Master's thesis

NTNU
Norwegian University of Science and Technology
Faculty of Engineering
Department of Civil and Environmental Engineering

Daniil Popov

Submerged Floating Tunnel: Water-Structure Interaction

Master's thesis in Coastal and Marine Engineering and Management
Supervisor: Hans Bihs
August 2019

NTNU
Norwegian University of Science and Technology

Daniil Popov

Submerged Floating Tunnel: Water-Structure Interaction

Master's thesis in Coastal and Marine Engineering and Management
Supervisor: Hans Bihs
August 2019

Norwegian University of Science and Technology
Faculty of Engineering
Department of Civil and Environmental Engineering

NTNU
Norwegian University of
Science and Technology

ERASMUS +: ERASMUS MUNDUS MOBILITY PROGRAMME

Master of Science in

COASTAL AND MARINE ENGINEERING AND MANAGEMENT

CoMEM

SUBMERGED FLOATING TUNNEL: WATER-STRUCTURE INTERACTION

Norwegian University of Science and Technology
11 August 2019

Daniil Popov

The Erasmus+: Erasmus Mundus MSc in Coastal and Marine Engineering and Management is an integrated programme including mobility organized by five European partner institutions, coordinated by Norwegian University of Science and Technology (NTNU).

The joint study programme of 120 ECTS credits (two years full-time) has been obtained at two or three of the five CoMEM partner institutions:

- Norges Teknisk- Naturvitenskapelige Universitet (NTNU) Trondheim, Norway
- Technische Universiteit (TU) Delft, The Netherlands
- Universitat Politècnica de Catalunya (UPC). BarcelonaTech. Barcelona, Spain
- University of Southampton, Southampton, Great Britain
- City University London, London, Great Britain

During the first three semesters of the programme, students study at two or three different universities depending on their track of study. In the fourth and final semester an MSc project and thesis has to be completed. The two-year CoMEM programme leads to a multiple set of officially recognized MSc diploma certificates. These will be issued by the universities that have been attended by the student. The transcripts issued with the MSc Diploma Certificate of each university include grades/marks and credits for each subject.

Information regarding the CoMEM programme can be obtained from the programme coordinator:

Øivind A. Arntsen, Dr.ing.
Associate professor in Marine Civil Engineering
Department of Civil and Environmental Engineering
NTNU Norway
Mob.: +4792650455 Fax: + 4773597021
Email: oivind.arntsen@ntnu.no

CoMEM URL: https://www.ntnu.edu/studies/mscomem

CoMEM Thesis

This thesis was completed by:
Daniil Popov

Under supervision of:
Hans Bihs, Associate Professor, NTNU
Arun Kamath, Post-Doctoral Fellow, NTNU
Weizhi Wang, PhD Candidate, NTNU

As a requirement to attend the degree of
Erasmus+: Erasmus Mundus Master in Coastal and Marine Engineering and Management (CoMEM)

Taught at the following educational institutions:

Norges Teknisk- Naturvitenskapelige Universitet (NTNU)
Trondheim, Norway

Technische Universiteit (TU) Delft
Delft, The Netherlands

At which the student has studied from August 2017 to August 2019.

Submerged Floating Tunnel: Water-Structure Interaction

A Masters' Thesis
submitted to the Faculty of Civil and Environmental Engineering
at the Norwegian University of Science and Technology

by

Daniil Popov

Abstract

This study focuses on water-structure interaction of submerged floating tube in homogeneous and stratified flows, as well as gravity current development. The latter was done in order to set up and validate numerical model that treats water stratification properly and in a computationally efficient manner.

First part of the study is dedicated to gravity current development. Grid convergence study was performed for simulation of two-dimensional gravity current, which showed that optimal cell sizes for the problem in question are 5 mm and 2.5 mm. In addition, Large-Eddy Simulation (LES) model of turbulence was tested, and its performance in simulation was compared to performance of simulation without any turbulence modelling. It was established that the latter represents gravity current development in two dimensions more accurately. After that, gravity current development in three dimensions was performed with LES modelling of turbulence and without any turbulence model. Both simulations were in good agreement with results of physical experiments, therefore LES model is a preferable choice as it is less computationally demanding.

In second part of the project, rigidly fixed horizontal cylinder in flow was considered in order to investigate in-line forces, acting upon the cylinder. At first, model with homogeneous flow was set up and validated. It was established that two-dimensional model with cell size of 2.5 mm and CFL criterion of 0.3 is a good choice in terms of balance between accuracy and computational efficiency. After that, system of two cylinders with varying distance between them was tested. It was established that in-line forces for both cylinders are affected, with influence on the second cylinder being more stark.

Third part of the study is dedicated to horizontal cylinder in stratified flow. Parameters of produced internal waves were in agreement with results of physical experiments.

Acknowledgments

This study was supported in part with computational resources at the Norwegian University of Science and Technology (NTNU) provided by the Norwegian Metacentre for Computational Science, NOTUR, under project number NN2620K.

I would first like to thank my main supervisor Hans Bihs for the opportunity to work on the chosen topic as part of his team. I also thank him for his guidance and support that he provided throughout the course of my work. I express my deepest gratitude to my co-supervisor Arun Kamath for his patience, cooperation and advice. The door to his office was always open to me whenever I encountered difficulties with my research or my writing. I also thank my co-supervisor Weizhi Wang for his help with technical issues that appeared as the study progressed.

I would also like to acknowledge Prof. Øivind Arntsen and Sonja Hammer for the assistance and encouragement they provided to CoMEM participants during our terms in Trondheim. In addition, I thank my classmates for pleasant moments we shared throughout the past two years.

Finally, I express my very profound appreciation to my parents for their love and unfailing support throughout the years of study. This accomplishment would not have been possible without them. Thank you.

Contents

List of Figures

Chapter 1

Introduction

1.1 General

Coastal areas around the globe are densely populated, approximately 3 billion people live in the coastal zone, which occupies less than 15% of the Earth area. Oceans and seas have been a major source of food for humanity for as long as has existed. Apart from that, they provide means of transportation: water-based transport in its ultimate form connects continents, letting millions of tonnes of goods travel daily over enormous distances. On a smaller scale, ferry connections play significant role in local transport systems, with Norway being a good illustration. However, in smaller scale cases, such as ferries across Norwegian fjords, water-based transport is not the only available option. Moreover, it is not always a preferable one, despite the inherent entertainment component. Ferry connections are slow and dependent on weather conditions, thus, they become bottlenecks in any transportation network, raising interest in replacing them with bridges and tunnels. Norwegian Coastal Route, 1100 km long route E39 that connects cities of Trondheim and Kristiansand through Ålesund, Stavanger, Bergen and Molde, exemplifies this: according a to study performed by The Norwegian road authority, Statens Vegvesen [1], E39 with its 7 ferry connections takes approximately 21 hours to complete. It is estimated that implementation of ferry-free connections such as tunnels and bridges, as well as improving parts of the road, will lead to reduction of time required to pass it by half and make the route 50 km shorter. However, geographical conditions, such as significant width and depth of some fjords, are associated with additional difficulties for design and construction of conventional tunnels and bridges, which makes their feasibility questionable. In this context, concept of Submerged Floating Tube (SFT) is considered as possible solution.

Concept of SFT implies tube that is placed under water and is secured in position by tendons and pontoons. Even though the concept is not new, such a structure

has never been built before due to high levels of risk associated with it, for example, risks of resilience of the structure to accidents (ship collisions, explosions, etc). However, safety challenges are not investigated in this study. Instead, it concentrates on water-structure interaction of the submerged floating tube, which constitutes another major uncertainty of the concept. In particular, character and magnitude of forces acting upon the structure in stratified water, which is water with non-constant density profile, are investigated so as to establish the influence of tow resistance of internal waves, which appear when flow of stratified water encounters an obstacle, in this case, cylinder.

Numerical modelling of internal waves, appearing on the surface of two water layers of fluids with different densities, constitutes a complicated challenge as it requires numerical domain that is long enough to encompass the wave train, as well as fine mesh so as to resolve internal waves and their influence on the cylinder accurately. In addition, simulation period must be sufficient so as to let internal waves enough time to develop. All aforementioned factors require some additional preparation steps whereby optimal size of the numerical domain and optimal cell size can be established. Simulation of gravity current propagation in two- and three-dimensional setups was chosen as a measure that can help achieving those goals.

Gravity current develops when two fluids of different density come into contact: it is driven by density differences. Gravity current are encountered both in natural and man-made conditions, for example in industry. It is an important research field as such, therefore part of the study concentrates on the numerical modelling of the gravity current propagation.

Both simulation of rigidly fixed cylinder in homogeneous and stratified water and simulation of the gravity current development are performed with the open-source computational fluid dynamics modelling program - REEF3D. REEF3D has been previously used to study various problems in the field of hydraulic, ocean and offshore engineering such as wave decomposition by Kamath [2], sloshing by Grotle [3], pier scour by Ahmad [4], seawall scour and pipeline scour by Ahmad [5], [6], extreme wave impact by Bihs [7] and irregular breaking wave forces by Aggarwal [8].

1.2 Objectives of the study

- Set up and validate the development of the gravity current in two- and three-dimensions in a numerical model;
- Set up and validate the rigidly fixed horizontal cylinder in flow of homogeneous water in a numerical model;

- Set up and validate the rigidly fixed horizontal cylinder in flow of stratified water in a numerical model;
- Investigate influence of various parameters on forces acting upon the cylinder. Parameters in question are the submergence of the cylinder, configuration of the structure and thickness of the water of higher density.

Chapter 2

Numerical Model

2.1 Introduction to REEF3D

In this project, the open-source computational fluid dynamics (CFD) modelling program - REEF3D - is used to simulate a numerical tank. The tank contains structure under current of water of varying density, and the aim is to investigate water-structure interaction. REEF3D is developed at the Department of Civil and Environmental Engineering of Norwegian University of Science and Technology (NTNU) in Trondheim, Norway. It employs high order space and time discretization schemes, which are applied to three-dimensional Reynolds-Averaged Navier-Stokes (RANS) Equations. Moreover, REEF3D is capable of calculating the pressure, which is of crucial importance for reaching the goal of this study, and uses the level-set method, which yields accurate representation of free surface. Concentration functions, installed in REEF3D, enable it to treat water of non-constant density, which is used for modelling of mixing and internal waves. Turbulence in REEF3D can be resolved directly by means of Direct Numerical Simulation (DNS), but also can be modelled with Large-Eddy Simulation (LES) [9], $k-\omega$ [10] and $k-\epsilon$ [11] models.
Some applications of REEF3D are outlined below.

- Calculation of forces acting upon various structures under currents and/or waves;
- Modelling of mixing of fluids with varying densities;
- Behaviour of floating body;
- Sediment transport modelling;

Various approaches are developed within the program, allowing for flexibility in completing researches with different combinations. It is important from the perspective of reduction of demand of computational resources.

2.2 Governing Equations

2.2.1 Reynolds-averaged Navier-Stokes Equations

Viscous and incompressible fluids are described by the Navier-Stokes equations, which stem from principle of momentum conservation. Together with continuity equation, RANS equations constitute governing system of equations. Incompressibility assumption arises from the fact that fluid velocities dealt with in marine and hydraulic engineering are of insignificant influence on compressibility of water and air, therefore system of governing equations can be simplified.

$$\frac{\partial u_i}{\partial x_i} = 0 \tag{2.1}$$

$$\frac{\partial u_i}{\partial t} + u_j \frac{\partial u_i}{\partial x_j} = -\frac{1}{\rho}\frac{\partial p}{\partial x_i} + \frac{\partial}{\partial x_j}\left[\nu\left(\frac{\partial u_i}{\partial x_j} + \frac{\partial u_j}{\partial x_i}\right) - \overline{u_i u_j}\right] + g_i \tag{2.2}$$

Where:

- u - velocity averaged over time;
- x - geometrical scale;
- ρ - water density;
- ν - kinematic viscosity;
- p - pressure;
- g - acceleration of gravity;
- $\overline{u_i u_j}$ - represents Reynolds stresses.

Convective and transient terms of the equation are presented in the left hand side of the equation, whereas right hand side is comprised of volume and surface forces.

2.2.2 Concentration function

Another equation that will be used in the study is function which defines concentration and its propagation. It is a parabolic equation, given as follows:

$$\frac{\partial C}{\partial t} + u_i \frac{\partial C}{\partial x_i} = \frac{\partial^2 C}{\partial x_i^2}(\nu + \nu_t) \tag{2.3}$$

Where:
C - concentration;
ν_t - eddy viscosity.

Solution of the equation is smooth, in order to be solved it requires boundary and initial conditions. Boundary conditions for cases considered in this study are presented as outflow and inflow boundaries (respectively, left and right boundaries in the case with flow) or as closed boundaries (walls) in case with no flow.

2.3 Turbulence modelling

2.3.1 k-ω model

When $k-\omega$ model of turbulence [10] is employed, Reynolds stress term from RANS is substituted by Boussinesq approximation as follows:

$$-\overline{u_i u_j} = \nu_t \left(\frac{\partial u_j}{\partial x_i} + \frac{\partial u_i}{\partial x_j} \right) - \frac{2}{3} k \delta_{ij} \tag{2.4}$$

With

$$\nu_t = c_\mu \frac{k}{\omega} \tag{2.5}$$

Where:
k - turbulent kinetic energy;
ω - specific turbulent dissipation;
ν_t - eddy viscosity.

Parameters k and ω are obtained through solving transport equations, which are given below.

$$\frac{\partial k}{\partial t} + u_j \frac{\partial k}{\partial x_j} = \frac{\partial}{\partial x_j} \left[\left(\nu + \frac{\nu_t}{\sigma_k} \right) \frac{\partial k}{\partial x_j} \right] + P_k - \beta_k k \omega \tag{2.6}$$

$$\frac{\partial \omega}{\partial t} + u_j \frac{\partial \omega}{\partial x_j} = \frac{\partial}{\partial x_j} \left[\left(\nu + \frac{\nu_t}{\sigma_\omega} \right) \frac{\partial \omega}{\partial x_j} \right] + \frac{\omega}{k} \alpha P_k - \beta_k k \omega^2 \tag{2.7}$$

Where:
P_k - turbulent production rate.
Coefficients α, β and σ are set as follows:

- $\alpha = \frac{5}{9}$;

- $\beta_k = \frac{9}{100}$;
- $\beta = \frac{3}{40}$;
- $\sigma_k = 2$;
- $\sigma_\omega = 2$

Schlichting's rough wall law [12] is employed so as to account for surface roughness at solid boundaries. The law is as follows:

$$u^+ = \frac{1}{\kappa} ln(\frac{30y}{k_s}) \tag{2.8}$$

Where:
u^+ - dimensionless wall velocity;
k_s - equivalent sand roughness;
y - water depth.
Coefficient κ is set to 0.4. It is assumed that in proximity of the wall turbulent production is equal to dissipation. The wall function for turbulent dissipation ω of the bed cell is given as follows:

$$\omega_{wall} = -\frac{c_\mu^{3/4} k_w^{1/2} U_w^+}{\Delta y_p} \tag{2.9}$$

Where:
Δy_p - distance from the wall to the center of the cell.

Turbulent kinetic energy k is obtained through integrating the source terms of eq. 2.6 over the bed cell:

$$\int (P_k - \omega_{wall})\rho = \left[\frac{\tau_w u_w}{\Delta y_p} - \frac{\rho c_\mu^{3/4} k_w^{3/2} U_w^+}{\Delta y_p} \right] \tag{2.10}$$

Where:
τ_w - wall shear stress;

2.3.2 Large-Eddy Simulation model of turbulence

Turbulent flows are comprised of eddies of various sizes. Large eddies are more energetic and therefore contribute to transport of conserved properties much more than small eddies, which rises interest in such modelling approach that treats large eddies with more details than small ones, thus reducing computational demand, compared

to direct numerical simulation of all eddies. This approach - Large Eddy Simulation method [9] - is based on filtering the velocity field in such a way that only big scale components remain. It is done as follows:

$$\bar{u_i}(x) = \int G(x, x')u_i(x')dx' \tag{2.11}$$

With $G(x, x')$ representing kernel of the filter. Various kernels are available in LES, in particular, Gaussian kernel, a box filter (simple local average) and a cutoff (this filter removes Fourier coefficients that belong to wave numbers beyond the cutoff). Each filter is characterized by length scale Δ. Thus, eddies bigger than Δ are considered large and therefore will be resolved, whereas smaller eddies will be modelled.

Filtering Navier-Stokes equations for incompressible fluid yields the following equation:

$$\frac{\partial(\rho\bar{u_i})}{\partial t} + \frac{\partial(\rho\overline{u_i u_j})}{\partial x_j} = -\frac{\partial\bar{p}}{\partial x_i} + \frac{\partial}{\partial x_j}\left[\mu\left(\frac{\partial\bar{u_i}}{\partial x_j} + \frac{\partial\bar{u_j}}{\partial x_i}\right)\right] \tag{2.12}$$

Filtering does not affect continuity equation as it is linear:

$$\frac{\partial(\rho\bar{u_i})}{\partial x_i} = 0 \tag{2.13}$$

Computation of the second component in eq. 2.12 is a challenging task, since $\overline{u_i u_j} \neq \bar{u_i}\bar{u_j}$, therefore, following modelling approximation is introduced:

$$\tau_{ij}^s = -\rho(\overline{u_i u_j} - \bar{u_i}\bar{u_j}) \tag{2.14}$$

Subgrid-scale (SGS) Reynolds stress τ_{ij}^s represents momentum flux, which appears in large scale, but caused by small-scale eddies. Local averages of the small-scale velocity field constitute this parameter.

Various means are available for determination of subgrid-scale Reynolds stress, one of them is called Smagorinsky model [13], which is an eddy viscosity model. It is based upon the idea that the main impact of SGS Reynolds stress results in increased dissipation and transport. Thus, model takes the following form:

$$\tau_{ij}^s - \frac{1}{3}\tau_{kk}^s\delta_{ij} = \mu_t\left(\frac{\partial\bar{u_i}}{\partial x_j} + \frac{\partial\bar{u_j}}{\partial x_i}\right) = 2\mu_t\bar{S_{ij}} \tag{2.15}$$

Where:
μ_t - eddy viscosity;
$\bar{S_{ij}}$ - strain rate of the large scale field.

Eddy viscosity is determined as follows:

$$\mu_t = C_s^2 \rho \Delta^2 |\bar{S}| \tag{2.16}$$

With:

$$|\bar{S}| = (\bar{S_{ij}} \bar{S_{ij}})^{\frac{1}{2}} \tag{2.17}$$

Where:
C_s - model parameter (usually taken as $C_S \simeq 0.2$);
Δ - filter scale;

2.4 Numerical Treatment of Governing Equations

Numerical treatment of partial differential equations (PDE), in this case system of RANS equations, entails use of the following notions:

- Stability. Numerical solution is called stable when small discrepancies in it do not cause solution to 'blow up'. Notion of stability normally implies certain conditions in form of limits to time step Δt or grid size Δx. It is convenient to assemble those limits in such a way that sets clear dependency between them, i.e. CFL condition, which is given as follows for certain numerical schemes:

$$\sigma = \frac{|u|\Delta t}{\Delta x} \tag{2.18}$$

- Convergence. Numerical solution must converge to actual solution of the PDE in question with Δx and $\Delta t \to 0$.

- Consistency. Numerical solution is said to be consistent with the actual solution if it converges to it and meets requirements of stability. Truncation error is a measurement of consistency: it is the difference between numerical solution and actual solution. Numerical scheme is said to be consistent with the actual solution if truncation error is zero for $\Delta x, \Delta t \to 0$.

- Accuracy. It is important that numerical scheme does not introduce non-physical damping to mixing of two fluids (as in the case under consideration in this project) or to wave propagation.

- Boundary conditions. Correct choice of boundary conditions is of crucial importance for any numerical simulation. It affects accuracy and may hamper simulation if boundary conditions are ill-posed.

- Efficiency. Strict requirements for accuracy and consistency may lead to simulation time that lies beyond acceptable limits, therefore computational efficiency must be taken into account as another important factor. Efficiency can be improved by introducing parallel computation.

2.4.1 Convection Discretization

2nd order Central Differences Scheme

Central differences scheme is symmetric: parameter in question is computed from values on both sides of it. Advantage of this method stems from relatively high accuracy of it (compared to 1-st order upwind scheme), however, it is associated with bigger demand from the perspective of computational efficiency. In addition, when physical damping is present, the scheme is unconditionally unstable, which reduces its applicability significantly. Scheme is built as follows:

$$\frac{\partial u}{\partial x} = \frac{u_{i+1} - u_{i-1}}{2\Delta x} \tag{2.19}$$

1st order Upwind Scheme

Unlike central differences scheme, 1-st order upwind scheme is more stable, however, this comes at cost of accuracy. Apart from that, direction is of importance now, as the parameter under investigation at cell i is calculated based on value at cell $i-1$ in case of positive direction and $i+1$ if the direction is negative. Scheme for positive direction is built as follows:

$$\frac{\partial u}{\partial x_i} = \frac{u_i - u_{i-1}}{\Delta x} \tag{2.20}$$

5th order WENO scheme

Modelling of the gravity current front propagation, which is one of the aims of the project, required sound numerical efficiency and stability, as well as high order of accuracy, so as to reduce non-physical damping of propagation speed and mixing. Weighted essentially non-oscillatory scheme (WENO), developed by Jiang [14] as combination of ENO schemes, first of which was constructed by Harten [15], combines those qualities and therefore is employed in simulations of the project. Its description is given below.

$$u_i \frac{\partial u_i}{\partial x_i} \simeq \frac{1}{\Delta x} \left(\bar{u}_{i+1/2} u_{i+1/2} - \bar{u}_{i-1/2} u_{i-1/2} \right) \tag{2.21}$$

Where:
$\bar{u}$ - convection velocity obtained at the cell surfaces through interpolation;
$u_{i+1/2}$ - convection velocity at the cell surface $i+1/2$, computed by means of WENO scheme.

WENO scheme is comprised of weighted sum of ENO stencils as follows:

$$U^{\pm}_{i+1/2} = \omega^{\pm}_1 U^{1\pm}_{i+1/2} + \omega^{\pm}_2 U^{2\pm}_{i+1/2} + \omega^{\pm}_3 U^{3\pm}_{i+1/2} \tag{2.22}$$

Where:
$\omega^{\pm}_n$ - non-linear weighting factors.

Upwind direction of the parameters in question is represented by the sign $\pm$. Three ENO stencils are shown as U^1, U^2 and U^3. They are computed as follows:

$$\begin{aligned} U^{1-}_{i+1/2} &= \frac{1}{3}u_{i-2} - \frac{7}{6}u_{i-1} + \frac{11}{6}u_i \\ U^{2-}_{i+1/2} &= -\frac{1}{6}u_{i-1} + \frac{5}{6}u_i + \frac{1}{3}u_{i+1} \\ U^{3-}_{i+1/2} &= \frac{1}{3}u_i + \frac{5}{6}u_{i+1} - \frac{1}{6}u_{i+2} \end{aligned} \tag{2.23}$$

Non-linear weighting factors are determined as follows:

$$\begin{aligned} \omega^{\pm}_1 &= \frac{\alpha^{\pm}_1}{\alpha^{\pm}_1 + \alpha^{\pm}_2 + \alpha^{\pm}_3} \\ \omega^{\pm}_2 &= \frac{\alpha^{\pm}_2}{\alpha^{\pm}_1 + \alpha^{\pm}_2 + \alpha^{\pm}_3} \\ \omega^{\pm}_3 &= \frac{\alpha^{\pm}_3}{\alpha^{\pm}_1 + \alpha^{\pm}_2 + \alpha^{\pm}_3} \end{aligned} \tag{2.24}$$

With coefficients $\alpha^{\pm}_n$ being determined as follows:

$$\begin{aligned} \alpha^{\pm}_1 &= \frac{1}{10}\frac{1}{(\bar{\epsilon} + IS^{\pm}_1)^2} \\ \alpha^{\pm}_2 &= \frac{6}{10}\frac{1}{(\bar{\epsilon} + IS^{\pm}_2)^2} \\ \alpha^{\pm}_3 &= \frac{3}{10}\frac{1}{(\bar{\epsilon} + IS^{\pm}_3)^2} \end{aligned} \tag{2.25}$$

Where:
IS - smoothness indicators;
ϵ - regularization parameter ($\epsilon = 10^{-6}$).

Weight of the indicator is defined by the extent of smoothness of the solution: the smoothest solution is given the largest weight. Smoothness indicators are computed as follows:

$$IS_1^{\pm} = \frac{13}{12}(q_1 - 2q_2 + q_3)^2 + \frac{1}{4}(q_1 - 4q_2 + 3q_3)^2$$

$$IS_2^{\pm} = \frac{13}{12}(q_2 - 2q_3 + q_4)^2 + \frac{1}{4}(q_2 - q_4)^2 \tag{2.26}$$

$$IS_3^{\pm} = \frac{13}{12}(q_3 - 2q_4 + q_5)^2 + \frac{1}{4}(3q_3 - 4q_4 + q_5)^2$$

2.4.2 Time treatment

Various time discretization schemes are implemented within REEF3D, among which 3-rd order TVD Runge-Kutta is seen as optimal [16]. It provides high accuracy with reasonable computational efficiency. It is built up as follows:

$$\begin{aligned} c^{(1)} &= c^n + \Delta t L(c^n) \\ c^{(2)} &= \frac{3}{4}c^n + \frac{1}{4}c^{(1)} + \frac{1}{4}\Delta t L(c^{(1)}) \\ c^{n+1} &= \frac{1}{3}c^n + \frac{2}{3}c^{(2)} + \frac{2}{3}\Delta t L(c^{(2)}) \end{aligned} \tag{2.27}$$

2.4.3 Level Set Method

REEF3D employs two-phase model of the flow so as to distinguish between fluid and air, and the interface-capturing level set method (LSM) [17] is used to present the surface: interface between two faces is regarded as zero-contour of the LSM. In zones below and above the zero-contour, LSM function is connected to distance function as follows:

$$\phi(\vec{x}, t) \begin{cases} > 0, & \text{if } \vec{x} \in \text{phase 1} \\ = 0, & \text{if } \vec{x} \in \Gamma \\ < 0, & \text{if } \vec{x} \in \text{phase 2} \end{cases}$$

Convection equation is used to link level set function with flow field. Pure convection equation is given as follows:

$$\frac{\partial \phi}{\partial t} + u_j \frac{\partial \phi}{\partial x_j} = 0 \tag{2.28}$$

2.4.4 Computation of pressure

Computation of pressure in the RANS equation is associated with additional difficulties in modelling, as it cannot be solved directly, therefore certain steps need to be taken in order to obtain pressures while keeping computational efficiency at a reasonable level. REEF3D offers following approaches to the problem:

- PJM: Projection Method;
- SIMPLE: Semi Implicit Method for Pressure Linked Equation;
- PISO: Pressure Implicit with Splitting Operator algorithm;

Projection method is used in this study, its essence is given below.

Projection method [18] implies divergence free flow field, obtained by the solution for pressure, and is related to continuity equation. At first, intermediate velocity field u_i^* is introduced, then momentum equation with omitted pressure gradient is solved for this field. Momentum equation is as follows:

$$\frac{\partial u_i^*}{\partial t} + u_j^n \frac{\partial u_i^n}{\partial x_j} = \frac{\partial}{\partial x_j} \left[(\nu + \nu_t) \left(\frac{\partial u_i^n}{\partial x_j} + \frac{\partial u_j^n}{\partial x_i} \right) \right] + g_i \tag{2.29}$$

The fact that intermediate velocity field is not divergence free implies following:

$$\frac{\partial u_i^*}{\partial x_i} \neq 0 \tag{2.30}$$

Divergence free flow field is obtained through finding pressures that meet the requirement of Poisson equation, which is given as follows:

$$\frac{\partial}{\partial x_i} \left(\frac{1}{\rho(\phi^n)} \frac{\partial p^{n+1}}{\partial x_i} \right) = \frac{1}{\Delta t} \frac{\partial u_i^*}{\partial x_i} \tag{2.31}$$

Where:
p^{n+1} - pressure at the new time step.

Divergence free velocity at the new time step is computed via correcting velocity at the intermediate time step with pressure:

$$u_i^{n+1} = u_i^* - \frac{\Delta t}{\rho(\phi^n)} \frac{\partial p^{n+1}}{\partial x_i} \tag{2.32}$$

Chapter 3

Literature review

In this chapter, relevant research on gravity current propagation and horizontal cylinder in flow is outlined.

3.1 Development of the gravity current

3.1.1 Gravity current in two dimensions

Series of two-dimensional lock-exchange experiments were performed at the Hydraulics Laboratory of RomaTRE [19] as a part of research on development of gravity current. Water tank used for experiments was comprised of two reservoirs, separated by the gate, as shown in Fig. 3.1. One reservoir was filled with water of higher density (ρ_1) than density of the water in another reservoir (ρ_2). Length and width of the tank, as well as length of the reservoir with water of higher density (ρ_1) were set constant: $L_T = 3.0$ m, $b_T = 0.2$ m, $x_0 = 0.2$ m. Water density (ρ_1) and water depth H varied in experiments as shown in Table 3.1.

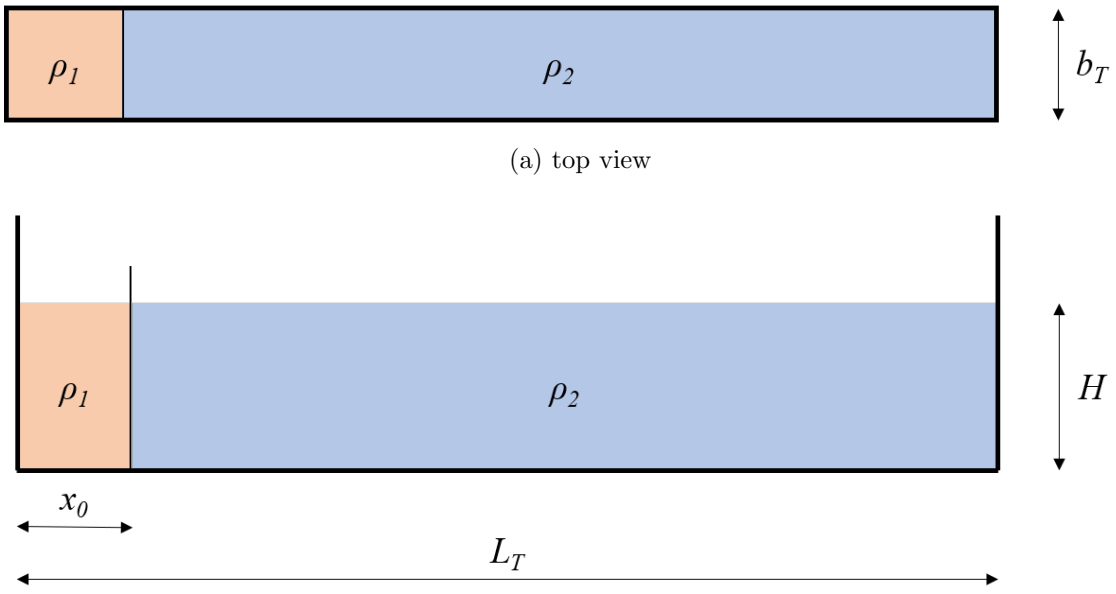

(a) top view

(b) side view

Figure 3.1: Water tank used in physical experiments on gravity current propagation in two dimensions

Table 3.1: Set of physical experiments on gravity current propagation in two-dimensional setup

Test	ρ_1 $[kg/m^3]$	H $[m]$	g' $[m/s^2]$
VT1	1035	0.3	0.34
VT2	1035	0.2	0.34
VT3	1035	0.1	0.34
VT4	1065	0.3	0.61
VT5	1065	0.2	0.61
VT6	1065	0.1	0.61
VT7	1095	0.3	0.87
VT8	1095	0.2	0.87
VT9	1095	0.1	0.87

Where:

$$g' = (\rho_1 - \frac{\rho_2}{\rho_1})g, \tag{3.1}$$

With $g = 9.81 m/s^2$.

After the gate had been removed, development and propagation of the gravity current were registered and converted into series of dimensionless time versus dimensionless space plots. Dimensionless time and space were calculated as follows:

$$T^* = \frac{t}{x_0/\sqrt{g'H}} \tag{3.2}$$

$$x_f^* = \frac{x_f}{H} \tag{3.3}$$

Where
x_f - instantaneous position of the front, [m];
t - time at which instantaneous position of the front is registered in certain position. [s]

3.1.2 Gravity current in three dimensions

Physical experiments on gravity current development in three dimensions were performed in water tank that was comprised of two equally sized reservoirs, filled with water of different densities, separated by the wall with the gate [19]. Development was influenced, among other things, by the width of the gate b (see Fig. 3.2).

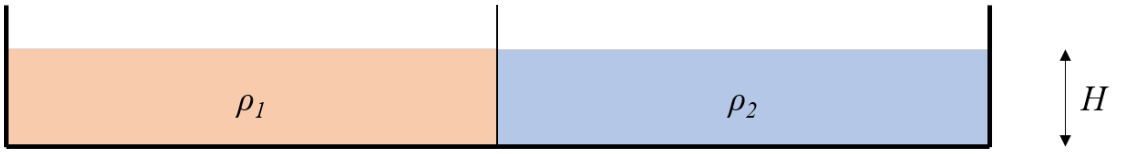

(a) side view

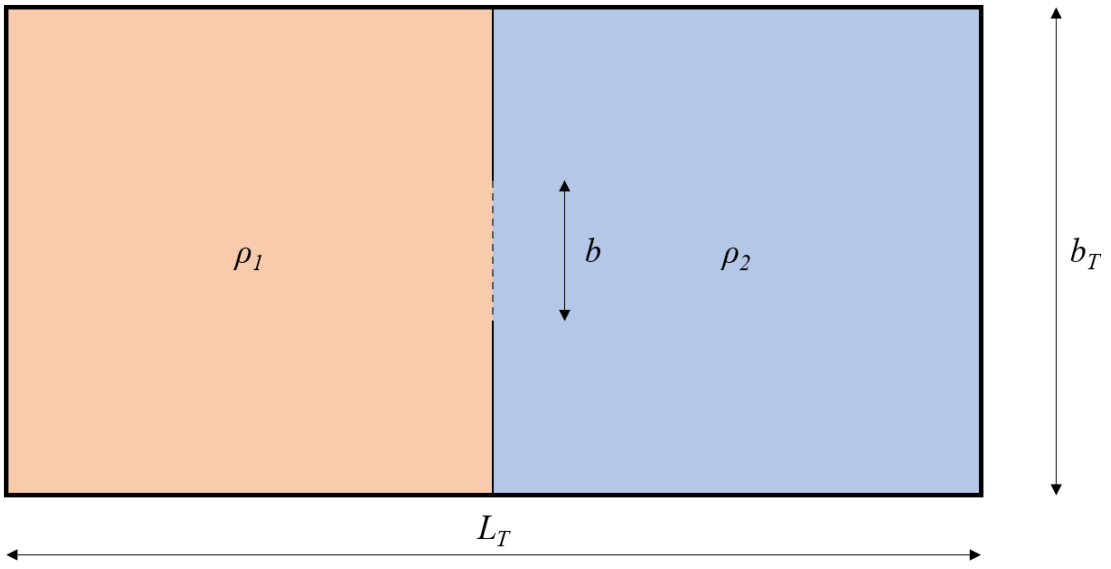

(b) top view

Figure 3.2: Water tank for gravity current propagation modelling in three-dimensional setup

Length and width of the tank were set as follows: $L_t = 2$ m, $b_T = 1$ m, respectively. Water depth $H = 0.15$ m. Width of the gate $b = 0.20$ m.

Apart from physical experiments, La Rocca [19] established numerical model, employing approach described by Rottman and Simpson [20] and Hogg [21], which uses rigid lid approximation. Rigid lid approximation is an assumption that free surface is covered with a rigid lid, which does not allow for its movement. This approximation is introduced in order to put double-layer shallow-water partial differential equation into conservative form, which is needed in order to use good shock-capturing numerical schemes. The equation is given as follows:

$$\frac{\partial \boldsymbol{u}_i}{\partial t} + \boldsymbol{u}_i \nabla \boldsymbol{u}_i = -\frac{1}{\rho_i} \nabla p_i - g\boldsymbol{k} - \frac{1}{\rho_i} \nabla \boldsymbol{T}^i \tag{3.4}$$

Where:
$\boldsymbol{T}^i$ - total stress tensor for layer i, including viscous and turbulence terms;
p_i - pressure distribution in layer i.

Pressure distributions are determined as follows:

$$p_1 = \rho_1 g(h_1 - z) + \rho_2 g h_2 \tag{3.5}$$

$$p_2 = \rho_2 g(h_1 + h_2 - z) \tag{3.6}$$

After rigid lid approximation is introduced, system is reduced to single-layer form, as shown by Ungarish and Zemach [22]. Thus, system of PDE takes the following form:

$$\frac{\partial h_1}{\partial t} + \frac{\partial p_1}{\partial x} + \frac{\partial q_1}{\partial y} = 0$$

$$\frac{\partial p_1}{\partial t} + \left[g h_1 \left(1 - \frac{\rho_2}{\rho_1}\right) - \frac{p_1^2}{h_1^2} \right] \frac{\partial h_1}{\partial x} + 2\frac{p_1}{h_1}\frac{\partial p_1}{\partial x} - \frac{p_1 q_1}{h_1^2}\frac{\partial h_1}{\partial y} + \frac{q_1}{h_1}\frac{\partial p_1}{\partial y} + \frac{p_1}{h_1}\frac{\partial q_1}{\partial y} = \frac{T^1_{xz}|_{z=0}}{\rho_1} \tag{3.7}$$

$$\frac{\partial q_1}{\partial t} + \left[g h_1 \left(1 - \frac{\rho_2}{\rho_1}\right) - \frac{q_1^2}{h_1^2} \right] \frac{\partial h_1}{\partial y} + 2\frac{q_1}{h_1}\frac{\partial q_1}{\partial y} - \frac{p_1 q_1}{h_1^2}\frac{\partial h_1}{\partial x} + \frac{q_1}{h_1}\frac{\partial p_1}{\partial x} + \frac{p_1}{h_1}\frac{\partial q_1}{\partial x} = \frac{T^1_{yz}|_{z=0}}{\rho_1}$$

Where:
p_1, q_1 - volumetric fluxes,
h_1, h_2 - layer thiknesses.

Use of the described numerical method yielded propagation speed of the gravity current that was in good agreement with results of physical experiments for two-dimensional current development. Moreover, front positions at different time instants, produced by the method for the three-dimensional gravity current development, also agreed well with positions obtained in physical tank.

3.2 Horizontal cylinder in flow

Stratification of water is a situation when layer of fresh or brakish water rests on top of salty water layer, which is caused by difference in densities. Stratification of water can be found in fjords, where fresh-water river discharge meets salty sea water and forms density profile as depicted in Fig. 3.3.

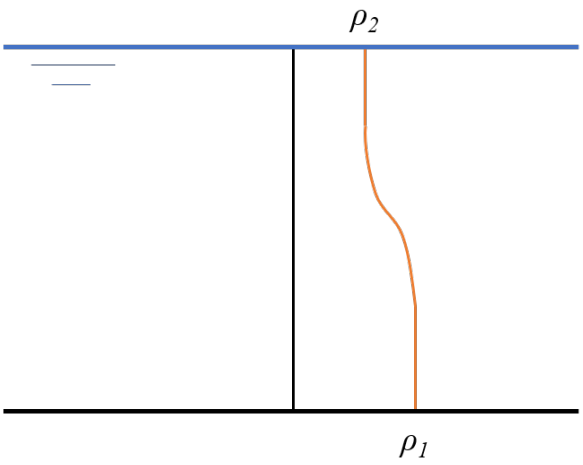

Figure 3.3: Stratification of water. Density profile

As can be seen in Fig. 3.3, fresh water layer does not turn into salty water layer abruptly: layer of varying density connects the two, its existence is a result of complicated and prolonged mixing, which occurs under influence of currents, waves, etc. Vessel encountering water bodies with stratification experiences so-called "dead-water" effects, first discussed by Ekman [23], when its manoeuvrability and speed are reduced.

When current is presented in such an ambience, placing a structure in it creates an obstacle, which results in appearing of lee waves. Lee waves are interfacial standing waves, which are created by action of buoyancy forces, acting upon parcels, disturbed by the obstacle. Upstream of the object, parcels of various density are carried by the current at levels of their neutral buoyancy, but once the current encounters the object, parcels are being displaced either upwards or downwards from the level. At this point, restoring buoyancy forces, caused by imbalance, start bringing disturbed parcels to their equilibrium, which is an oscillatory process, therefore wave patterns are observed. At certain distance downstream of the object, neutral buoyancy is restored. It is believed that "dead-water" effects are associated with action of lee waves.

Maximum natural buoyancy frequency, associated with oscillations mentioned above, is called Brünt-Väisälä frequency [24], which is determined as follows:

$$N_0 = \max \sqrt{-\frac{g}{\rho(z)} \frac{\partial \rho(z)}{\partial z}} \tag{3.8}$$

Where:
$\rho(z)$ - density profile, $[kg/m^3]$,

g - acceleration of gravity, $[m/s^2]$.

Forces acting upon the object in water stream - directed upwards (transverse force) and horizontally, along the current (in-line force) - are of utmost importance for submerged floating tube, and thus are the object of investigation. In-line force is comprised of forces brought about by skin friction and drag. The latter dominates in case of blunt objects, which is the case for the tube, therefore it is investigated in this section. Drag force is determined as follows:

$$F_D = 0.5 C_D \rho D u^2 \tag{3.9}$$

Where:
Cd - drag coefficient;
D - diameter of an object, $[m]$,
u - current velocity, $[m/s^2]$.

Physical experiments were performed in both homogeneous water and stratified water [25]. It was not possible to arrange current in water tank, therefore Galilean transformation of the problem was employed: cylinder was moving in water at rest. Sensors, installed on the cylinder, registered acting forces, and during the later stage they were analyzed in dimensionless form as follows:

$$C_D = \frac{f_x}{0.5 \rho D u^2} \tag{3.10}$$

Where:
f_x - registered force, $[N]$.
Experimental tank depicted in Fig. 3.4. z_0 represents distance between free surface and center of the cylinder.

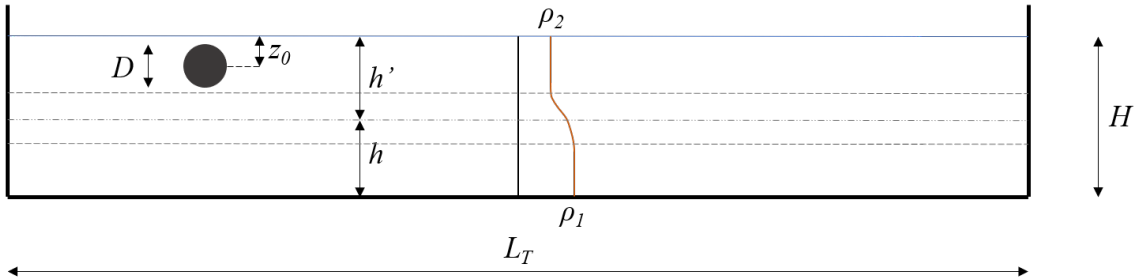

Figure 3.4: Water tank used in physical experiments

Tank characteristics were chosen as follows:

- Length of the tank: $L_T = 6$ m,

- Width of the tank: $b_T = 1$ m,
- Water depth: $H = 0.4$ m,
- Diameter of the cylinder: $D = 0.05$ m.

Layer on top consists of fresh water, bottom layer - of water with higher density. Layer of changing density is called pycnocline. Its characteristics (steepness of density gradient, thickness) are influencing forces acting upon the structure.

Series of experiments was comprised of set of tows of the cylinder (in positive and negative directions) performed in homogeneous water and in stratified water. For the latter, several values of water density of the bottom layer were tested (see table 3.2).

Table 3.2: Density ratios

N	$\Delta\rho/\rho_1$
1	0.013
2	0.018
3	0.025
4	0.031
5	0.032
6	0.040

Where:

$$\Delta\rho = \rho_1 - \rho_2 \tag{3.11}$$

Tows of the cylinder were performed with various speeds, corresponding to different current velocities, as listed below:

- 8 cm/s,
- 10 cm/s,
- 15 cm/s.

Apart from that, z_0/D ratio was varied so as to establish what influence submergence of the tube has on forces acting upon it. Set of values for this parameter is presented in table 3.3.
Forces obtained during experiments were analyzed in correlation with densimetric Froude number, which is determined as follows:

Table 3.3: Tested values of submergence

N	z_0/D
1	0.66
2	0.94
3	1.24
4	1.34
5	1.56
6	2.16
7	2.86
8	3.62
9	4.44

$$Fr_d = \frac{|U|}{c_i} \tag{3.12}$$

Where:
c_i - estimated celerity of the longest internal wave.

It is calculated as follows:

$$c_i = \sqrt{g\frac{\Delta\rho}{\rho_1}\frac{hh'}{h+h'}} \tag{3.13}$$

Where:
h' - distance from free surface to the centre of the pycnocline, [m],
h - distance from centre of the pycnocline to the bottom of the tank, [m].

Analysis of obtained data led to better understanding of water-structure interaction in stratified flow. Some results are outlined below.

As a result of the analysis of tows in homogeneous water higher value of the drag force was recorded, compared to the value of drag force in free stream conditions: $C_D = 1.56$ for $z_0/D = 1.34$, which is 25% higher than expected. It is likely that this happens due to proximity and blockage effects. Two kinds of blockage are distinguished:

- solid blockage due to limited depth that causes change of velocity past the cylinder.
- wake blockage, associated with the fact that average speed distributed behind the cylinder differently.

Proximity effect arises from the fact that cylinder is placed in vicinity of water surface.

As a result of the analysis of tows in stratified flow it was established that C_D is independent of Reynolds number and solely defined by densimetric Froude number. For values of densimetric Froude number Fr_d, that exceed certain critical densimetric Froude number $Fr_{d,cr}$, drag force in stratified flow drops below that in homogeneous water. From the analysis presented in, which also accounted for observations and analysis made by Carpenter and Keulegan in, it is deduced that critical densimetric Froude number is $Fr_{d,cr} \simeq 0.9$ for positive towing direction and $Fr_{d,cr} = 0.6$ for negative towing direction. It was also concluded that for $Fr_d >> 1$ stratification effects vanish, as well as when thickness of pycnocline grows. Biggest internal waves, thus highest tow resistance due to them, or most severe "dead-water" effect, were observed for $Fr_d \simeq 0.8$ in positive towing direction, while for negative towing direction biggest internal waves were registered for $Fr_d \simeq 0.5$.

As discussed above, several conditions influence increase in drag force acting upon the cylinder in stratified flow. Given that the aim of the research is to distinguish 'dead water' effect among those conditions, it is convenient to employ the following approach.
Tow resistance due to internal gravity waves, proposed by Lamb [26], can be determined as follows:

$$R_w = \frac{1}{8}\Delta\rho g H^2(1 - \frac{c_g}{U}) \tag{3.14}$$

Where:
H - height of the wave train, $[m]$,
c_g - group velocity, $[m/s]$,

Then tow resistance is compared to difference between registered in-line force, acting upon the structure, and the in-line force, appearing in homogeneous water, which is estimated based on data collected during tows in homogeneous water.

$$\beta_0 = (f_{xd} - f_{x,estimated})/R_w \tag{3.15}$$

When $\beta_0 \simeq 1$, increase in force is explained solely by the 'dead water' effect. If $\beta_0 \simeq 0$, there is no difference between homogeneous water and stratified water cases. In other situations other effects influence increase in force. It was concluded that 'dead water' effect exclusively explains difference in forces for the cases when the cylinder is located within the top layer, but not very close to the surface, combined with densimetric Froude number in the range of $0.4 < Fr_d < 0.6$. When this combination occurs, $0 < \beta_0 < 2.0$, thus tow resistance due to internal waves is a reasonably good estimate for "dead-water" effects, according to. However, for many other combinations other conditions influence the in-line force.

Chapter 4

Propagation of Gravity Current

In this chapter, development and propagation of gravity current are investigated first in two dimensions and then in three dimensions in order to validate numerical model, set up in REEF3D.

4.1 Gravity Current in two-dimensional setup

As a first step, two-dimensional case of gravity current propagation is investigated so as to establish optimal parameters needed for advancing towards modelling of gravity current in three-dimensional case and consequently, at a final stage of the project, towards modelling of submerged tube in stratified current. Parameters in question are the cell size and options for numerical treatment of turbulence. Following cell sizes are considered:

- 2.5 mm,
- 5 mm,
- 10 mm,
- 20 mm.

In order to account for turbulence, LES model is implemented.

In this project, simulations of gravity current development and propagation are performed in a numerical tank with characteristics identical to those of the tank used in physical experiments. However, width of the tank (b_T) is set to one cell size in order to make numerical model less computationally demanding. For the sake of simplicity, only parts of the original set of experiments are considered (listed in table 4.1):

Table 4.1: Set of numerical simulations on gravity current propagation in two-dimensional setup

Test	ρ_1 $[kg/m^3]$	H $[m]$	g' $[m/s^2]$
VT1	1035	0.3	0.34
VT4	1065	0.3	0.61

4.1.1 Simulations without turbulence model

At this stage of the project, turbulence is accounted for by means of Direct Numerical Simulation. After that, time versus space plots of Gravity Current propagation obtained without turbulence model will be compared to those obtained with LES modelling of turbulence.

VT1: cell size 20 mm

At first, coarse mesh with cell size of 20 mm is considered. Legend in Fig. 4.1 represents concentration as fraction of water with higher density in the tank at every cell of the domain, thus, red zone, which corresponds to value of one in the legend, is the zone fully comprised of water with higher density. Conversely, blue zone, represented by zero in the legend, has no water of higher density in it, therefore it is fresh water. As time advances, more colours appear in snapshots as a result of mixing: share of water with higher density increases in the area where gravity current propagates. In Fig, 4.1a (t = 0), simulation has not started yet, therefore the scale contains values [0,1]. However, at time instant t = 2 s (Fig. 4.1b) rescaling is done so as to keep gravity current clear and estimate the highest concentration in the numerical tank at the given time instant: concentration in the core of the gravity current is estimated to be $c = 0.995$. Further rescaling at t = 10 s (Fig. 4.1) yields $c = 0.945$ in the core of the current and $c \simeq 0.4$ in its tail. By the time current front reaches the point of 2.7 m (t = 20 s, Fig. 4.1d) concentration in the core drops to $c = 0.823$, while concentration in its tail is predominantly $c \simeq 0.3$. At the end of the simulation (t = 30 s, Fig. 4.1e) concentration in the core is $c = 0.607$, in the area surrounding the core at the right end of the tank it is $c \simeq 0.4$ and in the trail along the bottom of the tank it remains $c \simeq 0.3$.
Such model appeared to be the least computationally demanding out of the entire set of models. However, only large vortices are resolved, as can be seen in Fig. 4.1.

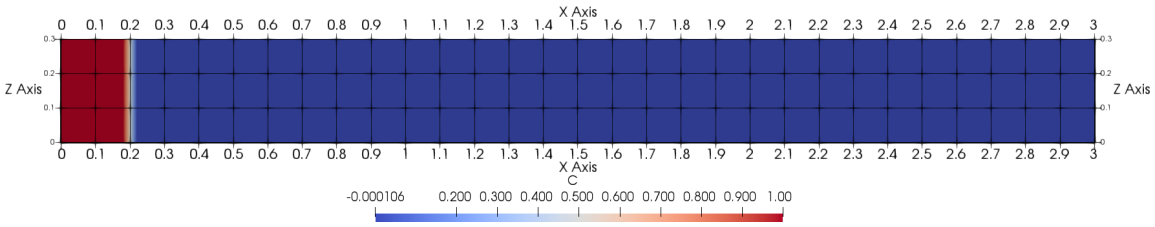

(a) t = 0 s

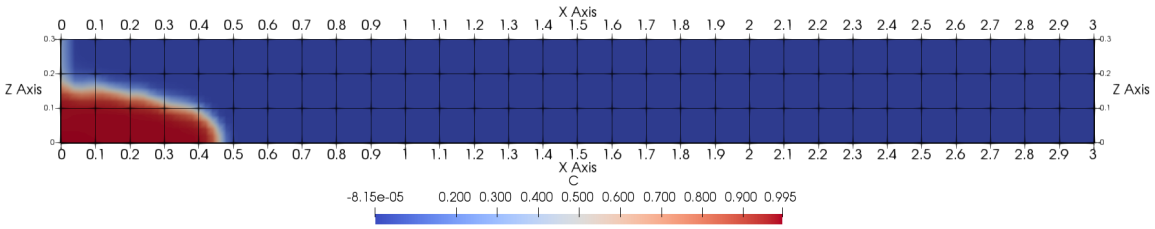

(b) t = 2 s

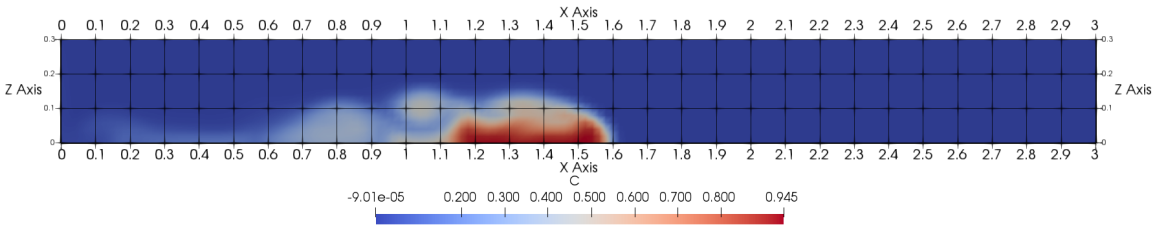

(c) t = 10 s

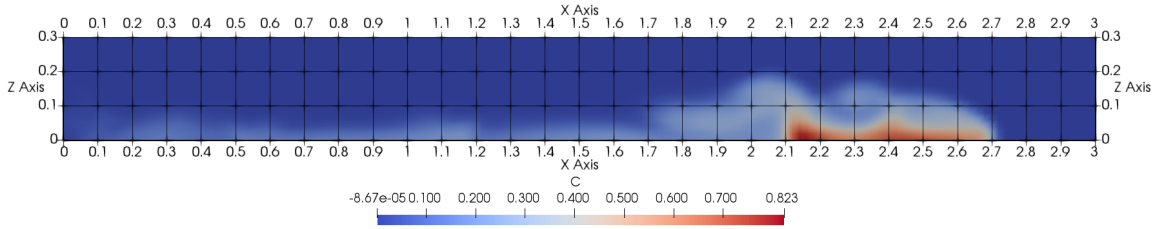

(d) t = 20 s

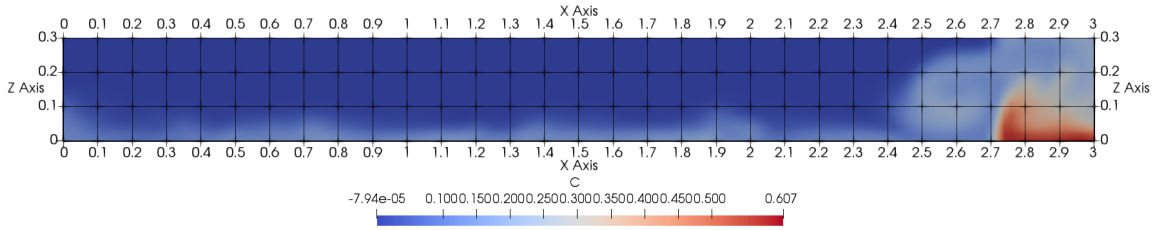

(e) t = 30 s

Figure 4.1: Gravity current propagation for cell size 20 mm.

VT1: cell size 10 mm

Legend in Fig. 4.2 represents concentration as fraction of water with higher density in water at every cell of the domain, thus, red zone, which corresponds to value of one in the legend, is the zone fully comprised of water with higher density. Conversely, blue zone, represented by zero in the legend, has no water of higher density in it, therefore it is fresh water. As time advances, more colours appear in snapshots as a result of mixing: share of water with higher density increases in the area where gravity current propagates. In Fig, 4.2a (t = 0), simulation has not started yet, therefore the scale contains values [0,1]. However, at time instant t = 2 s (Fig. 4.2b) rescaling is done so as to keep gravity current clear and estimate the highest concentration in the numerical tank at the given time instant: concentration in the core of the gravity current is estimated to be $c = 0.970$. Further rescaling at t = 10 s (Fig. 4.2) yields $c = 0.818$ in the core of the current and $c \simeq 0.2$ in its tail. By the time current front reaches the point of 2.7 m (t = 20 s, Fig. 4.2d) concentration in the core drops to $c = 0.634$, while concentration in its tail is predominantly $c \simeq 0.3$. At the end of the simulation (t = 30 s, Fig. 4.2e) concentration in the core is $c = 0.462$, in the area surrounding the core at the right end of the tank it is $c \simeq 0.250$ and in the trail along the bottom of the tank it remains $c \simeq 0.150$. It can be seen that mixing is enhanced for the case in question, compared to the previous case (Fig. 4.1).

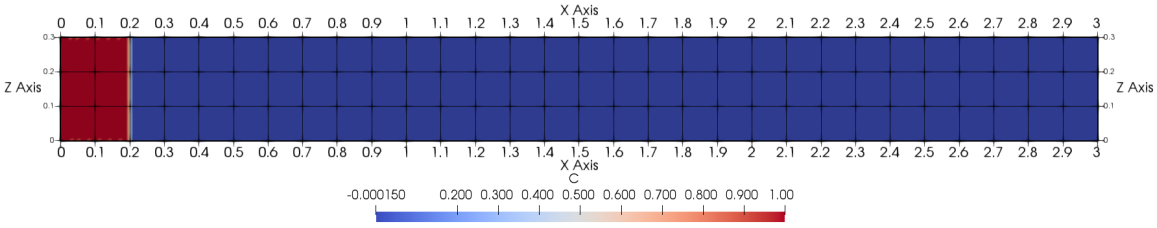

(a) t = 0 s

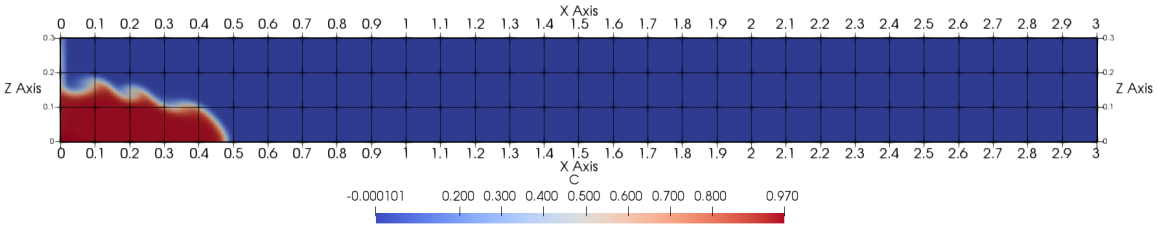

(b) t = 2 s

Figure 4.2: Gravity current propagation for cell size 10 mm.

As expected, finer mesh results in more distinctive vortices patterns (Fig. 4.2), however, such model is more computationally demanding.

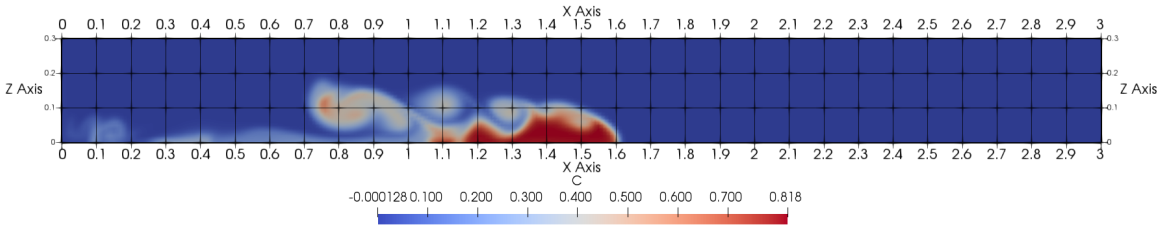

(c) t = 10 s

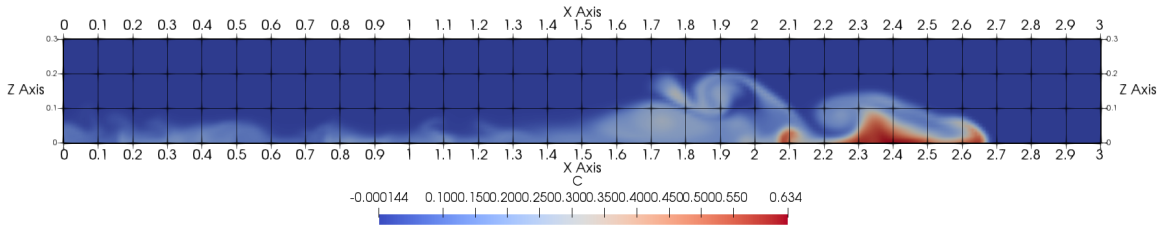

(d) t = 20 s

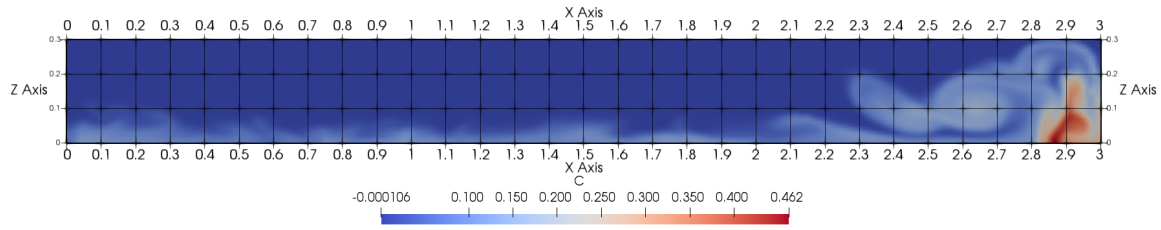

(e) t = 30 s

Figure 4.2: Gravity current propagation for cell size 10 mm.

VT1: cell size 5 mm

Fine mesh of 5 mm leads to further improved resolution of vortices, which comes at cost of further increased time needed to complete the simulation. Legend in Fig. 4.3 represents concentration as share of water with higher density in water at every cell of the domain, thus, red zone, which corresponds to value of one in the legend, is the zone fully comprised of water with higher density. Conversely, blue zone, represented by zero in the legend, has no water of higher density in it, therefore it is fresh water. As time advances, more colours appear in snapshots as a result of mixing: share of water with higher density increases in the area where gravity current propagates. In Fig, 4.3a (t = 0), simulation has not started yet, therefore the scale contains values [0,1]. However, at time instant t = 2 s (Fig. 4.3b) rescaling is done so as to keep gravity current clear and estimate the highest concentration in the numerical tank at the given time instant: concentration in the core of the gravity current is estimated to be $c = 0.997$. Further rescaling at t = 10 s (Fig. 4.3) yields $c = 0.888$ in the core of the current and $c \simeq 0.3$ in its tail.

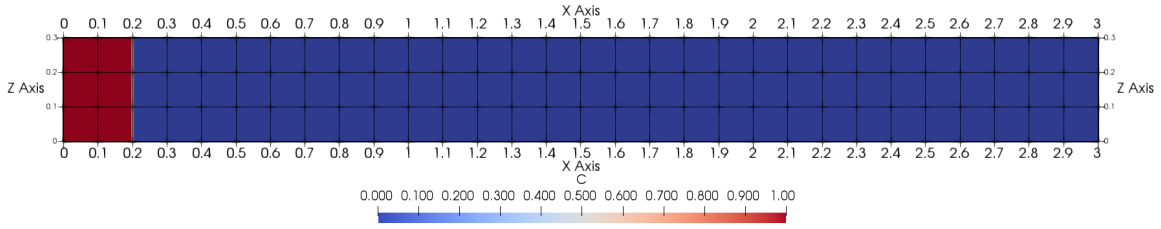

(a) t = 0 s

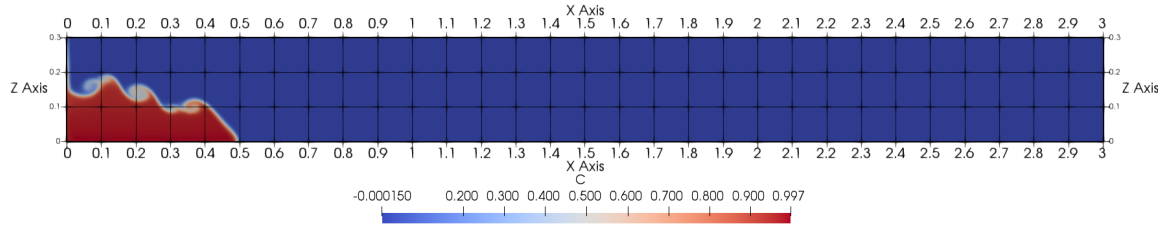

(b) t = 2 s

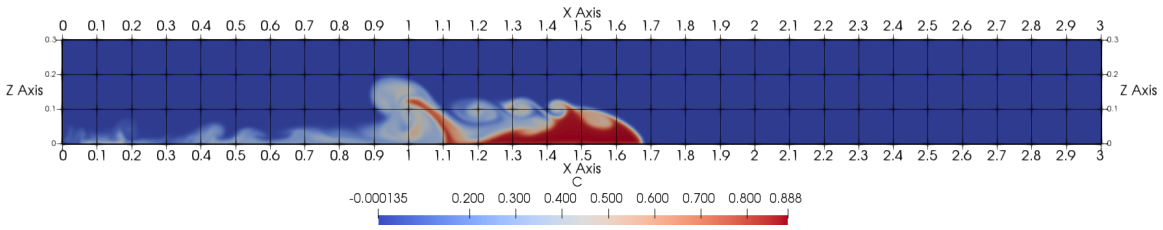

(c) t = 10 s

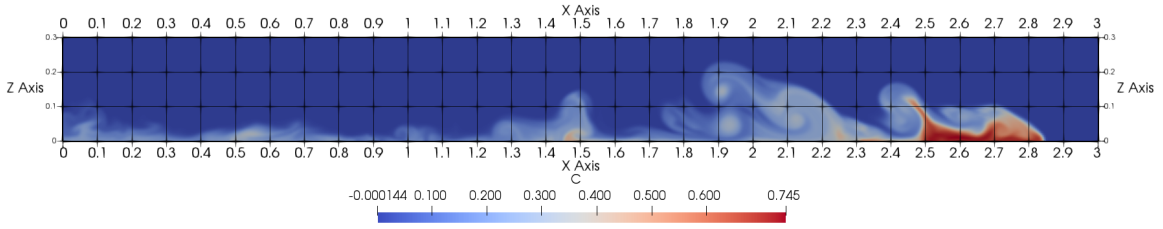

(d) t = 20 s

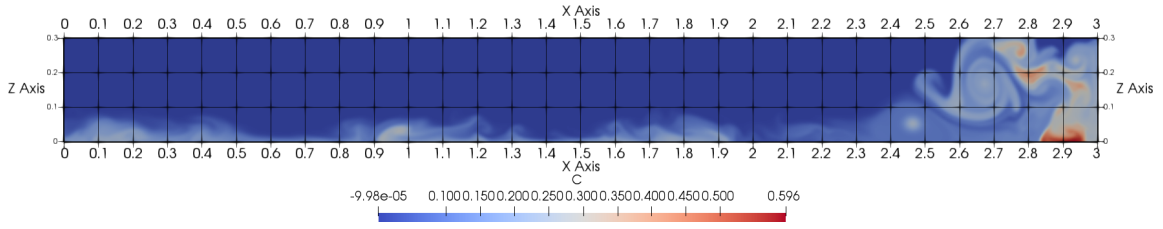

(e) t = 30 s

Figure 4.3: Gravity current propagation for cell size 5 mm.

By the time current front reaches the point of 2.85 m (t = 20 s, Fig. 4.3d) concentration in the core drops to $c = 0.745$, while concentration in its tail is predominantly

$c \simeq 0.350$. At the end of the simulation (t = 30 s, Fig. 4.3e) concentration in the core is $c = 0.596$, in the area surrounding the core at the right end of the tank it is $c \simeq 0.350$ with some inclusions of zones with higher concentration. In the trail along the bottom of the tank it is $c \simeq 0.250$. It can be seen that mixing is downsized for the case in question, compared to the previous cases (Fig. 4.1, Fig. 4.2).

VT1: cell size 2.5 mm

Very fine mesh of 2.5 mm cell size demonstrated formation of sophisticated patterns of large and small vortices, which is arguably the best outcome from the perspective of investigating the mixing of the two water parts (Fig. 4.4). The case under consideration is the most resource demanding, however, extent of the demand lies within reasonable limits.

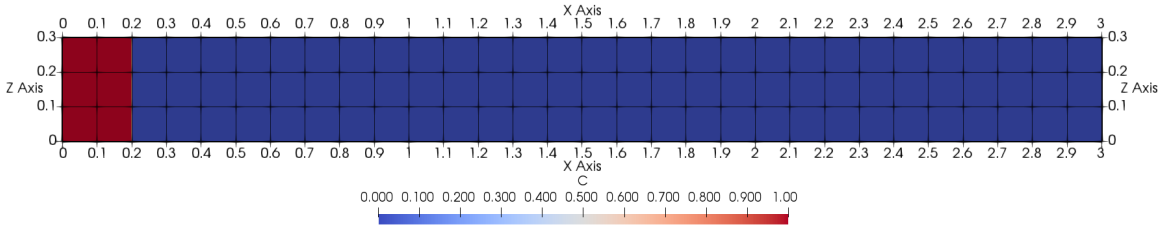

(a) t = 0 s

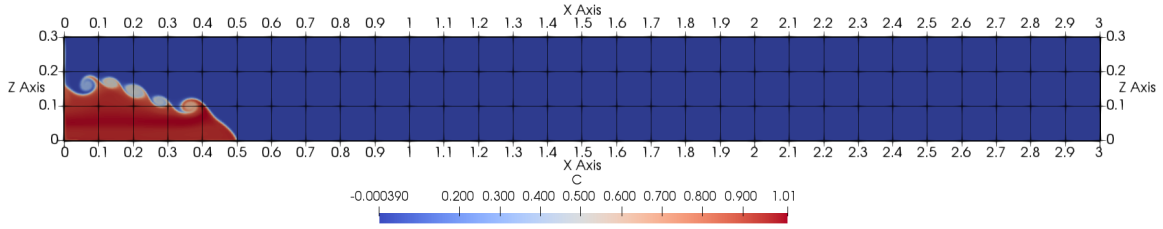

(b) t = 2 s

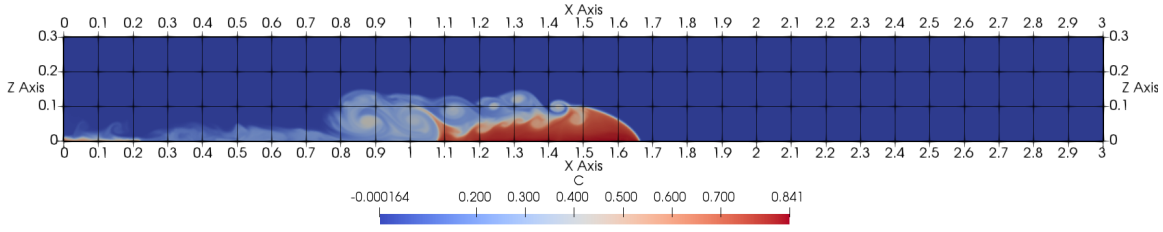

(c) t = 10 s

Figure 4.4: Gravity current propagation for cell size 2.5 mm.

Legend in Fig. 4.4 represents concentration as fraction of water with higher density in water at every cell of the domain, thus, red zone, which corresponds to value of one in the legend, is the zone fully comprised of water with higher density. Conversely, blue

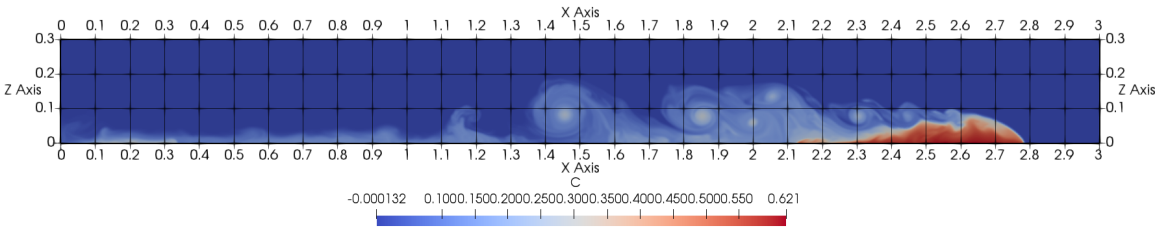

(d) t = 20 s

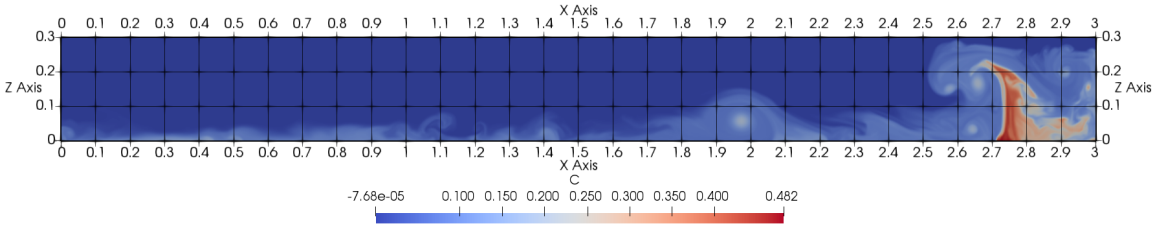

(e) t = 30 s

Figure 4.4: Gravity current propagation for cell size 2.5 mm.

zone, represented by zero in the legend, has no water of higher density in it, therefore it is fresh water. As time advances, more colours appear in snapshots as a result of mixing: share of water with higher density increases in the area where gravity current propagates. In Fig, 4.4a (t = 0), simulation has not started yet, therefore the scale contains values [0,1]. Rescaling at t = 2 s (Fig. 4.4b) shows that concentration in the core of the gravity current remains predominantly $c = 1$. Further rescaling at t = 10 s (Fig. 4.4) yields $c = 0.841$ in the core of the current and $c \simeq 0.3$ in its tail. By the time current front reaches the point of 2.8 m (t = 20 s, Fig. 4.4d) concentration in the core drops to $c = 0.621$, while concentration in its tail is mainly $c \simeq 0.300$. At the end of the simulation (t = 30 s, Fig. 4.4e) concentration in the core is $c = 0.482$, in the area surrounding the core at the right end of the tank it is $c \simeq 0.300$ with some inclusions of zones with higher concentration. In the trail along the bottom of the tank it is $c \simeq 0.200$. It can be seen that mixing increases for the case in question, compared to the previous case (Fig. 4.3).

4.1.2 Numerical Model with LES approach to turbulence

In order to reduce computational cost of models, Large Eddies Simulation model is implemented and tested for cell sizes considered above. After that, dimensionless time versus dimensionless space plots of models with LES model of turbulence are compared to those of simulations with no turbulence modelling so as to establish whether they yield similar results.

VT1: cell size 20 mm

Cell size of 20 mm is under consideration for a simulation with LES modelling of turbulence. Legend in Fig. 4.5 represents concentration as fraction of water with higher density in water at every cell of the domain, thus, red zone, which corresponds to value of one in the legend, is the zone fully comprised of water with higher density. Conversely, blue zone, represented by zero in the legend, has no water of higher density in it, therefore it is fresh water. As time advances, more colours appear in snapshots as a result of mixing: share of water with higher density increases in the area where gravity current propagates. In Fig, 4.5a (t = 0), simulation has not started yet, therefore the scale contains values [0,1]. However, at time instant t = 2 s (Fig. 4.5b) rescaling is done so as to keep gravity current clear and estimate the highest concentration in the numerical tank at the given time instant: concentration in the core of the gravity current is estimated to be $c = 0.893$. Further rescaling at t = 10 s (Fig. 4.5) yields $c = 0.951$ in the core of the current and $c \simeq 0.2$ in its tail, however, it must be noted that the area of mixed water is considerably smaller than that obtained in simulation without any turbulence model (Fig. 4.1). By the time current front reaches the point of 2.2 m (t = 20 s, Fig. 4.5d) concentration in the core drops to $c = 0.429$, while concentration in its tail is predominantly $c \simeq 0.1$. At the time instant t = 30 s, Fig. 4.5e) concentration in the core is $c = 0.241$ and in the tail it decreases to $c \simeq 0.06$. At the end of the simulation (t = 60 s, Fig. 4.5f) registered concentration in the core is $c = 0.067$, whereas in the trail along the bottom of the tank it reaches level of $c \simeq 0.01$ in the first part of the tank and in the area adjacent to the core. These two zones are separated bu the gap where $c \simeq 0$. Mixing it dramatically enhanced in the simulation under consideration, compared to the simulation with similar cell size but with no turbulence modelling (Fig. 4.1).

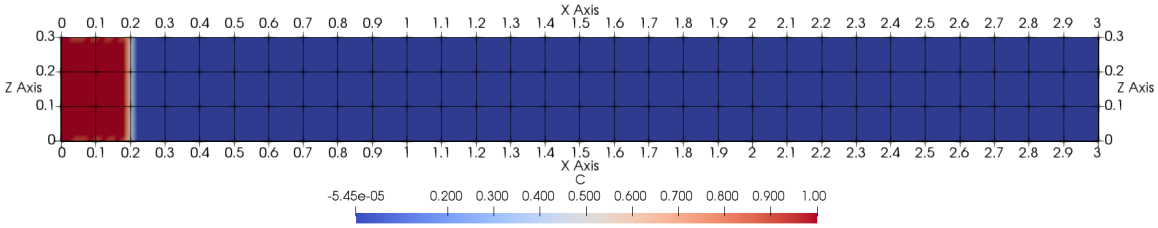

(a) t = 0 s

Figure 4.5: Gravity current propagation for cell size 20 mm.

Simple pattern of vortex formation are observed in the simulation with cell size of 20 mm, as observed in Fig. 4.5.

As shown in Fig. 4.6, gravity current front in the model with implemented LES propagates much slower than in the case without turbulence modelling: it reached the end of the water tank at the time t = 36 s.

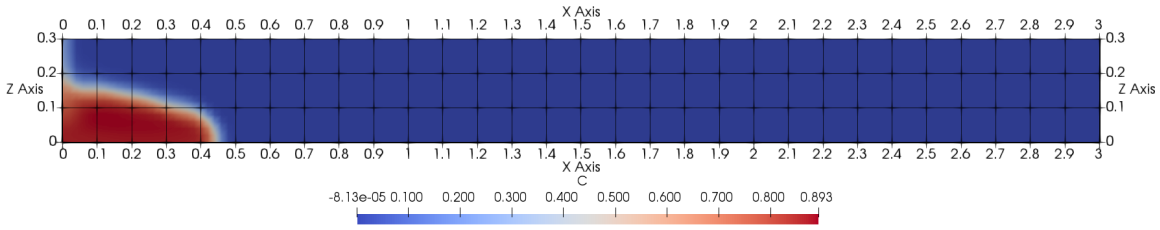

(b) t = 2 s

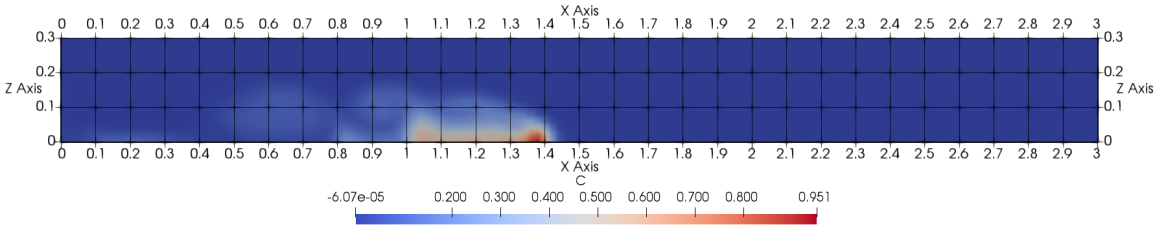

(c) t = 10 s

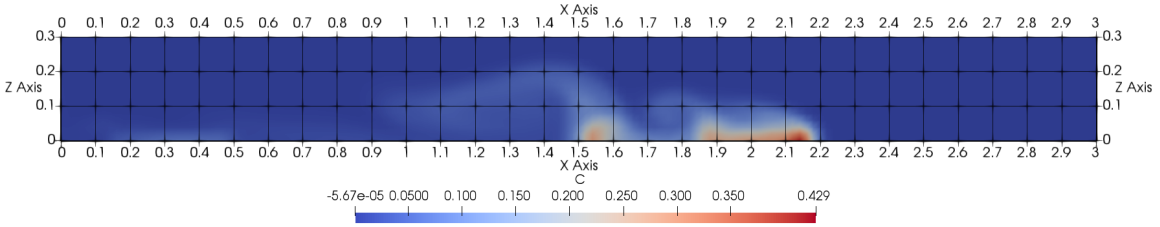

(d) t = 20 s

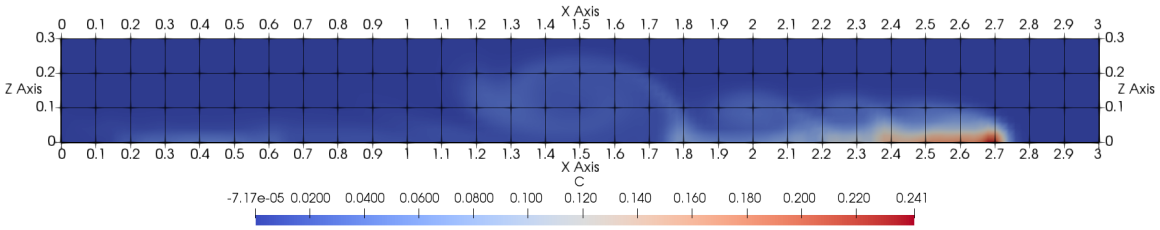

(e) t = 30 s

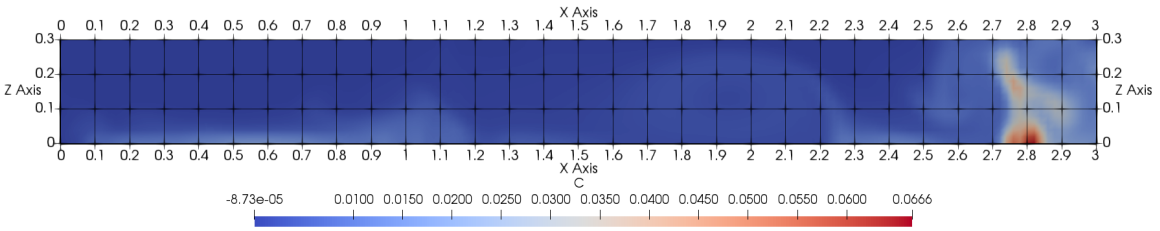

(f) t = 60 s

Figure 4.5: Gravity current propagation for cell size 20 mm.

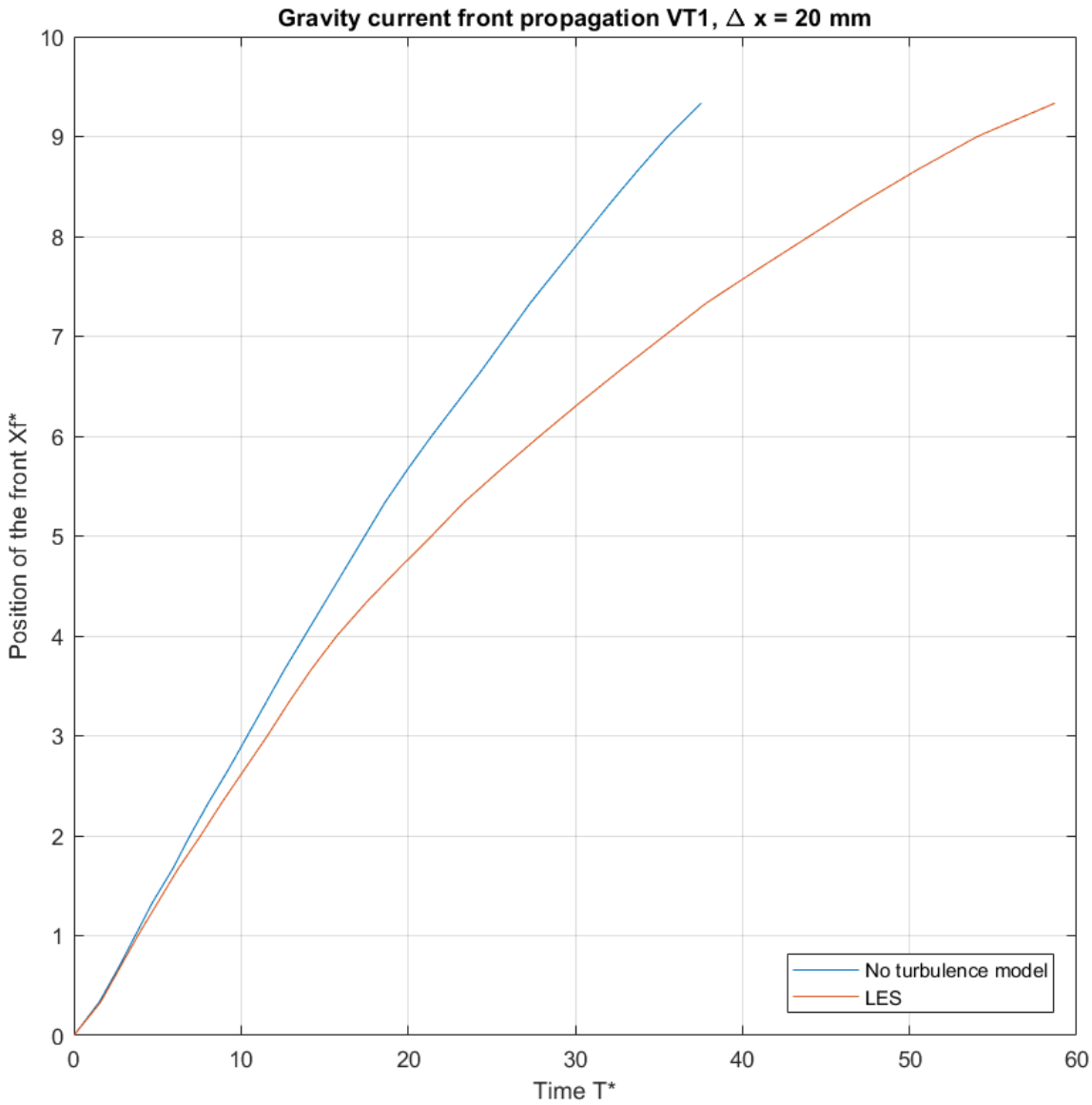

Figure 4.6: Comparison of current front propagation for cases with and without turbulence modelling for cell size of 20 mm

VT1: cell size 10 mm

Less coarse mesh brought about more detailed vortex formation. Legend in Fig. 4.7 represents concentration as fraction of water with higher density in water at every cell of the domain, thus, red zone, which corresponds to value of one in the legend, is the zone fully comprised of water with higher density. Conversely, blue zone, represented by zero in the legend, has no water of higher density in it, therefore it is fresh water.

As time advances, more colours appear in snapshots as a result of mixing: share of water with higher density increases in the area where gravity current propagates. In Fig, 4.7a (t = 0), simulation has not started yet, therefore the scale contains values [0,1]. However, at time instant t = 2 s (Fig. 4.7b) rescaling is done so as to keep gravity current clear and estimate the highest concentration in the numerical tank at the given time instant: concentration in the core of the gravity current is estimated to be $c = 0.871$. Further rescaling at t = 10 s (Fig. 4.7c) yields $c = 0.559$ in the core of the current and $c \simeq 0.2$ in its tail, however, it must be noted that the area of mixed water is considerably smaller than that obtained in simulation without any turbulence model (Fig. 4.2), but larger than that registered in the previous case (Fig. 4.5). By the time current front reaches the point of 2.0 m (t = 20 s, Fig. 4.7d) concentration in the core drops to $c = 0.179$, while concentration in its tail is predominantly $c \simeq 0.08$. At the time instant t = 30 s, (Fig. 4.7e) concentration in the core is $c = 0.102$ and in the tail it decreases to $c \simeq 0.04$. At the end of the simulation (t = 55 s, Fig. 4.7f) registered concentration in the core is $c = 0.022$, whereas in the trail along the bottom of the tank it reaches level of $c \simeq 0.004$ in the first part of the tank and in the area adjacent to the core. These two zones are separated by the gap where $c \simeq 0$. Mixing is further enhanced in the simulation under consideration, compared to the previous case (Fig. 4.5).

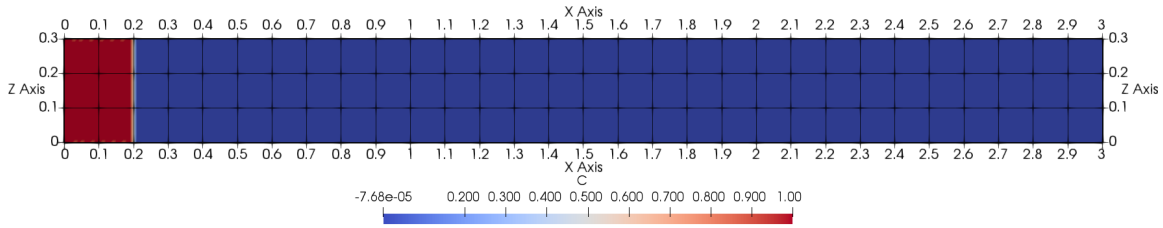

(a) t = 0 s

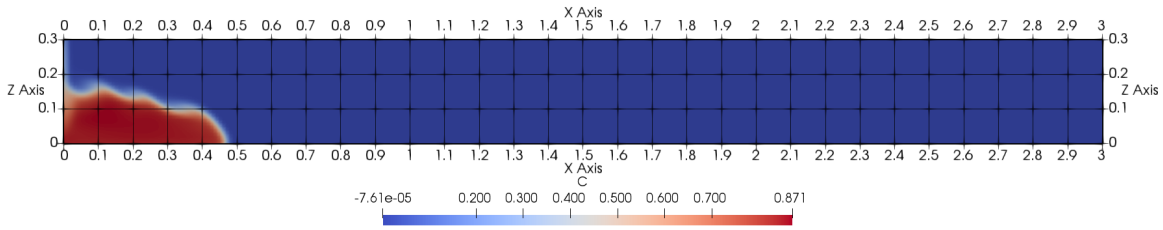

(b) t = 2 s

Figure 4.7: Gravity current propagation for cell size 10 mm.

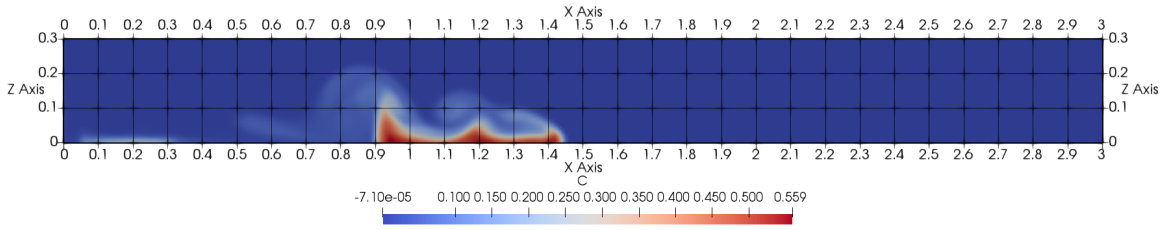

(c) t = 10 s

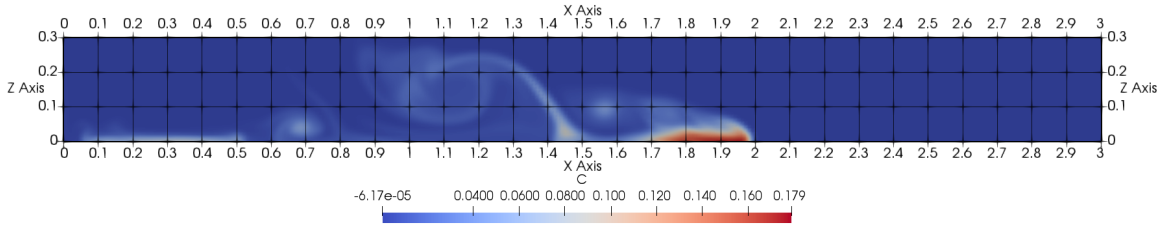

(d) t = 20 s

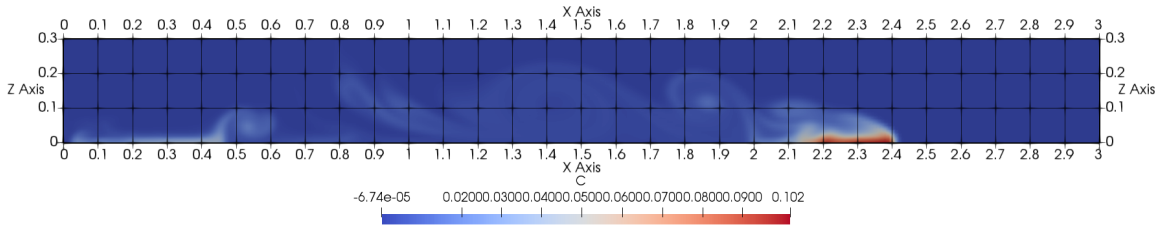

(e) t = 30 s

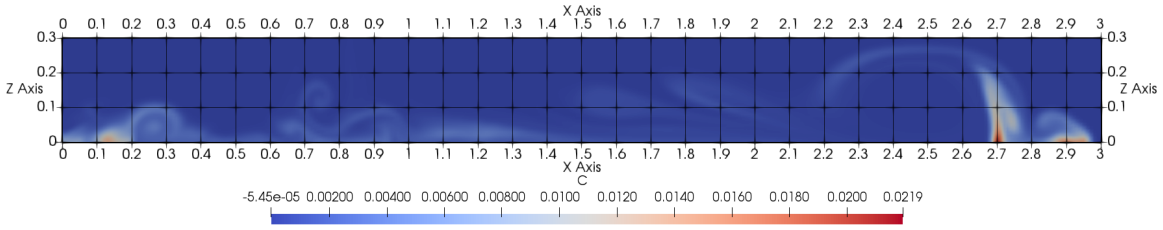

(f) t = 55 s

Figure 4.7: Gravity current propagation for cell size 10 mm.

As can be seen in Fig. 4.8, gravity current front reaches the end of the tank at the time t = 55 s, whereas for the coarser mesh with the cell size of 20 mm (Fig. 4.6), as well as for more fine mesh (Fig. 4.10) it reaches the end of the tank much faster.

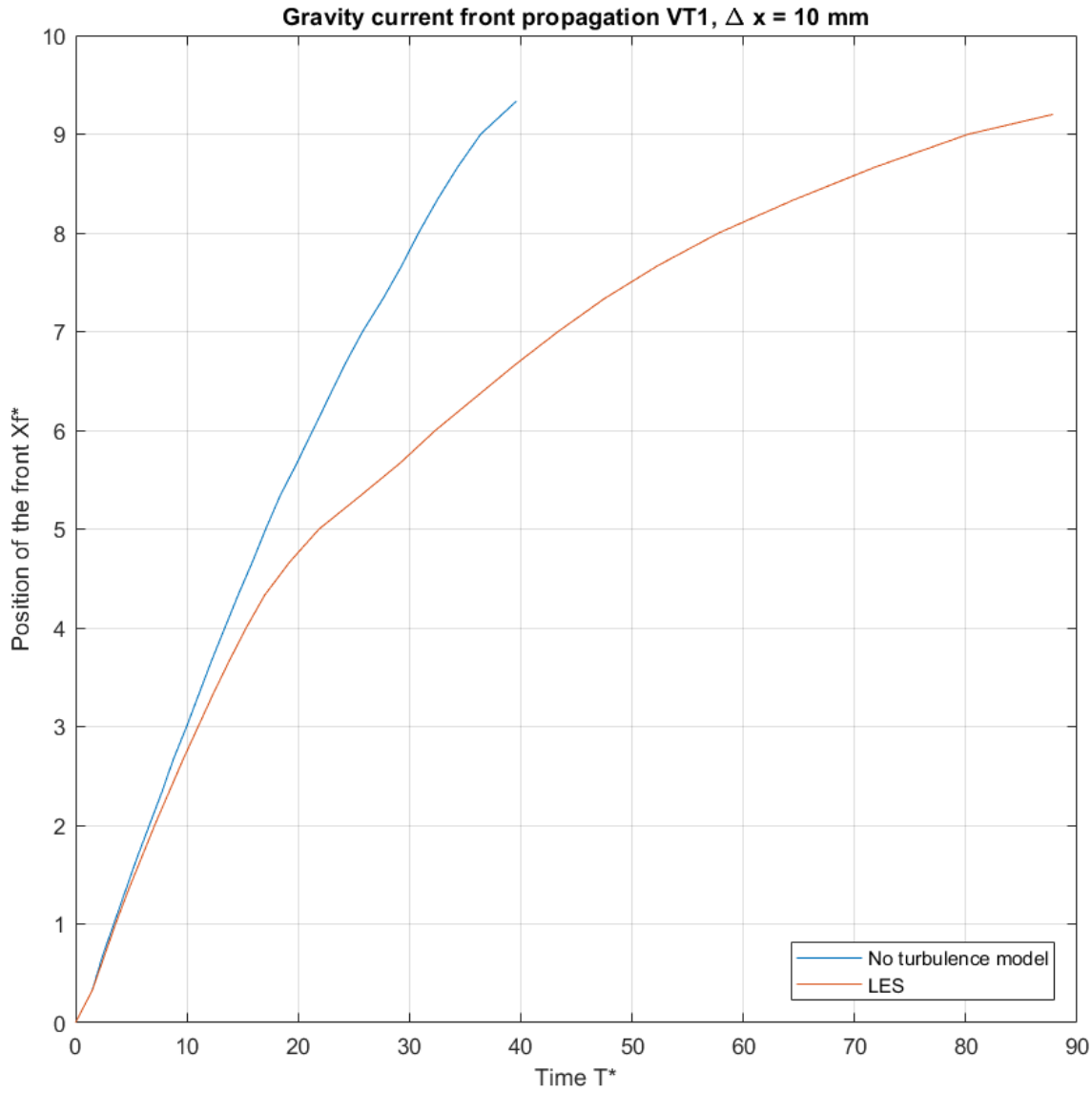

Figure 4.8: Comparison of current front propagation for cases with and without turbulence modelling for cell size of 10 mm

VT1: cell size 5 mm

As expected, fine mesh results in more detailed pattern of vortices (Fig. 4.9). Legend in Fig. 4.9 represents concentration as fraction of water with higher density in water at every cell of the domain, thus, red zone, which corresponds to value of one in the legend, is the zone fully comprised of water with higher density. Conversely, blue zone, represented by zero in the legend, has no water of higher density in it, therefore it is fresh water.

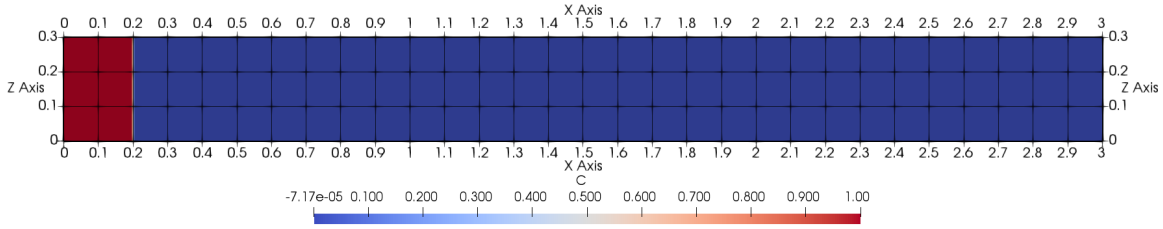

(a) t = 0 s

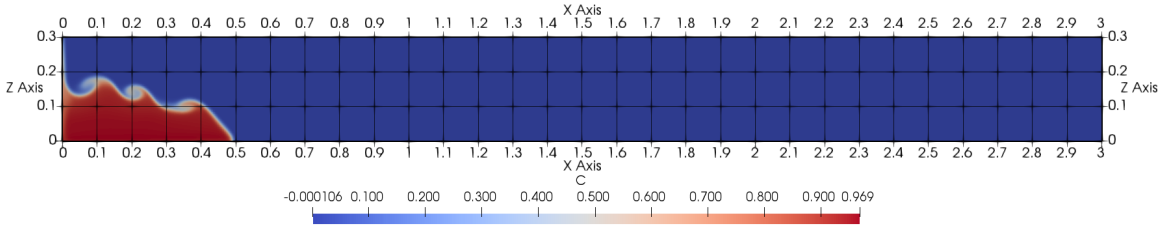

(b) t = 2 s

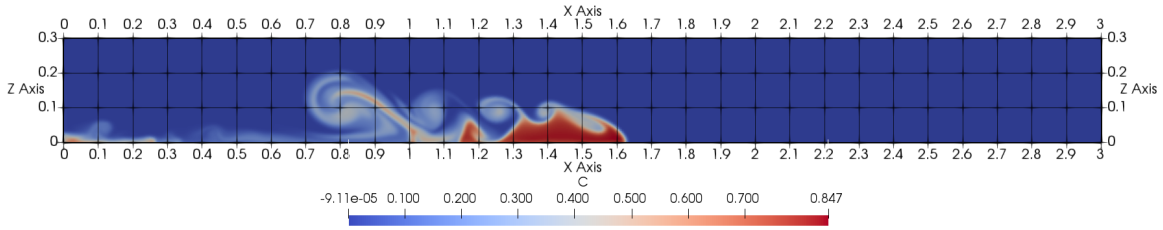

(c) t = 10 s

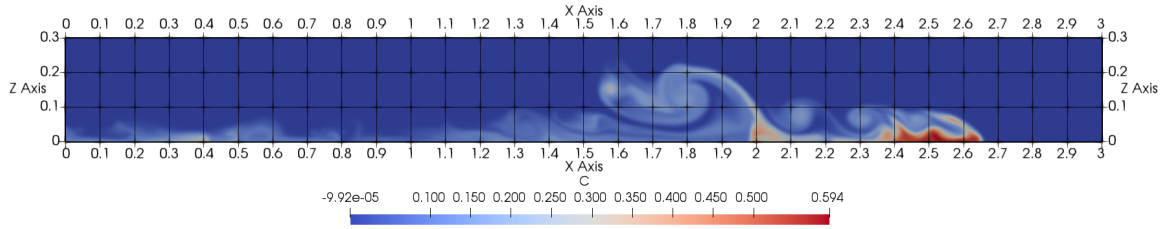

(d) t = 20 s

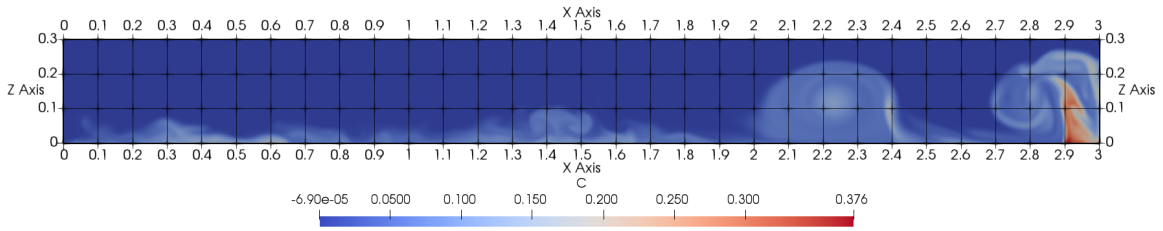

(e) t = 30 s

Figure 4.9: Gravity current propagation for cell size 5 mm.

As time advances, more colours appear in snapshots as a result of mixing: share of water with higher density increases in the area where gravity current propagates. In

Fig, 4.9a (t = 0), simulation has not started yet, therefore the scale contains values [0,1]. However, at time instant t = 2 s (Fig. 4.9b) rescaling is done so as to keep gravity current clear and estimate the highest concentration in the numerical tank at the given time instant: concentration in the core of the gravity current is estimated to be $c = 0.969$. Further rescaling at t = 10 s (Fig. 4.9) yields $c = 0.847$ in the core of the current and $c \simeq 0.3$ in its tail. By the time current front reaches the point of 2.65 m (t = 20 s, Fig. 4.9d) concentration in the core drops to $c = 0.594$, while concentration in its tail is predominantly $c \simeq 0.200$. At the end of the simulation (t = 30 s, Fig. 4.9e) registered concentration takes value $c = 0.376$ in the core and $c \simeq 0.250$ in the area surrounding the core. The trail of the current along the tank bottom is characterized by concentrations in range [0.100,0.150]. Compared to previous cases, mixing in the case under consideration is decreased, which can be explained by the fact that more turbulence vortices are resolved directly.
It is shown in Fig. 4.10 that for the cell size of 5 mm propagation speed of the gravity current front for model with LES becomes closer to that of simulation without any turbulence model, nevertheless, it is still slower.

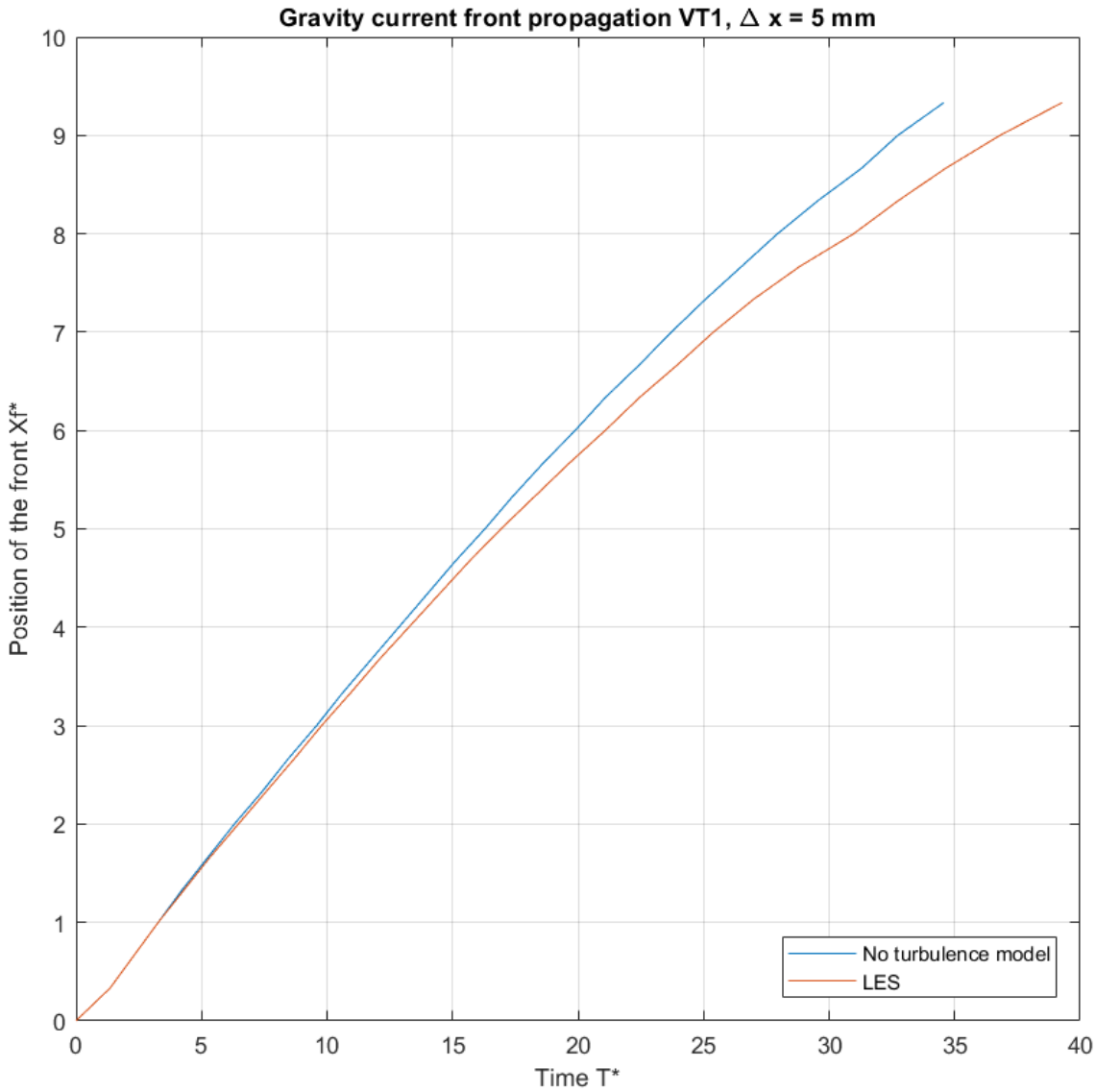

Figure 4.10: Comparison of current front propagation for cases with and without turbulence modelling for cell size of 5 mm

VT1: cell size 2.5 mm

Rich, detailed patterns of vortices in the model with the cell size of 2.5 mm (Fig. 4.11) are reminiscent of those observed in similar model where turbulent eddies are resolved directly (Fig. 4.4). Legend in Fig. 4.11 represents concentration as fraction of water with higher density in water at every cell of the domain, thus, red zone, which corresponds to value of one in the legend, is the zone fully comprised of water with higher density. Conversely, blue zone, represented by zero in the legend, has no

water of higher density in it, therefore it is fresh water.

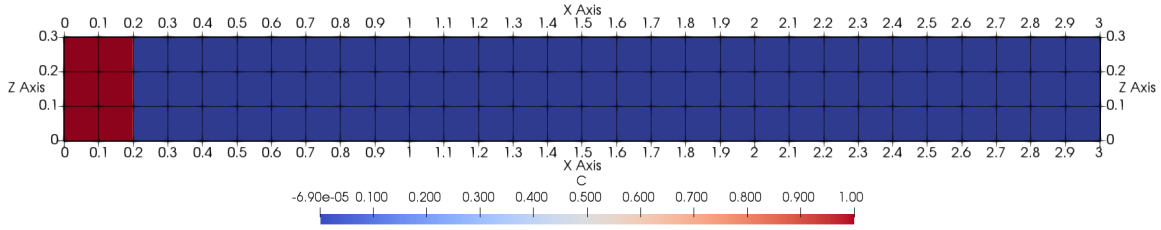

(a) t = 0 s

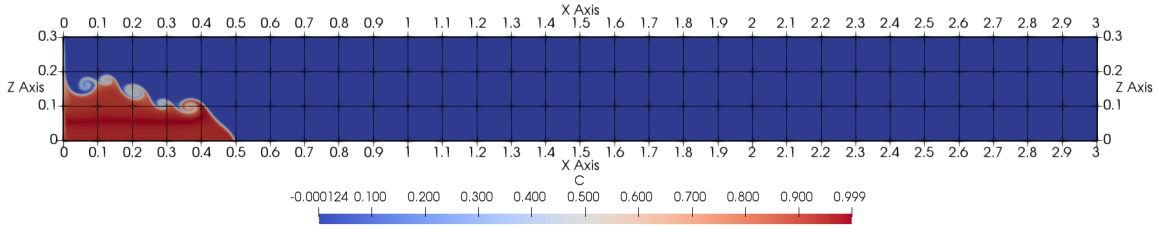

(b) t = 2 s

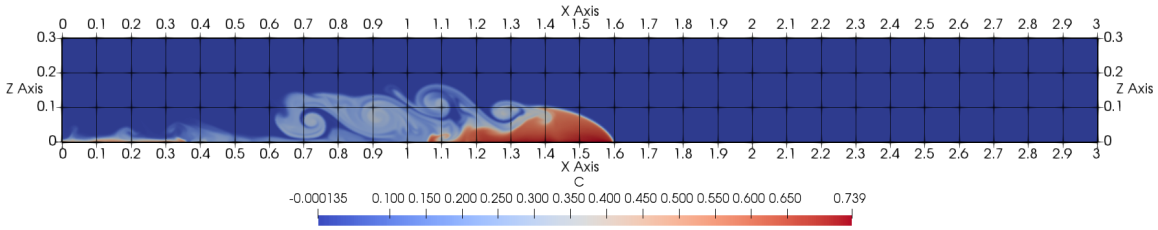

(c) t = 10 s

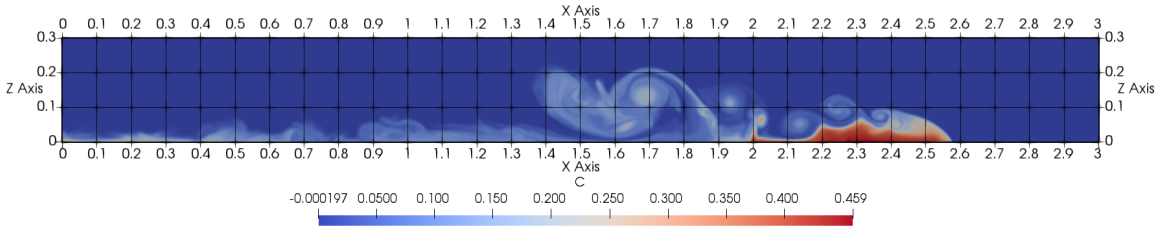

(d) t = 20 s

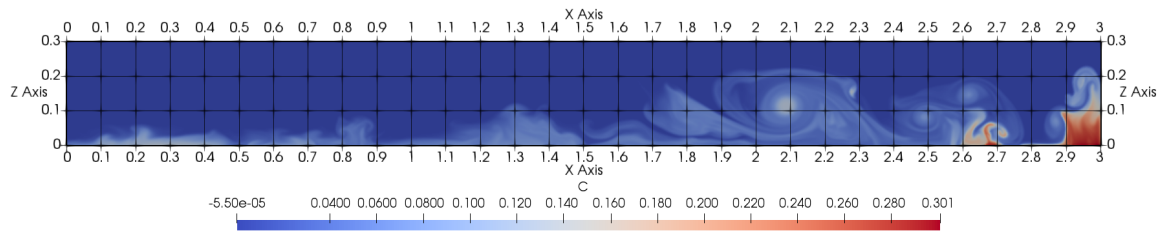

(e) t = 30 s

Figure 4.11: Gravity current propagation for cell size 5 mm.

As time advances, more colours appear in snapshots as a result of mixing: share of water with higher density increases in the area where gravity current propagates. In Fig, 4.11a (t = 0), simulation has not started yet, therefore the scale contains values [0,1]. However, at time instant t = 2 s (Fig. 4.11b) rescaling is done so as to keep gravity current clear and estimate the highest concentration in the numerical tank at the given time instant: concentration in the core of the gravity current is estimated to be $c = 0.999$. Further rescaling at t = 10 s (Fig. 4.11c) yields $c = 0.739$ in the core of the current and $c \simeq 0.350$ in its tail. By the time current front reaches the point of 2.58 m (t = 20 s, Fig. 4.11d) concentration in the core drops to $c = 0.459$, while concentration in its tail is predominantly $c \simeq 0.200$. At the end of the simulation (t = 30 s, Fig. 4.11e) concentration is registered varying in range [0.200,0.301] in the core. The trail of the current along the tank bottom is characterized by concentrations in range [0.040,0.160]. Compared to previous case, mixing in the case under consideration is generally increased, which stems from the fact that more vortices are resolved directly.

Propagation speed of the gravity current front for the model with LES, as can be seen in Fig. 4.12, is of the same order as the speed for the model without any turbulence model, however, the latter is faster. Difference in speed is not reduced (compared to the previous case) despite downsized cell size.

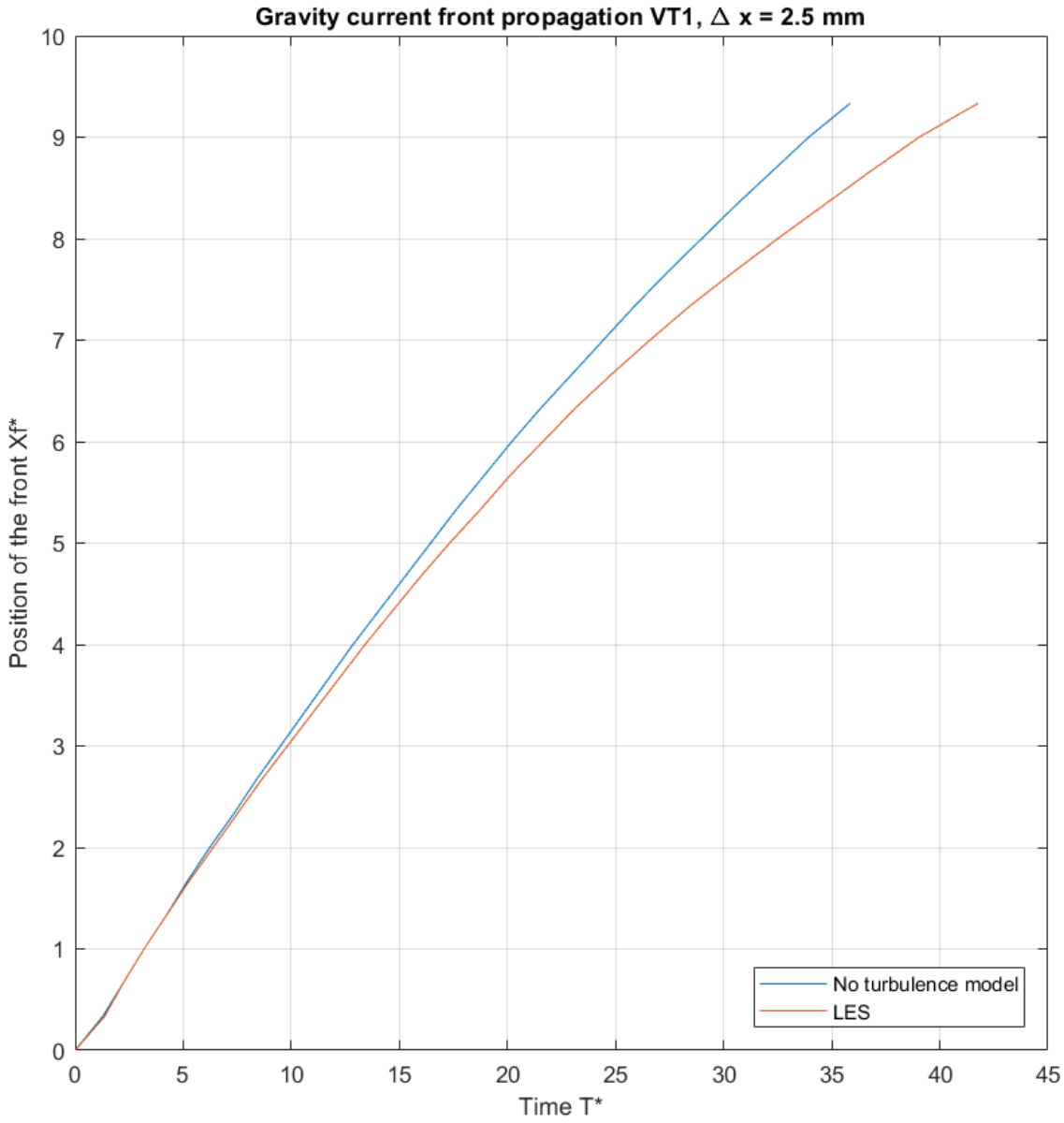

Figure 4.12: Comparison of current front propagation for cases with and without turbulence modelling for cell size of 2.5 mm

4.1.3 Grid Convergence Study

In this section, dimensionless time versus dimensionless space plots of gravity current front propagation, obtained in simulations with varying mesh sizes, are compared to similar plots from physical experiments.

Simulations without turbulence modelling

It can be seen in Fig. 4.13 that in models without any turbulence model, gravity current front propagation speed changes insignificantly with decreasing mesh size. Nonetheless, certain dependency is observed: numerical front propagation speed converges to that of physical model as the mesh becomes finer.

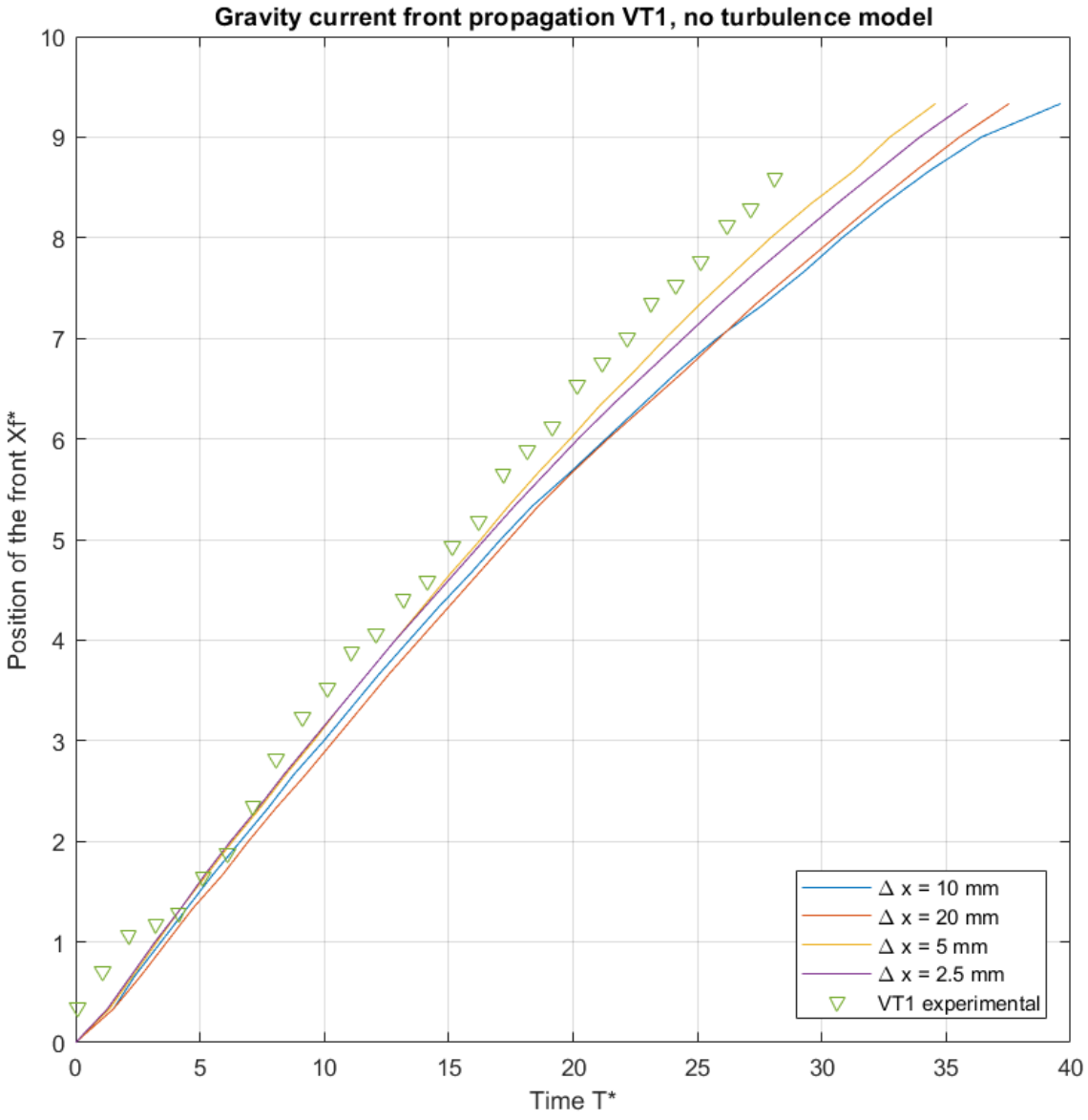

Figure 4.13: Grid Convergence (no turbulence modelling)

Models with implemented LES

In cases with LES modelling of turbulence, impact of the cell size on gravity current front propagation speed is more stark: only cases with 2.5 mm and 5 mm cell sizes yield front propagation speeds comparable to the speed obtained in physical experiments (Fig. 4.14). Simulation with 10 mm cell size stands out as it contradicts the trend of convergence of numerical speeds to the physical one as mesh becomes finer.

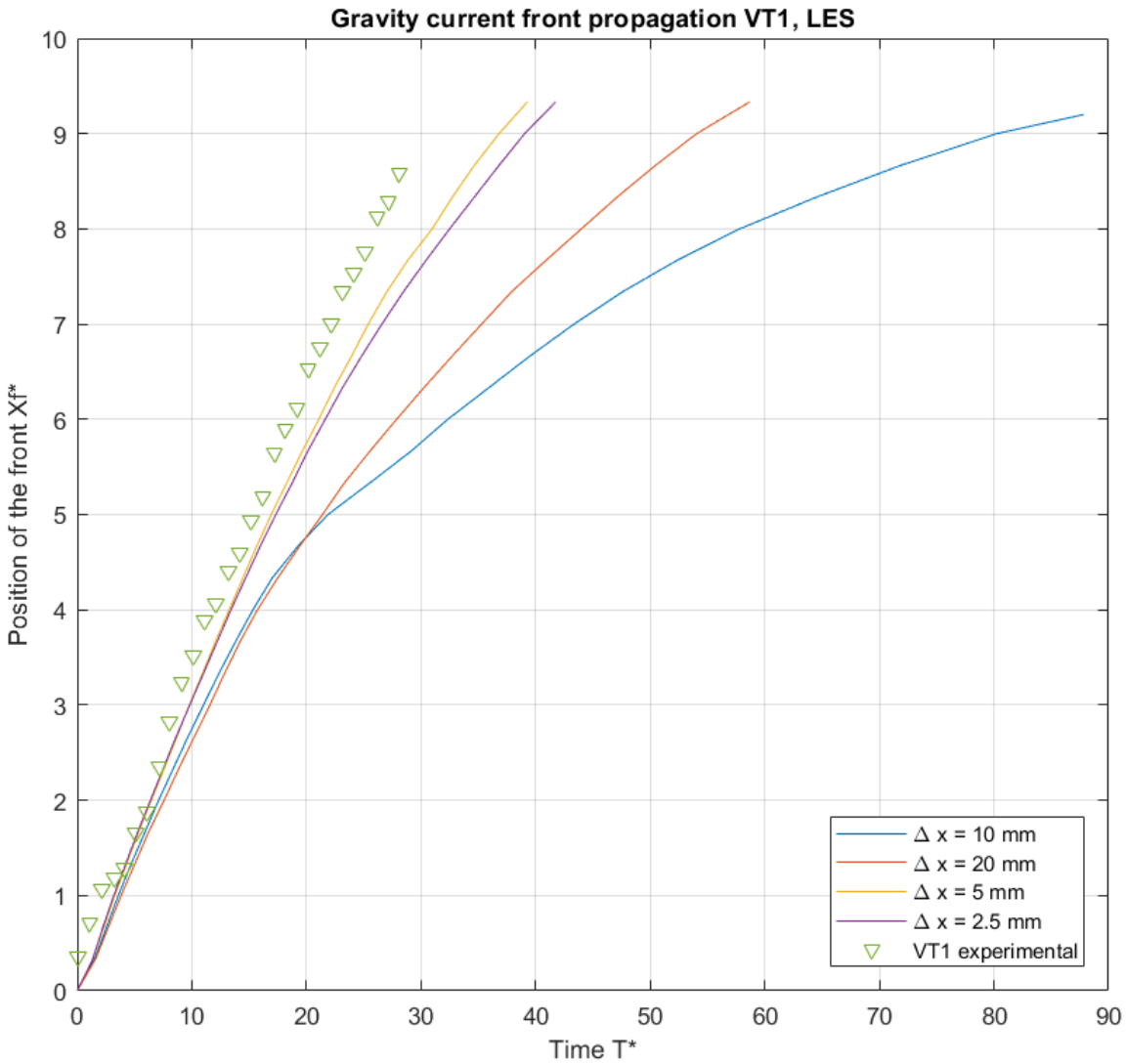

Figure 4.14: Grid Convergence (LES modelling of Turbulence)

4.1.4 VT4: Verification of the results

In previous subsection it was established that models without modelling of turbulence and with cell size of 5 mm or 2.5 mm are optimal for numerical modelling of gravity current development in two-dimensional setup. All simulations are performed with $\rho_1 = 1035\ kg/m^3$. Ensuring that same conclusion holds for different values of ρ_1 is of crucial importance, therefore numerical model for case VT4 (see table 4.1) with $\rho_1 = 1065\ kg/m^3$ is investigated. Results are presented in Fig. 4.15.

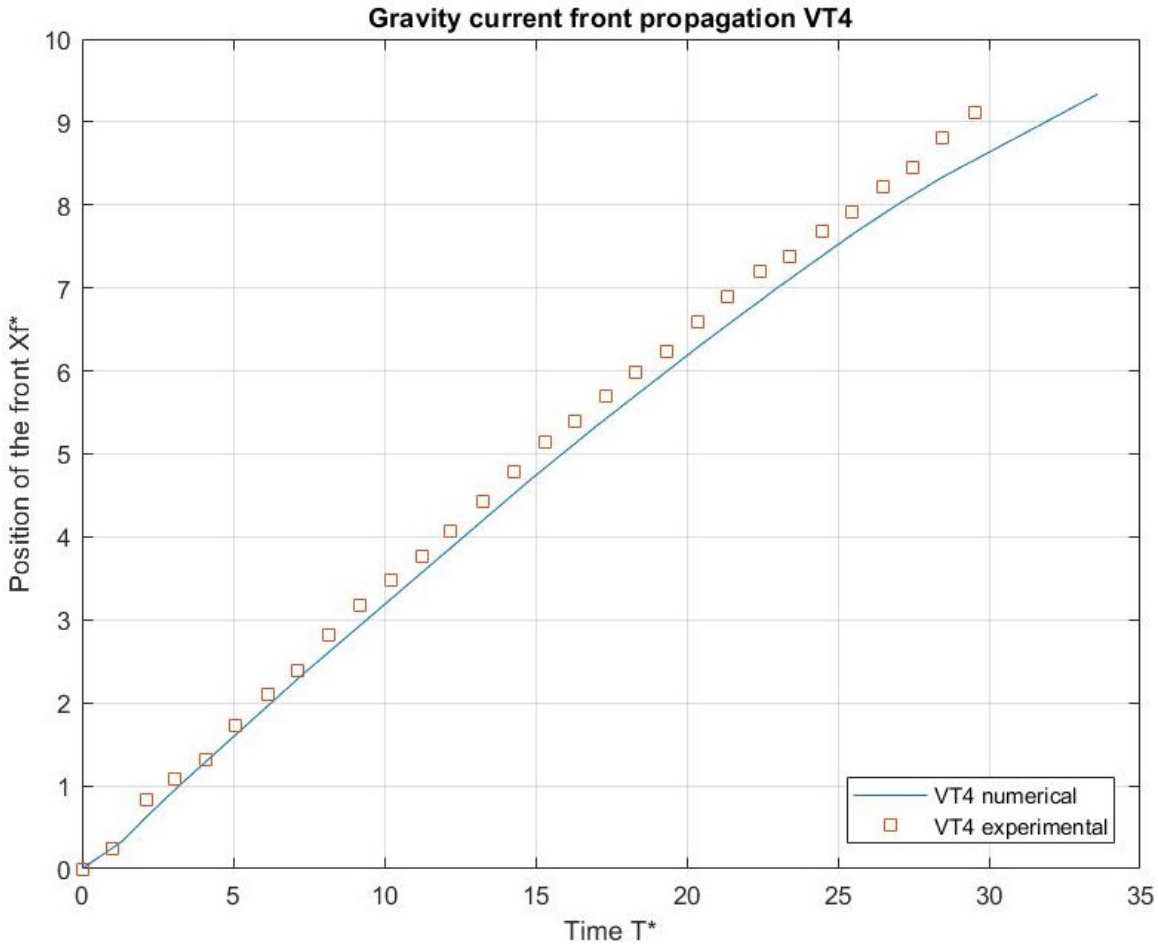

Figure 4.15: Gravity Current Propagation with $\rho_1 = 1065\ kg/m^3$

As can be seen in Fig. 4.15, gravity current front propagation speed, obtained through numerical modelling, is in good agreement with that obtained in physical experiments. Thus, it is arguably safe to conclude that parameters of cell size, as well as approach to turbulence, considered as optimal, are indeed optimal and can be used for modelling of gravity current front propagation in two-dimensional setup.

4.2 Three-dimensional gravity current

In this section, gravity current propagation in three-dimensional setup is considered. Simulations are performed with LES modelling of turbulence and without any turbulence model. After that, results are compared.

Gravity current develops in mushroom-like patterns: it not only propagates along the x-axis, but also along the y-axis. At different time instants position of the gravity current front is registered and then plotted so as to establish different phases of the development. Various values of ρ_1 were investigated in physical experiments, however, for the sake of simplicity, only one of them is chosen in this study.

4.2.1 Comparison of simulations with and without turbulence models

Similar experiments are performed in this study in a numerical tank, which is identical in its dimensions to the tank from physical experiments. LES modelling of turbulence is implemented and tested, after that results are compared to those obtained with model where turbulence eddies are resolved directly. After that, obtained gravity current front positions are compared to those obtained in physical experiments. Density of water in first reservoir is chosen $\rho_1 = 1025\ kg/m^3$. Cell size is set to 5 mm.

It can be seen in Fig. 4.16 that numerical and physical results are in arguably good agreement for both simulation with no modelling of turbulence and simulation with LES modelling of turbulence. Certain mismatch in shape develops for either simulations as time advances, however, propagation speed of the front in x direction is represented adequately.

Patterns of mixing are more detailed in the simulation with no turbulence modelling small vortices are abundant at each time instant, except for the first one (t = 2 s, Fig. 4.16a, Fig. 4.16b). However, simulation with implemented LES model of turbulence approximates impact of small-scale vortices arguably good. In addition, it yields front positions that are adequate to front positions from physical experiment, which brings to conclusion that this model is preferable to the one with no turbulence modelling as the latter is more computationally demanding.

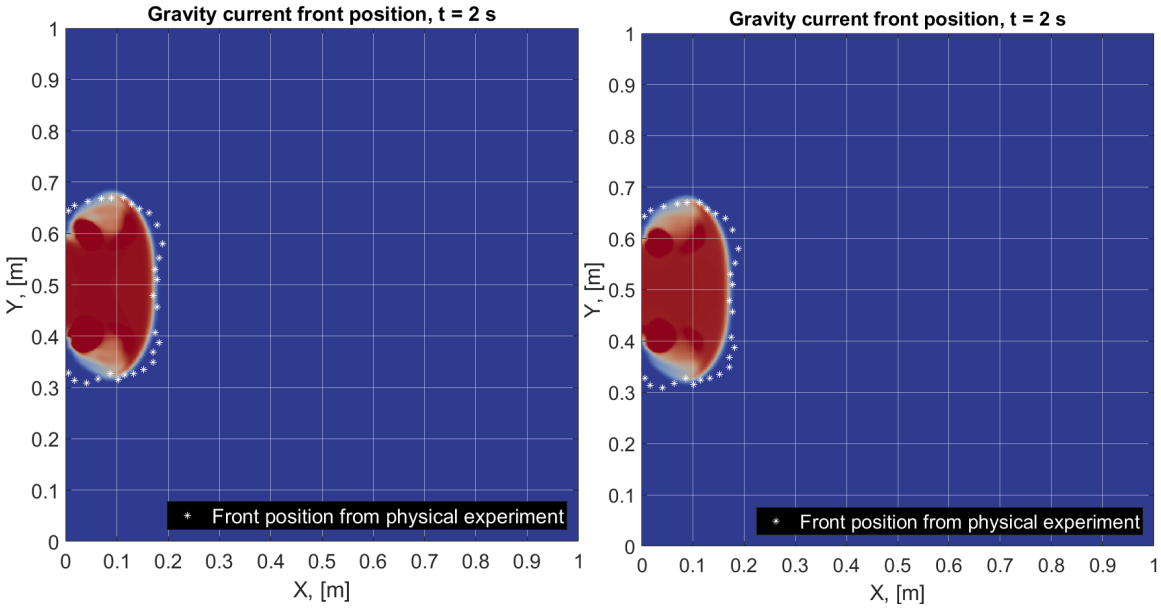

(a) t = 2 s, no turbulence modelling

(b) t = 2 s, LES

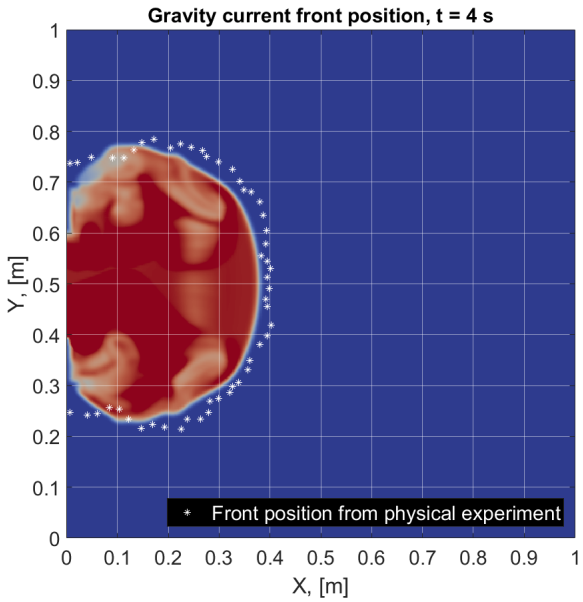

(c) t = 4 s, no turbulence modelling

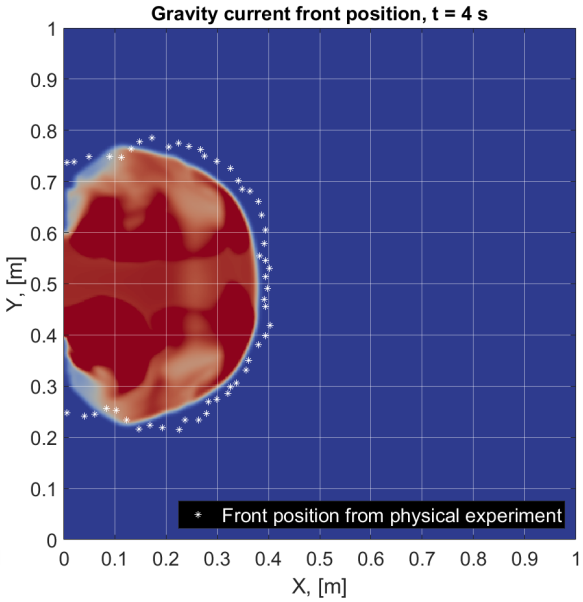

(d) t = 4 s, no LES

Figure 4.16: Three-dimensional gravity current

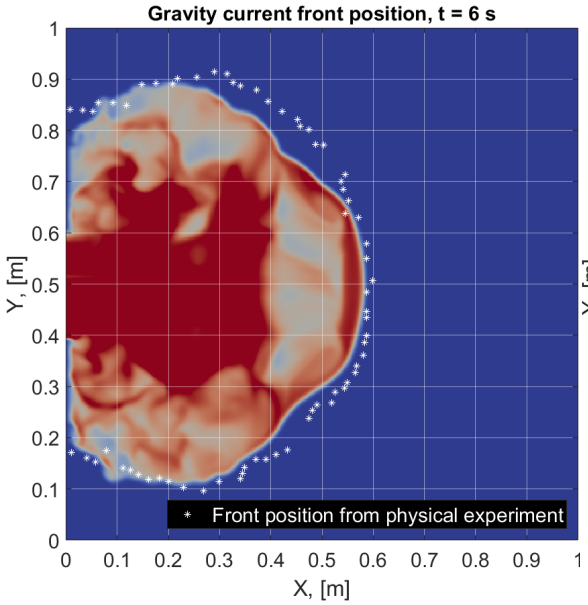

(e) t = 6 s, no turbulence modelling

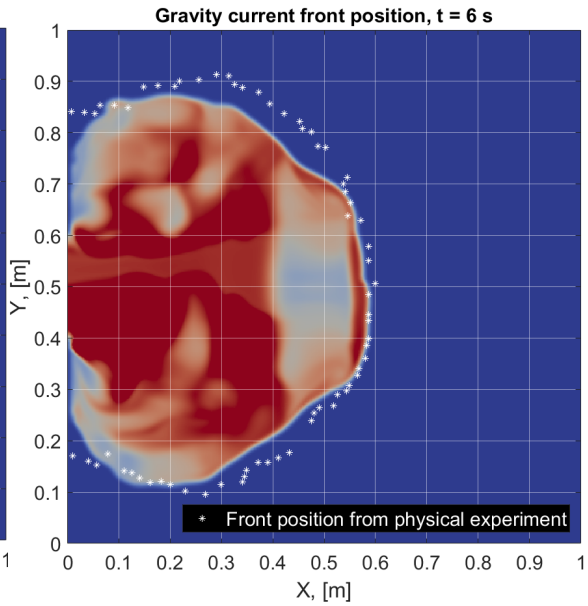

(f) t = 6 s, LES

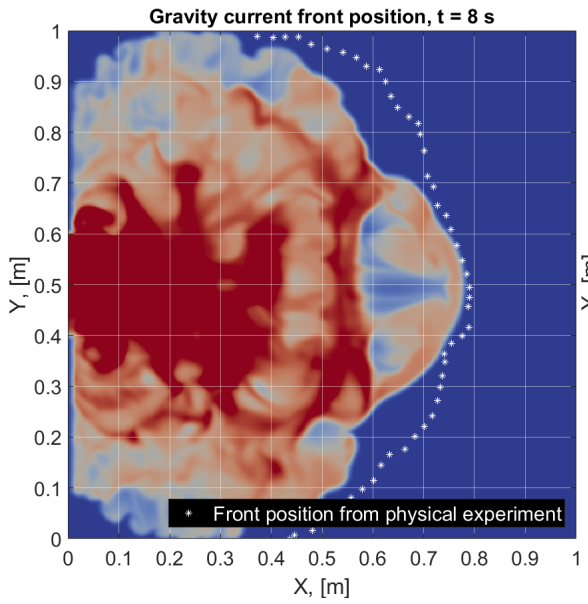

(g) t = 8 s, no turbulence modelling

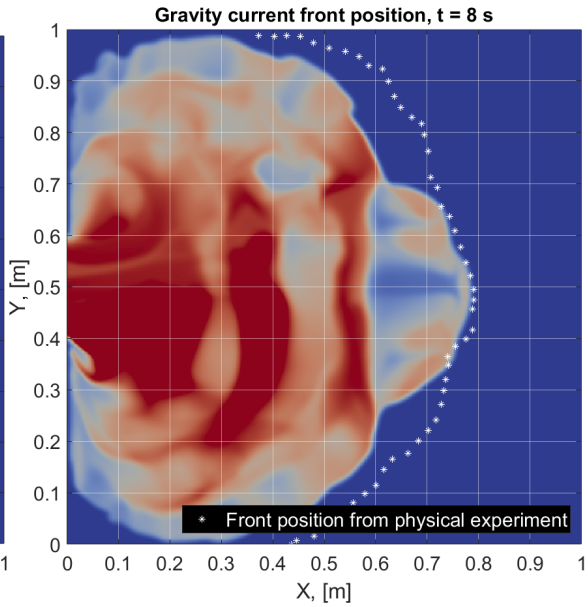

(h) t = 8 s, LES

Figure 4.16: Three-dimensional gravity current

Chapter 5

Water-Structure interaction of Submerged Floating Tube

In this chapter, Submerged Floating Tube (SFT) is considered. At first, cylinder is placed in homogeneous water so as to validate the model. After that, water layers of varying density are introduced, and their effect on forces acting upon the structure is investigated.

5.1 SFT in Homogeneous Water

One of the aims of the study is to understand how grid size and value of CFL criterion affects forces acting upon cylinder in homogeneous water in numerical model. Sizes of numerical tank differ from those of the tank used in physical experiments:

- Width of the tank is reduced to $b_T = 0.5$ m,
- Length of the tank is set to $L_T = 1.5$ m, and in certain cases with very fine grid, length is set to $L_T = 0.8$ m.

Reduction of sizes is done in order to decrease number of cells in numerical model, keeping it within 20 million cells. Limit arises from computational demands considerations.

At first, grid convergence study is performed so as to determine accuracy of computation. Following grid sizes are used:

- 10 mm,
- 5 mm,
- 2.5 mm.

After that, for all cases, in-line force acting upon the structure is obtained using two methods: via function, implemented in REEF3D, and via numerical integration of the pressure around the structure. The latter is employed as a reasonable estimate of accuracy of the former.

5.1.1 Numerical integration of pressure around the cylinder

Numerical probe points are placed around the cylinder at a distance of one cell size from it, see Fig. 5.1

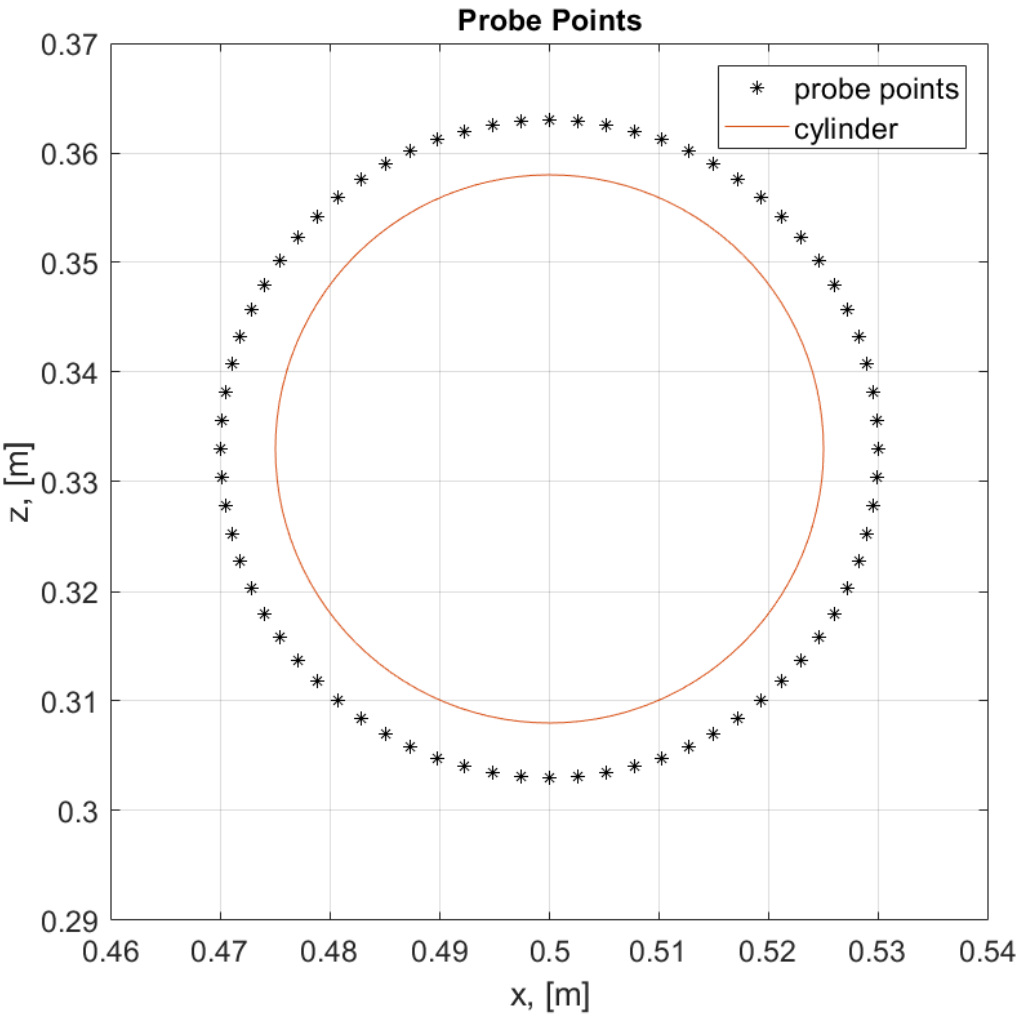

Figure 5.1: Probe points

There are 72 probe points used, one point per each $\pi/36$ rad in $[0, 2\pi]$ domain, meaning that distance between two adjacent points would be approximately 3 mm,

depending on the cell size of the case in question. Such length allowed for linear approximation in pressure distribution between two points, making numerical integration of pressure distribution possible (Fig. 5.2).

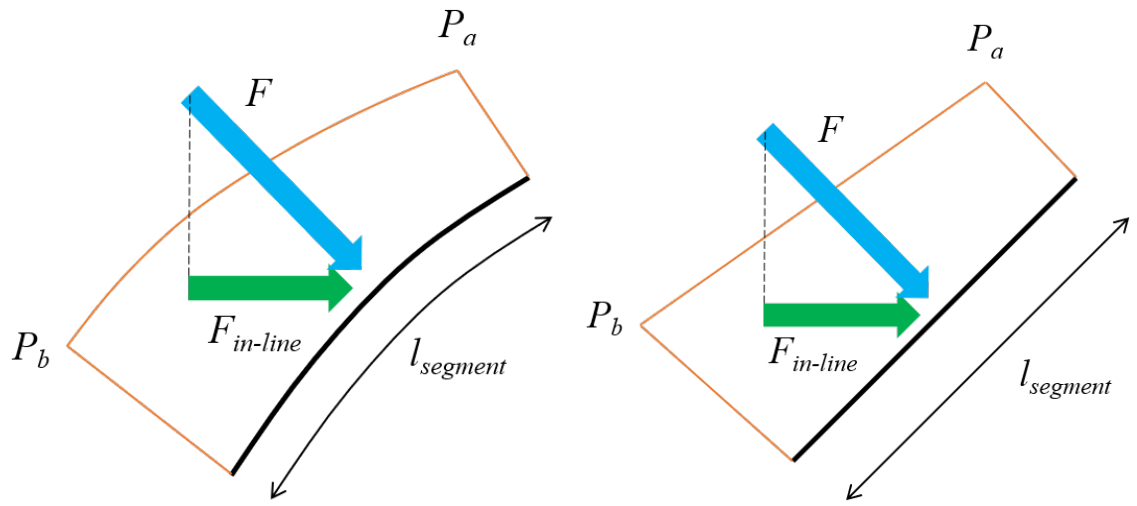

(a) Exact distribution (b) Linear approximation

Figure 5.2: Integration of pressure distribution

Total force acting on increment is calculated as follows:

$$F = 0.5(P_a + P_b)l \tag{5.1}$$

The sine component gives the horizontal component of the total force. Procedure is performed for each increment along the cylinder perimeter, after that corresponding horizontal forces are summed, which yields total in-line force.

5.1.2 Grid Convergence Study

As mentioned above, cell sizes of 2.5 mm, 5 mm and 10 mm are tested. Simulations are run with current speed of 10 cm/s, corresponding to discharge of 0.02 m^3/s for chosen tank width and water depth of 0.5 m and 0.4 m, respectively. Submergence of the cylinder is set to $z_0/D = 1.34$.

Cell size 10 mm

At first, coarse grid is investigated. For illustration purposes, hydrostatic component of pressure is subtracted from the total distribution, thus, pressure due to current is obtained, which is presented in Fig. 5.3. As mentioned in subsection 5.1.1, total pressure is registered via number of probe points that are evenly distributed around

the cylinder on a distance of one cell size from it. After hydrostatic component of pressure had been removed, in certain areas around the cylinder, namely top part and bottom part, pressures became negligible. Conversely, in areas upstream and downstream of the cylinder, pressures are significant, which is associated with water deceleration in the regions. Difference in these pressures constitutes the acting in-line force.

For calculation of force and drag coefficient, however, full distribution is used, as it is more precise. Hydrostatic component of pressure is cancelled out by itself as it acts on all sides. Numerical integration of pressure at probe points yields drag coefficient $C_D = 1.41$, which is lower compared to value obtained in physical experiments [27]: $C_D = 1.5$, but larger than free-stream drag coefficient for $Re \simeq 5000$, which is $C_{D,fr.str} = 1.2$, according to Sarpkaya and Isaacson [28].

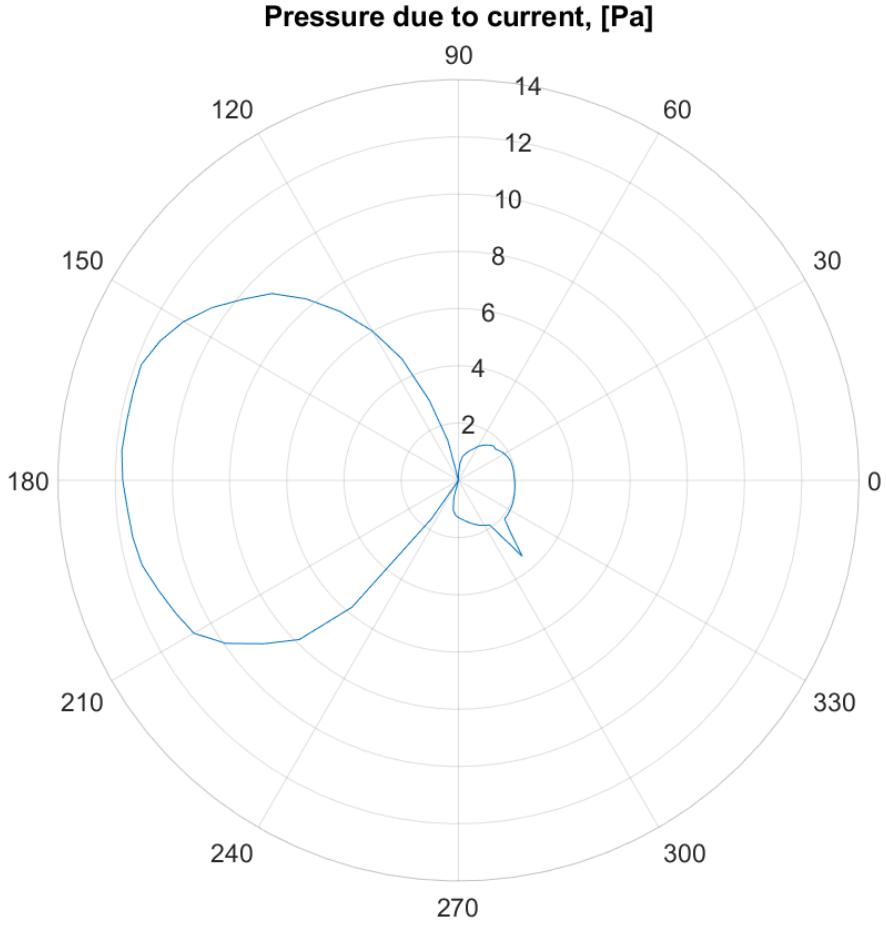

Figure 5.3: Pressure distribution for cell size of 10 mm

Function of force calculation within REEF3D yields drag coefficient $C_D = 1.69$, which is much higher than drag coefficient computed via numerical integration of pressures.

Cell size 5 mm

Less coarse grid is under consideration in this subsection. Hydrostatic component of pressure is subtracted from the total distribution, thus, pressure due to current is obtained, which is presented in Fig. 5.4 As explained in subsection 5.1.1, total pressure is registered via number of probe points that are evenly distributed around the cylinder on a distance of one cell size from it (in thic case, 5 mm). Distribution of pressure due to current for this case is similar to that for previous case of coarse mesh. After hydrostatic component of pressure had been removed, in top part and bottom part pressures became negligible. Conversely, in areas upstream and downstream of the cylinder, pressures are significant, which is associated with water deceleration in the regions. However, shape of distribution shown in Fig. 5.4 is slightly different from that of Fig. 5.3 : the former is more narrow, meaning that lower pressures are registered in regions [90;150] *deg* and [210,270] *deg*. In addition, pressures at probe points in the region [150,210] *deg* and behind the cylinder are higher for the case of finer grid.

For calculation of force and drag coefficient, however, full distribution is used, as it is more precise. Hydrostatic component of pressure is cancelled out by itself as it acts on all sides. Numerical integration of pressure at probe points yields drag coefficient $C_D = 1.25$, which is lower compared to value obtained in physical experiments: $C_D = 1.5$, but slightly larger than free-stream drag coefficient for $Re \simeq 5000$, which is $C_{D,fr.str} = 1.2$, according to Sarpkaya and Isaacson [28].

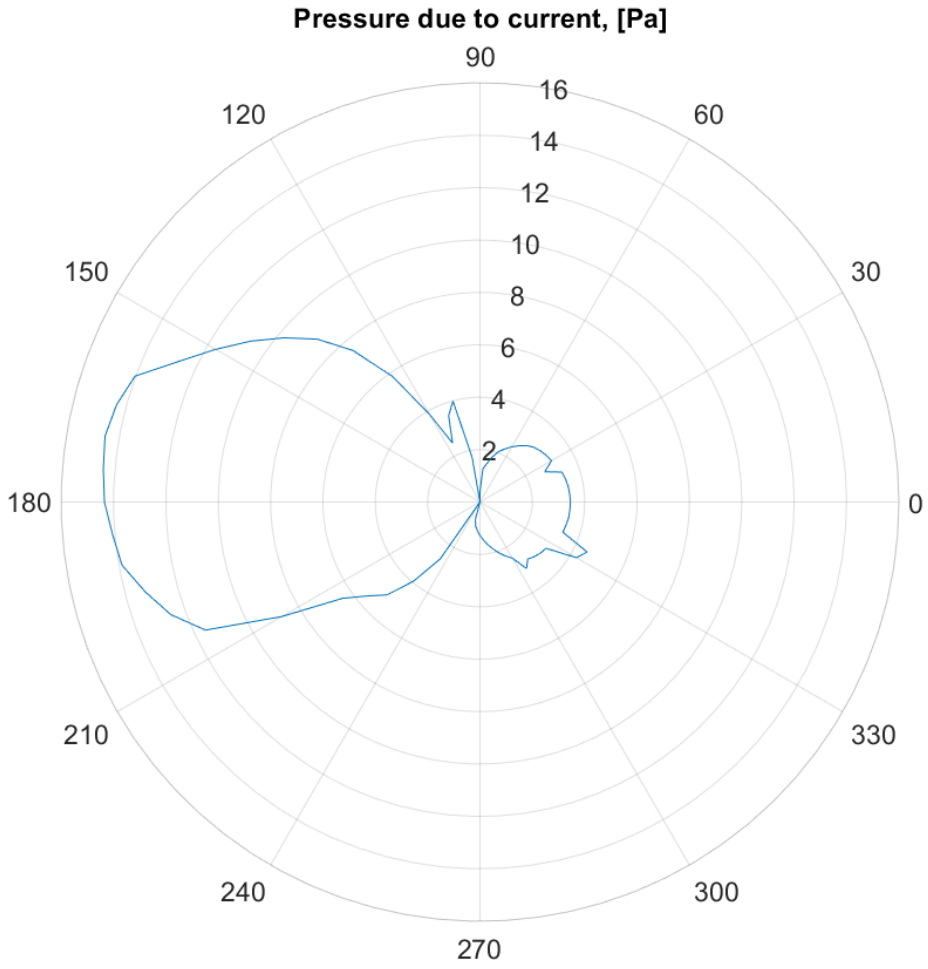

Figure 5.4: Pressure distribution for mesh size of 5 mm

Function of force calculation within REEF3D yields drag coefficient $C_D = 0.98$, which is much lower than all drag coefficients mentioned above.

In Fig. 5.5, steady state development is shown by means of velocity profiles at different time instants for the case of finer grid of 5 mm. It can be seen that steady state is reached at $t \simeq 15$ s. White contour in the middle of each snapshot depicts surface elevation. For the sake of convenience, velocity profiles at different time instants are provided only for this model, as development of low velocity zone behind the cylinder is identical for all cases.

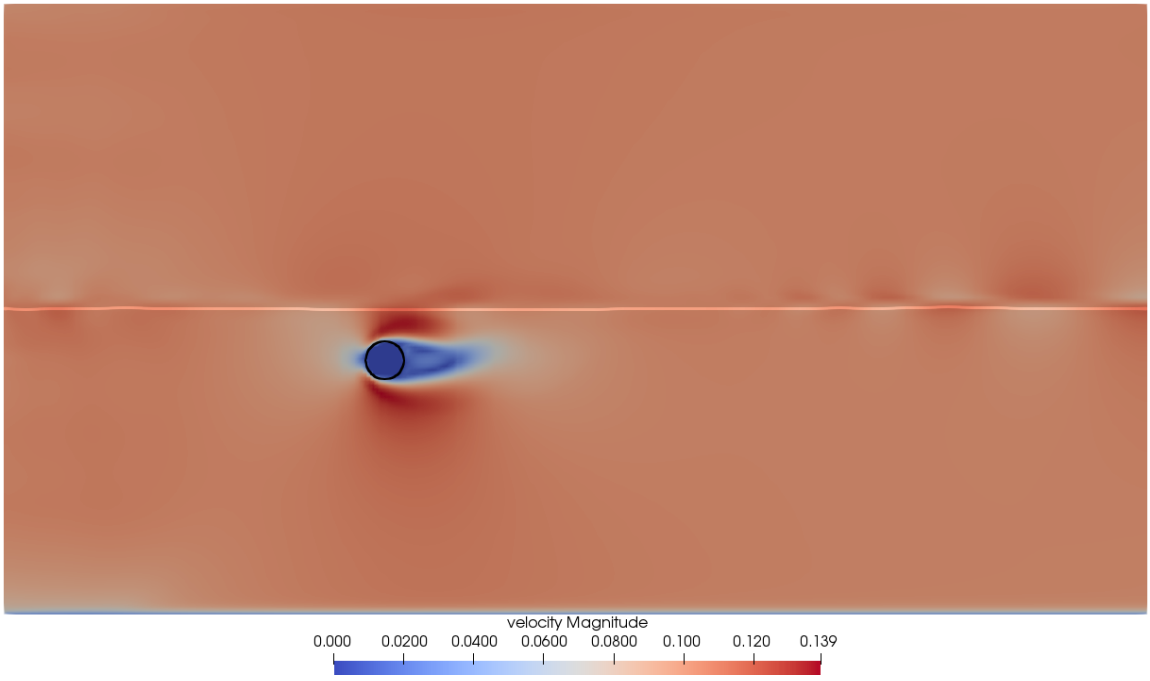

(a) t = 2 s

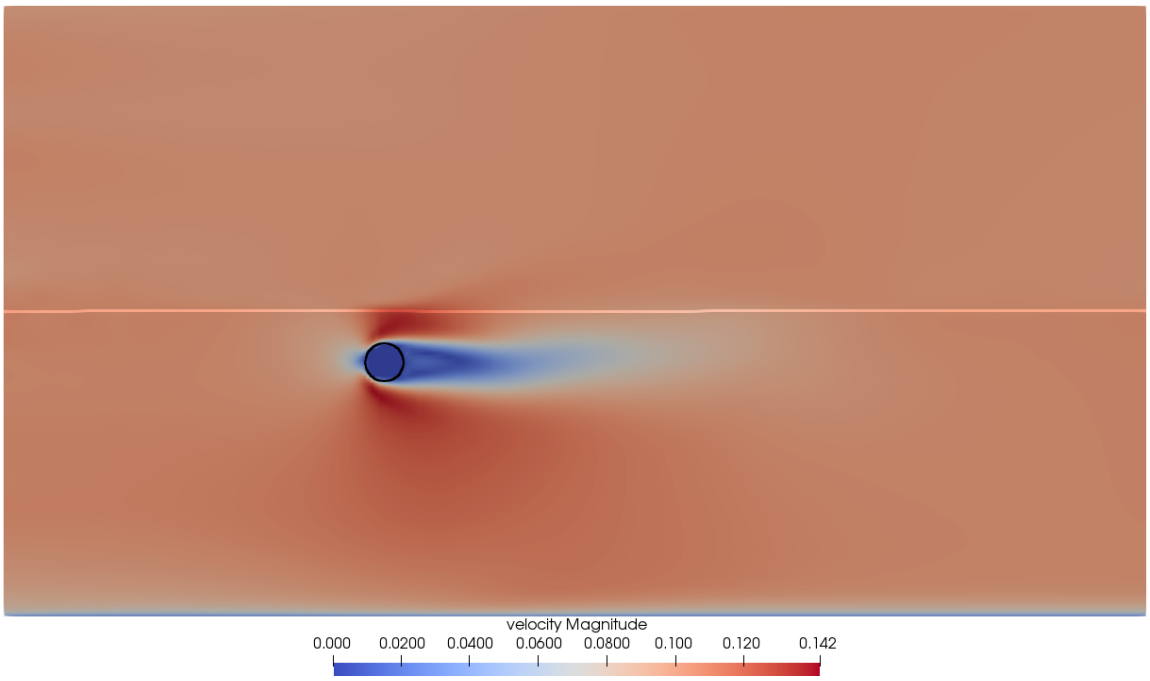

(b) t = 6 s

Figure 5.5: Velocity at different time instants. Development of steady state

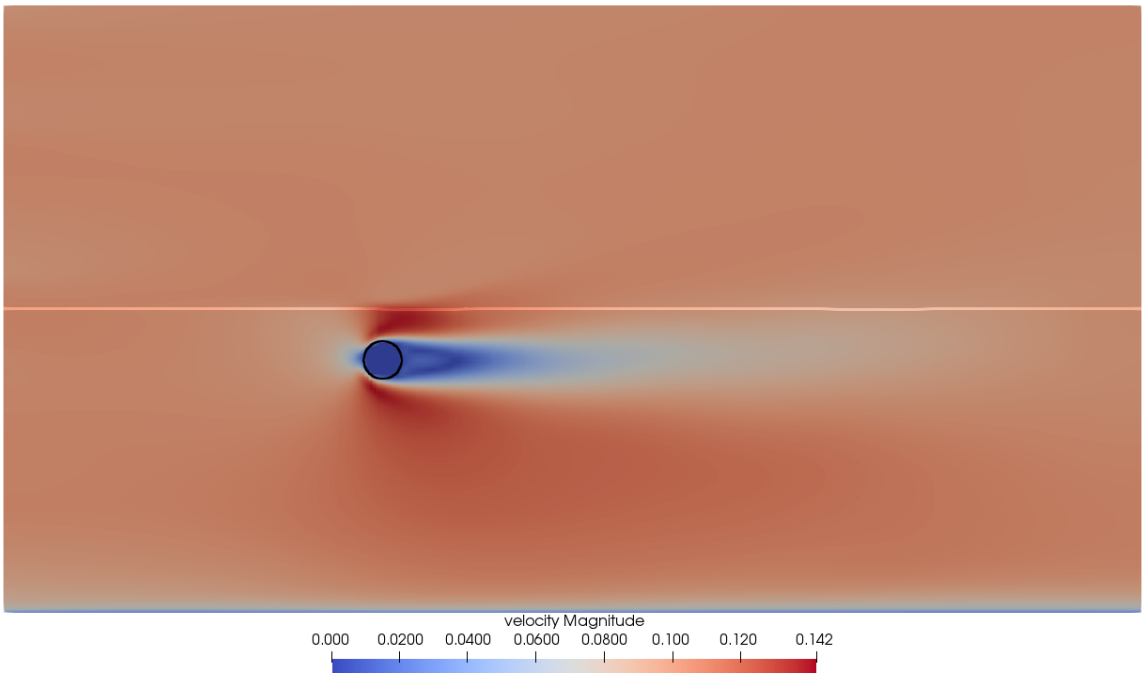

(c) t = 10 s

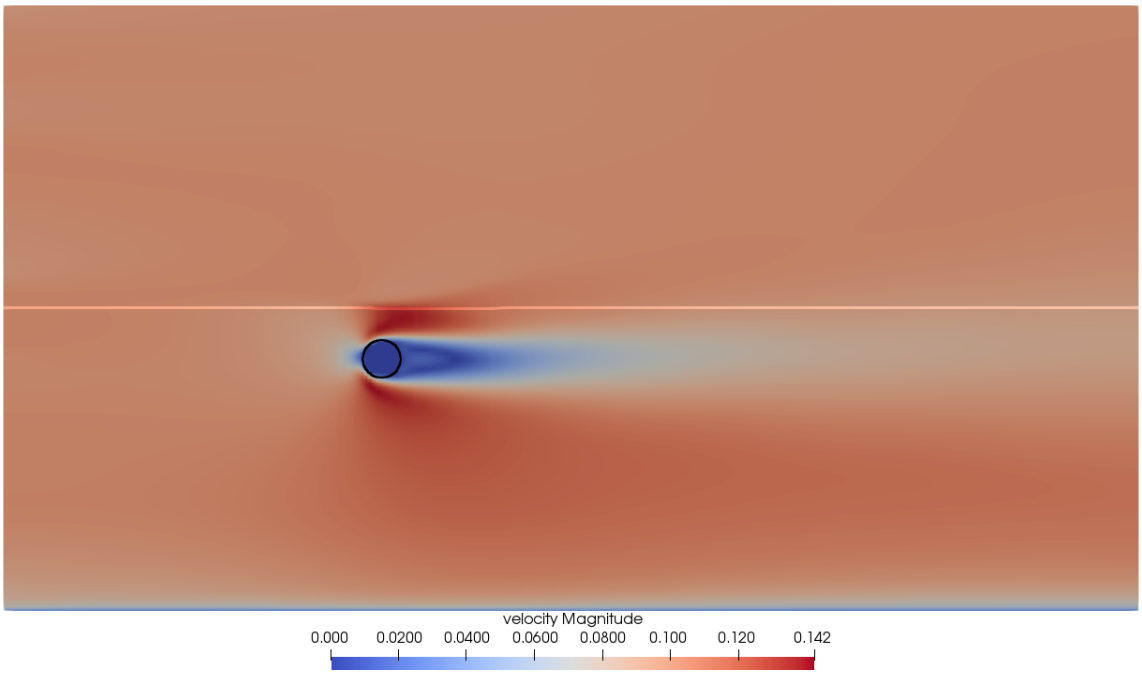

(d) t = 14 s

Figure 5.5: Velocity at different time instants. Development of steady state

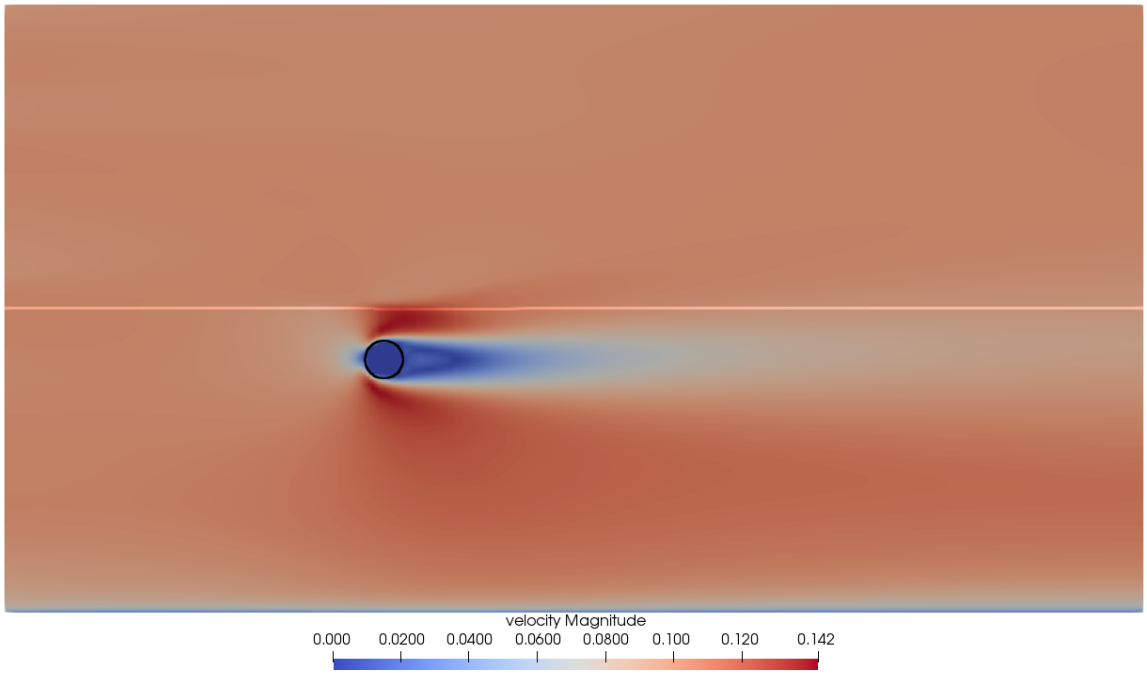

(e) t = 30 s

Figure 5.5: Velocity at different time instants. Development of steady state

Fig. 5.5a shows how zone of low velocities behind the cylinder is forming at t = 2 s, almost immediately after the beginning of the simulation. By the time simulation reaches time t = 6 s (Fig. 5.5b), the zone has enlarged, with its tail pointing slightly upwards. This slight distortion remains in place at time t = 10 s, depicted in Fig. 5.5c, while zone keeps growing. By the time simulation reaches instant of t = 14 s (Fig. 5.5d), the zone becomes strictly horizontal and its development stops: there is almost no visible difference between snapshots taken at t = 14 s and t = 30 s (Fig. 5.5e). Length of the zone of decreased velocity is approximately 0.8 m.

Cell size 2.5 mm

Fine grid with cell size of 2.5 mm is considered at last. Hydrostatic component of pressure is subtracted from the total distribution, thus, pressure due to current is obtained, which is presented in Fig. 5.6 As explained in subsection 5.1.1, total pressure is registered via number of probe points that are evenly distributed around the cylinder on a distance of one cell size from it (here 2.5 mm). Distribution of pressure due to current for this case is similar to those described above. After hydrostatic component of pressure had been removed, in top part and bottom part pressures became negligible. Conversely, in areas upstream and downstream of the cylinder, pressures are significant, which is associated with water deceleration in the regions. However, shape of distribution shown in Fig. 5.6 is slightly different from those in

Fig. 5.3 and 5.4. Pressure distribution for the model with cell size of 2.5 mm is almost as wide as one for the model with cell size of 5 mm, but the maximum value on the upstream side is approximately 12 Pa, which is similar in the model with 10 mm cell size. Same agreement is seen in downstream side pressures of models with 10 mm and 2.5 mm cell sizes: values of pressures for both cases are within 2 Pa behind the cylinder, whereas for model of 5 mm cell size pressures are registered at a level of 4 Pa.

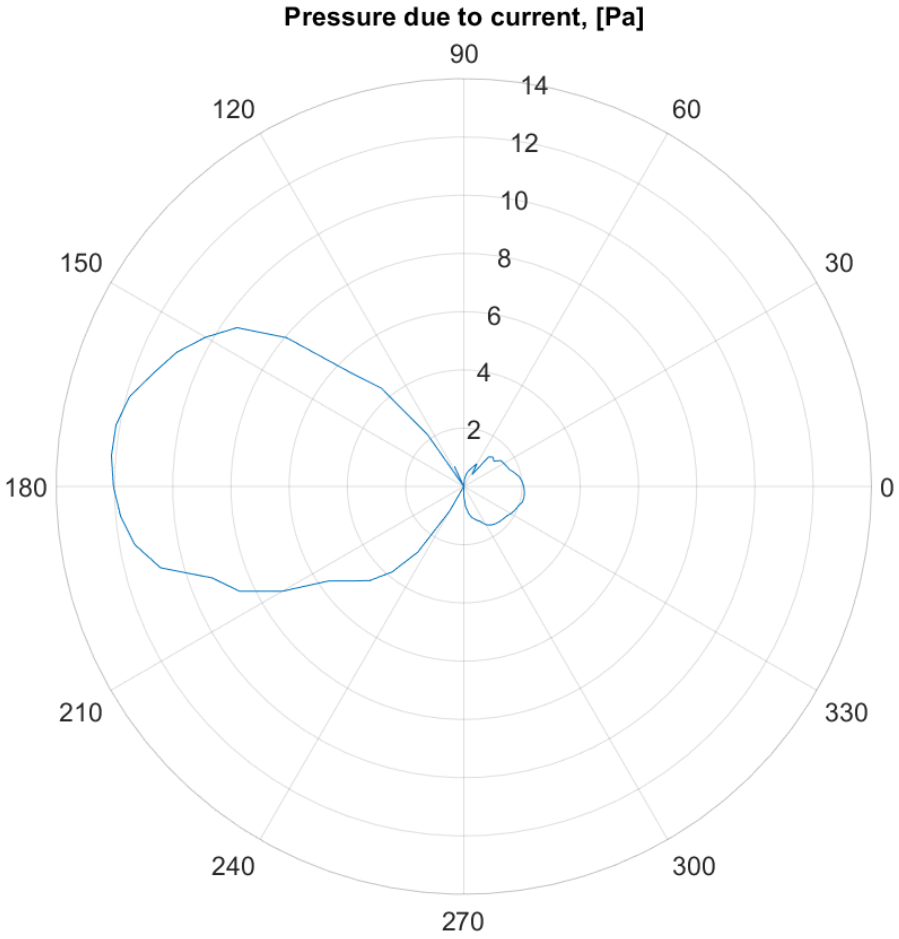

Figure 5.6: Pressure distribution for mesh size of 2.5 mm

For calculation of in-line force and drag coefficient full pressure distribution is used, as it is more precise. Hydrostatic component of pressure is cancelled out by itself as it acts on all sides. Numerical integration of pressure at probe points yields drag coefficient $C_D = 1.14$, which is lower compared to value obtained in physical experiments [27]: $C_D = 1.5$, and slightly lower than free-stream drag coefficient for $Re \simeq 5000$, which is $C_{D,fr.str} = 1.2$, according to Sarpkaya and Isaacson [28].

Function of force calculation within REEF3D yields drag coefficient $C_D = 1.17$, which slightly differs from drag coefficient computed via numerical integration of pressures and value estimated based upon Reynolds number.

Comparison of forces

Forces, obtained through installed function in REEF3D for models of different grid resolutions, are shown in Fig. 5.7. Significant variation in results is observed: $F_{inline} = 0.42$ N with corresponding drag coefficient $C_D = 1.69$ for model with cell size of 10 mm; $F_{inline} = 0.24$ N with $C_D = 0.98$ for model of 5 mm cell size and $F_{inline} = 0.29$ N with $C_D = 1.17$ for model with cell size of 2.5 mm.

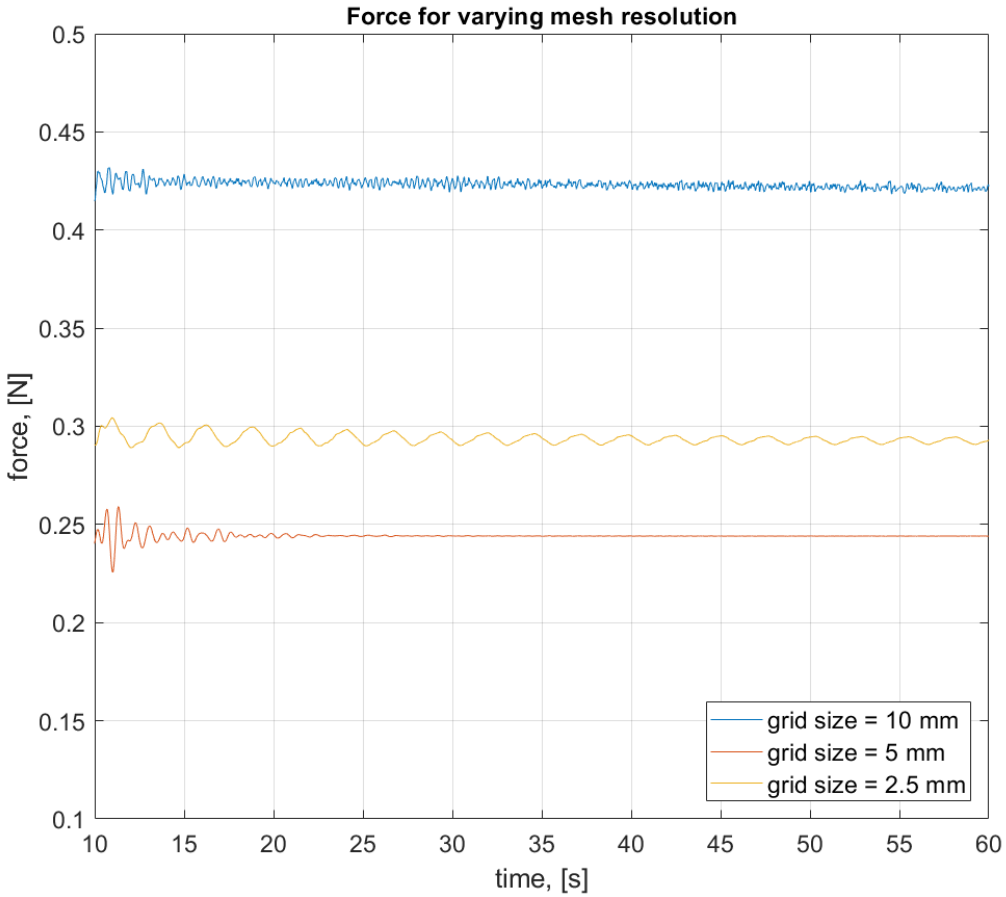

Figure 5.7: Influence of mesh size on drag force

As can be seen in Fig. 5.7, all the recorded forces demonstrate certain oscillations, which fade away for the case with cell size of 5 mm at time $t \simeq 25$, however, oscillations persist throughout entire simulation period for two other cases. Force fluctuation of

the model with very fine grid is periodic and becomes smoother as time advances. Vortex formation can be one of the reasons behind in-line force alteration, as Reynolds number for the model under consideration is within subcritical region ($Re \simeq 5000$), which implies fully turbulent vortex street behind the cylinder. It is highly likely that models with coarser mesh are not able to grasp vortex formation, therefore fluctuation is not observed. However, force behaviour, registered in the model with the coarsest mesh, contains numerous spikes of small amplitude, which can be explained by low accuracy of such model. Same reason most likely stands behind the fact that drag coefficient is much higher than anticipated.

Grid convergence study is summarized in Table 5.1. Notation is used as follows:

- $C_{d,1}$ - drag coefficient computed via numerical integration of pressures around the cylinder;
- $C_{d,2}$ - drag coefficient computed via function installed in REEF3D;
- $C_{d,0}$ - expected drag coefficient corresponding to $Re \simeq 5000$.

Table 5.1: Drag coefficients obtained by different methods for varying mesh size

Cell size, [mm]	$C_{d,1}$	$C_{d,2}$	$C_{d,0}$
10	1.41	1.69	1.2
5	1.25	0.98	1.2
2.5	1.14	1.17	1.2

It is clear that model with the finest mesh yields the most accurate result, however, it is very computationally demanding. This issue will be addressed below.

5.1.3 Varying CFL criterion

In order to increase computational efficiency, different values of CFL criterion, which links cell size Δx and time step Δt and imposes limits on them, are tried. Namely:

- $CFL = 0.2$
- $CFL = 0.3$
- $CFL = 0.5$

The larger the CFL criterion, the bigger time steps are taken, thus, it increases computational efficiency at cost of accuracy. Extent of this influence in investigated below.

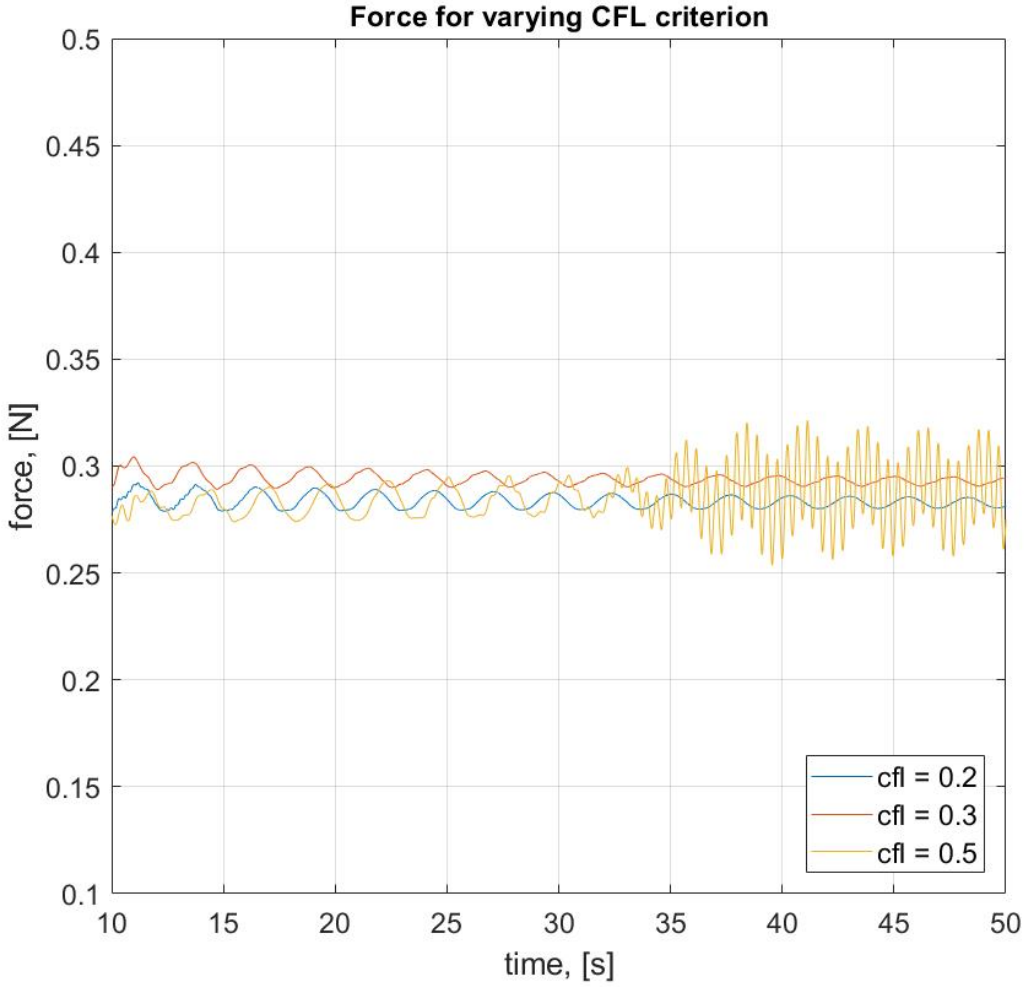

Figure 5.8: Influence of CFL criterion on drag force

As can be seen in Fig. 5.8, mean values of in-line forces in general are in agreement, albeit drag force in model with $CFL = 0.3$ is slightly bigger than that of the model with $CFL = 0.2$: it is $F = 0.28$ and $F = 0.28$, respectively (difference of 3%). Force of the model with $CFL = 0.5$ exhibit different behaviour: instability develops at $t \simeq 33$ s, meaning that larger values of CFL criterion cannot be used. It is decided that in given conditions it is optimal to perform simulations with $CFL = 0.3$.

5.1.4 Submerged floating tube in two-dimensional case

Another possible solution for increasing efficiency is downsizing computational domain. So far simulations are performed in three-dimensional numerical tank with width $b_T = 0.5$. Reducing the width would lead to significant improvement of effi-

ciency, however, it might also cause instabilities. This measure is tried in the numerical tank which width is reduced to $b_T = 0.1$ m, thus making the simulation essentially two-dimensional. Length of the tank and depth of water, as well as cylinder diameter, remained unchanged. Results are summarized in Fig. 5.9

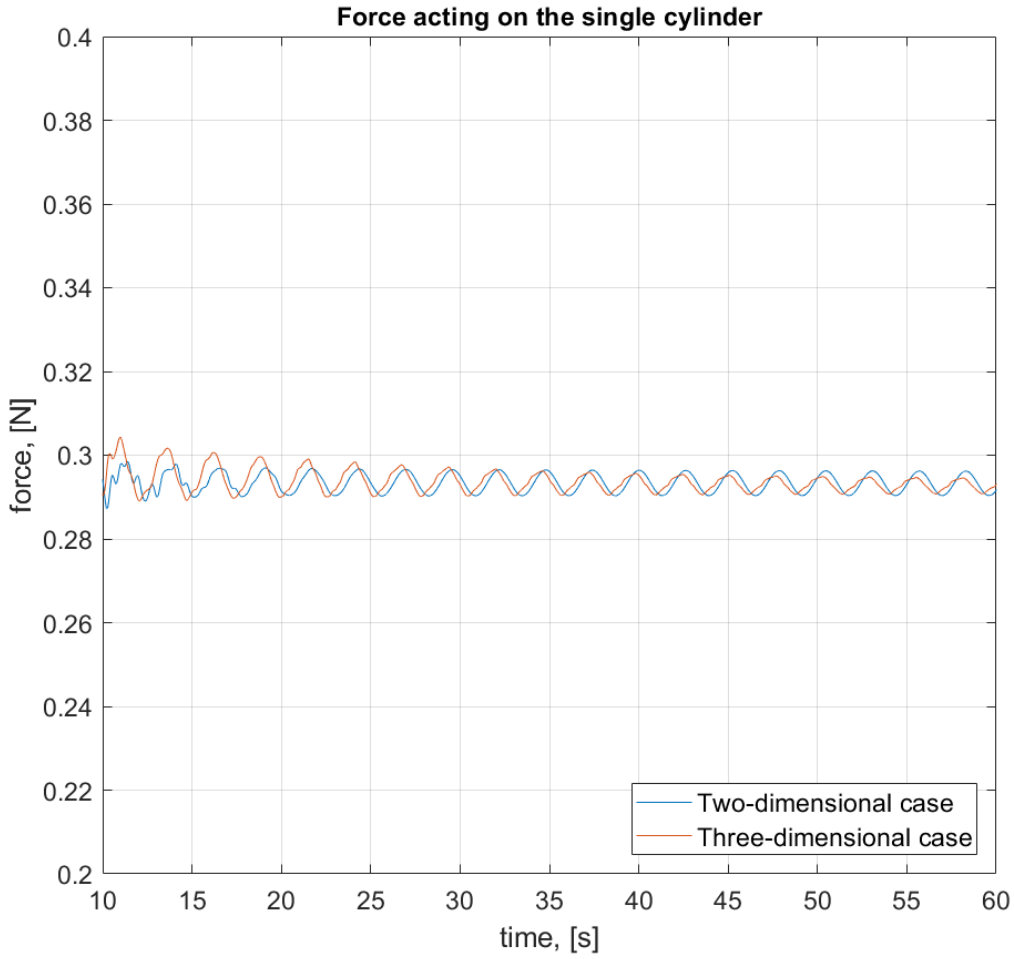

Figure 5.9: Comparison of drag forces obtained in two- and three-dimensional simulations

As can be seen in Fig. 5.9, in-line force behaviour in both models is very similar with some negligible discrepancies, namely, oscillations of the force in two-dimensional model smoothen out faster in the beginning of the simulation than those in three-dimensional model. Towards the end of the simulation, however, amplitude of oscillations in force of three-dimensional model is smaller than in two-dimensional case. Nevertheless, good agreement between forces allows to use two-dimensional models, which considerably improves computational efficiency.

5.1.5 Two cylinders in homogeneous water

After it was established that two-dimensional model is sufficient, additional cylinder is introduced so as to investigate its influence on in-line forces appearing in the system. Scheme of the numerical tank is shown in Fig. 5.10. Two cylinders are placed in a row, separated by some distance d, at the same level of submergence.

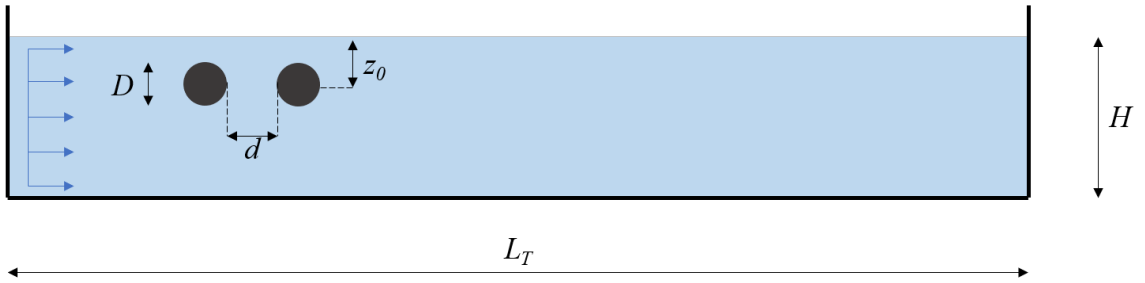

Figure 5.10: Combination of the cylinders

Three values of distance d are tested (D stands for diameter of the cylinder):

- $d = 1D$
- $d = 1.5D$
- $d = 2D$

Influence of the size of the distance on drag force is investigated in following subsections.

Distance between cylinders of 1D

At first, impact of $d = 1D$ is tested. Fig. 5.11 shows velocity profile at the time instant t = 15 s, when steady state is fully developed.

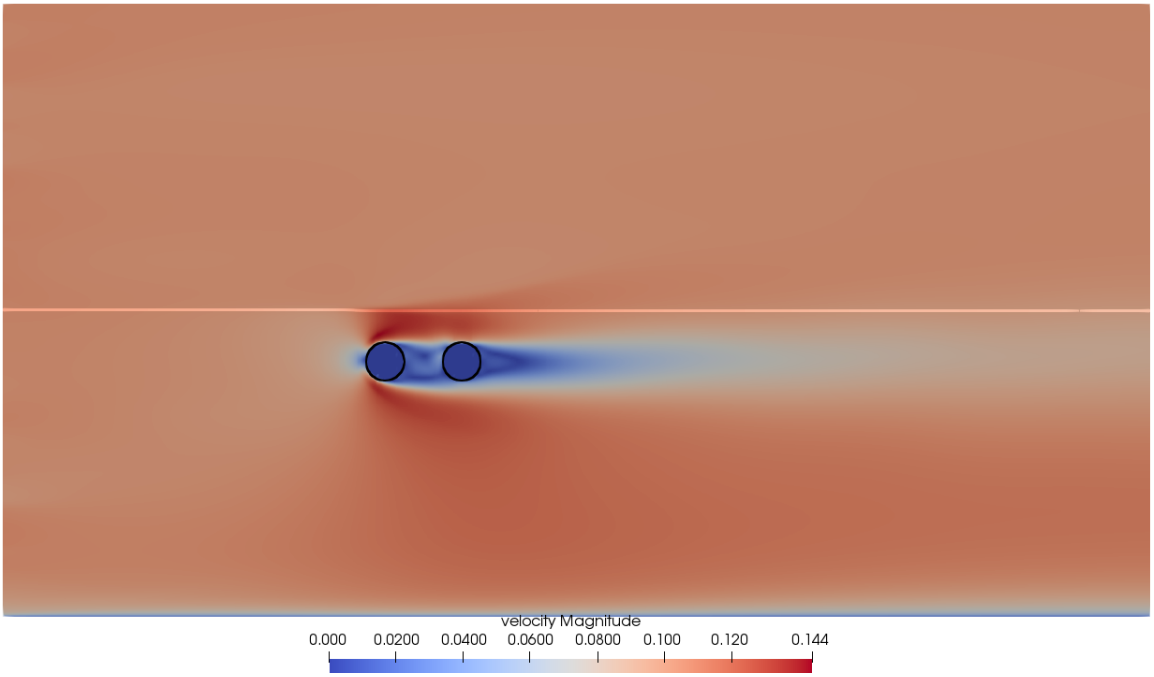

Figure 5.11: Two cylinders: velocity at t = 15 s

Fig. 5.12 represents distribution of pressure due to current for the first cylinder (Fig. 5.12a) and for the second cylinder (Fig. 5.12b). These distributions are obtained by subtracting hydrostatic component from total pressure. [25]

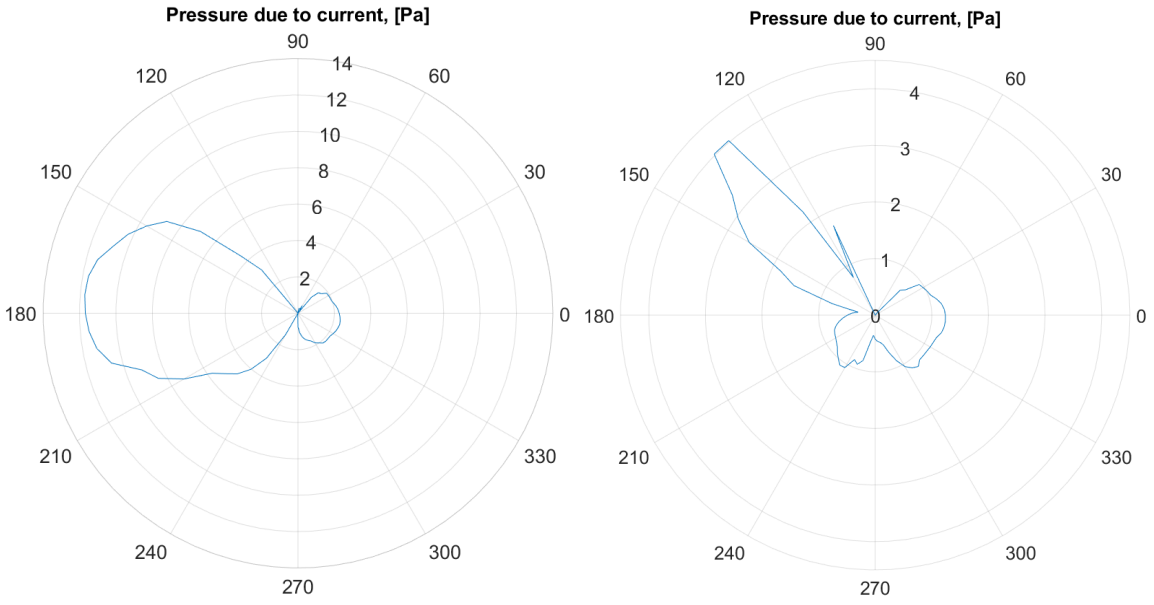

(a) Cylinder 1

(b) Cylinder 2

Figure 5.12: Pressure distribution for cylinders with distance of 1D between them

It can be seen clearly that distribution of pressure for the first cylinder in the set (Fig. 5.12a) is similar in shape and values to distribution of pressure for the single cylinder (Fig. 5.6). Distribution of pressure due to current for the second cylinder, however, is different: pressures of values up to 4 Pa are registered in the sector [120,150] *deg*. It is the same sector where deceleration is observed in Fig. 5.11. Similar effect is observed in front lower part of the second cylinder, albeit registered pressure is much smaller and does not go beyond 1 Pa. Horizontal asymmetry can be partly explained by proximity effects due to presence of free surface. Pressures behind the second cylinder are also smaller than those behind the first cylinder, however, the shape of the distribution in this part is similar.

Distance between cylinders of 1.5D

As a next step, distance between two cylinders is enlarged to $1.5D$. In Fig. 5.13 stages of steady state development are shown by means of snapshots of velocity profiles at different time instants. Process of steady state development is identical for all models with two cylinders, therefore it is omitted for cases with $d = 1D$ and $d = 2D$.

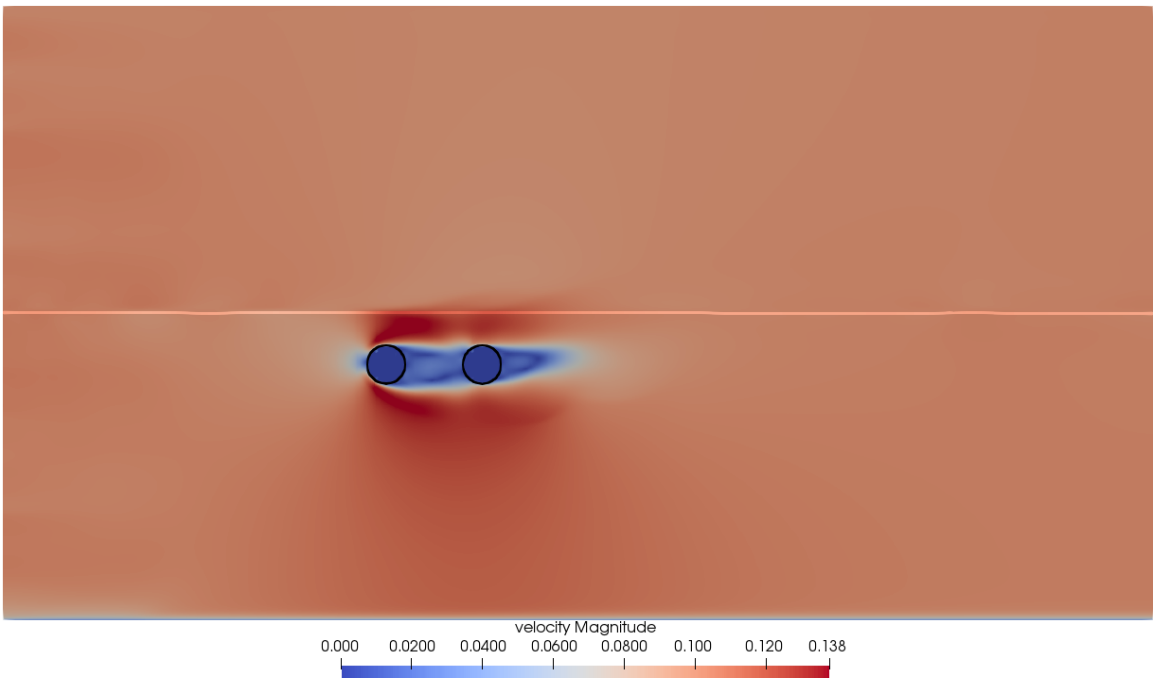

(a) t = 2 s

Figure 5.13: Two cylinders: velocity at different time instants. Development of steady state

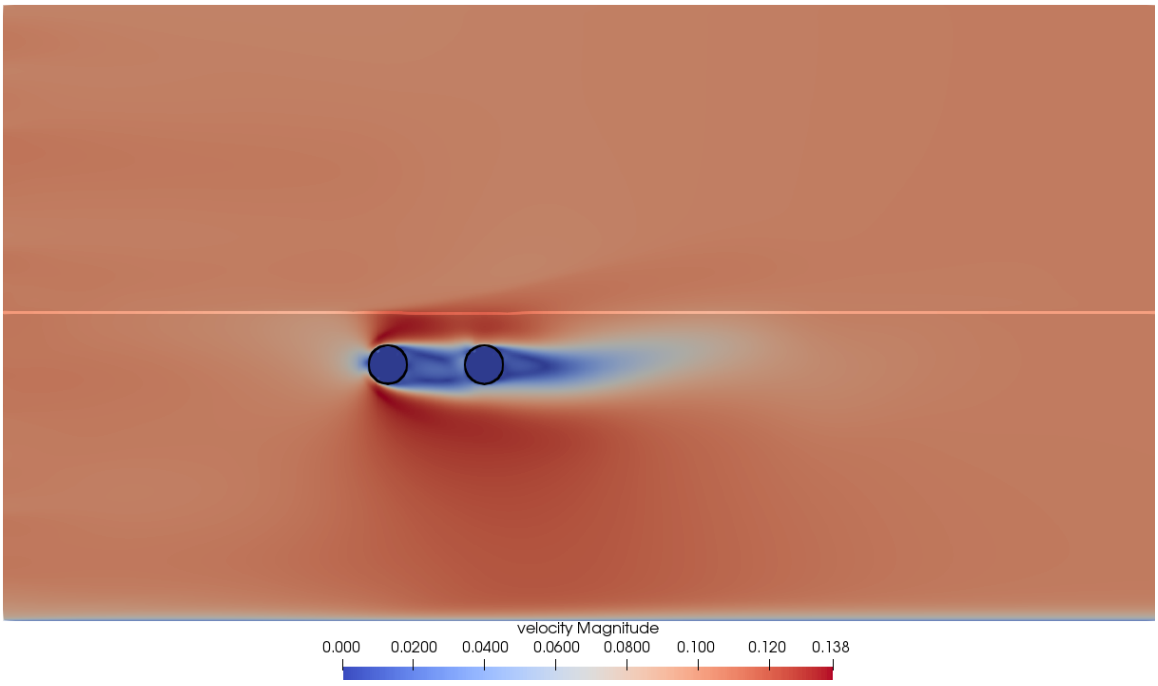

(b) t = 5 s

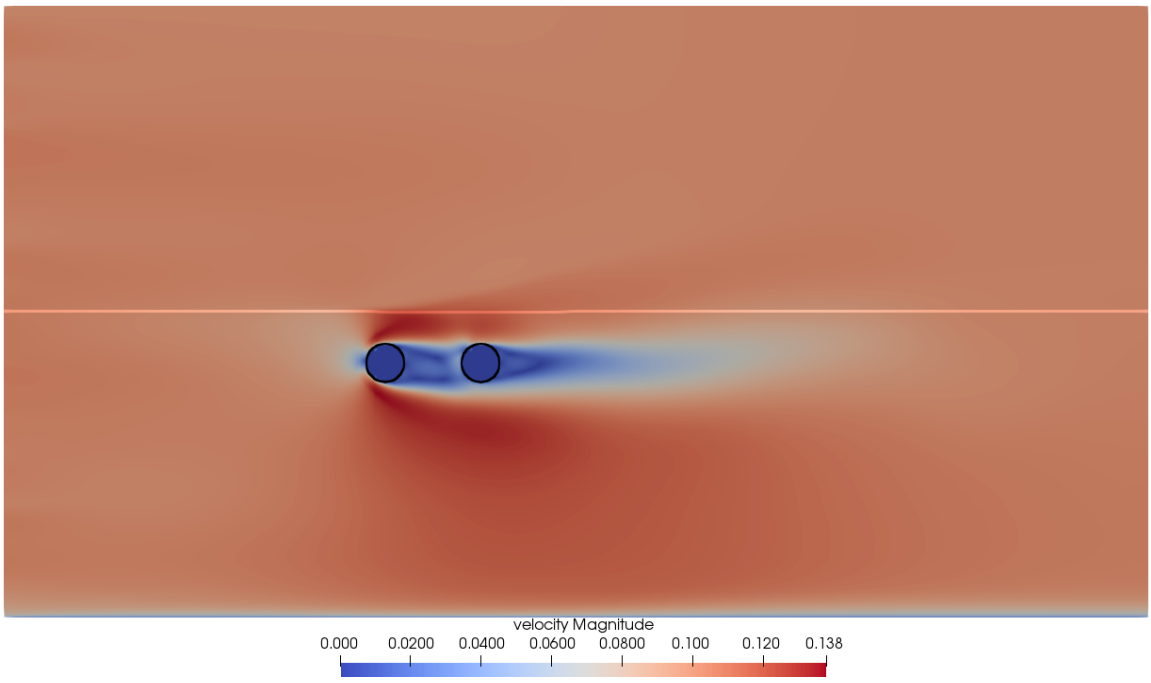

(c) t = 7 s

Figure 5.13: Two cylinders: velocity at different time instants. Development of steady state

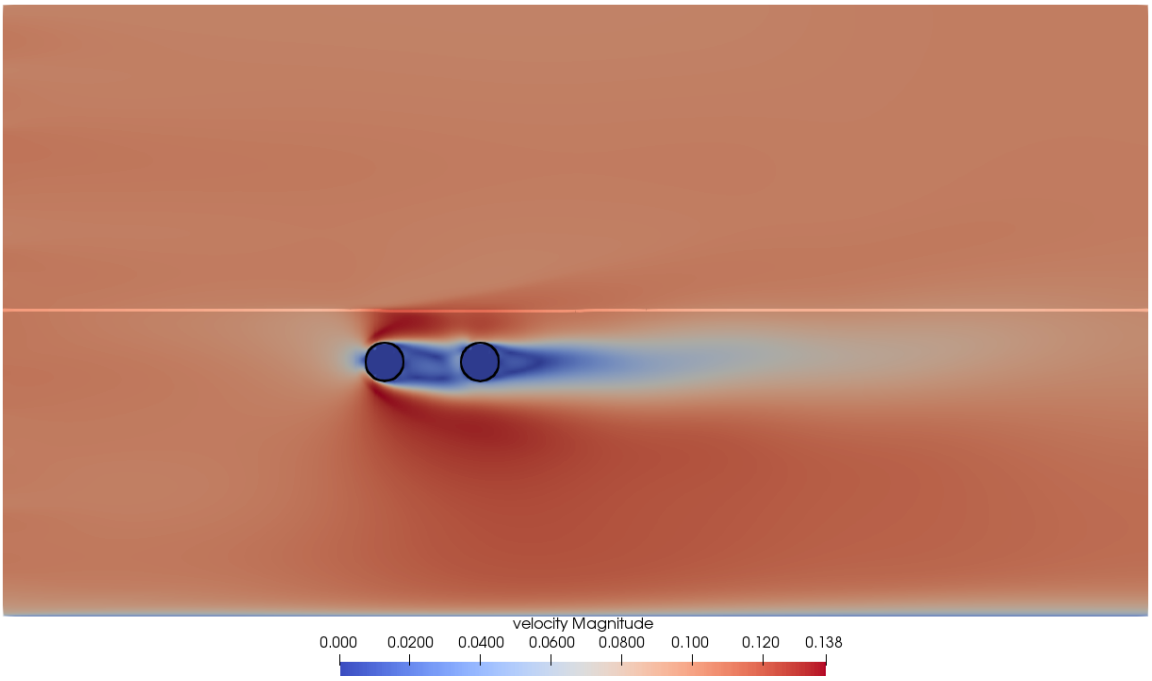

(d) t = 10 s

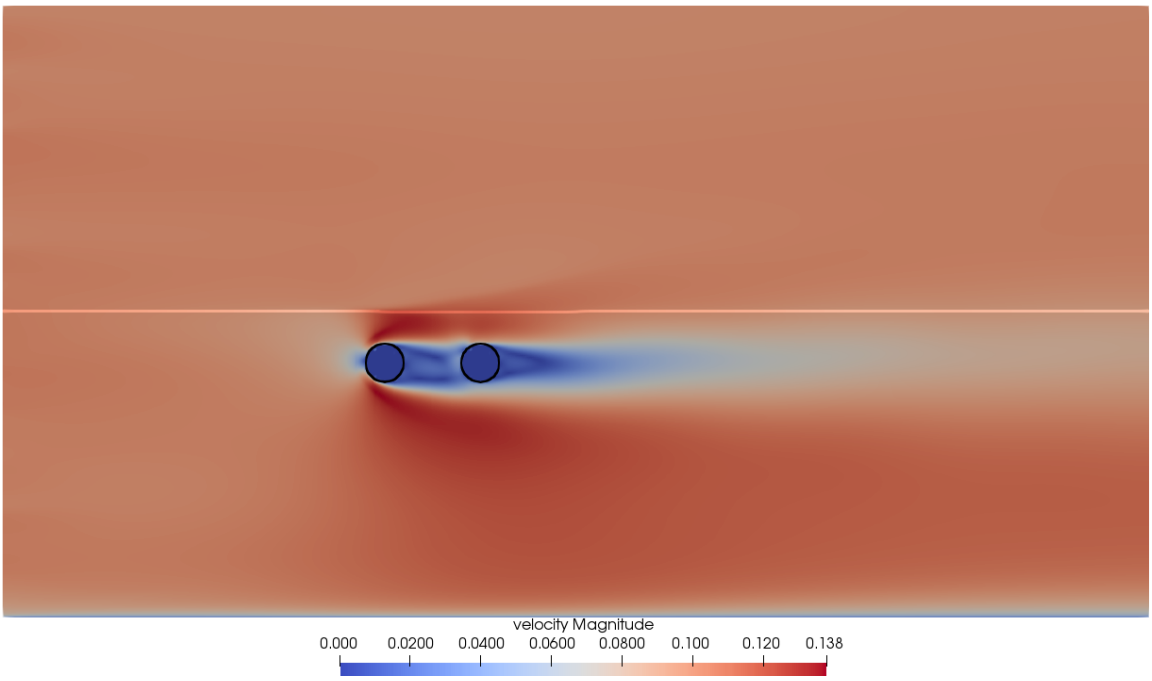

(e) t = 15 s

Figure 5.13: Two cylinders: velocity at different time instants. Development of steady state

At the beginning of the simulation, at time t = 2 s (Fig. 5.13a), zones of decreased

velocity started developing behind the cylinder. The gap between accelerated zones of the cylinders is present due to the fact that cylinders experienced start of the flow independently. The gap disappears as simulation reaches time t = 5 s (Fig. 5.13b). Decreased velocity zone behind the second cylinder grows and slightly bends upwards at time t = 5 s, as well as at time t = 7 s (Fig. 5.13c). Zone of decreased velocity grows in length until time t = 15 s (Fig. 5.13e), where it stabilizes, reaching the length of approximately 0.8 m.

Distribution of pressure for the first cylinder in the set (Fig. 5.14a) is similar in shape and values to distribution of pressure for the single cylinder (Fig. 5.6). Distribution of pressure due to current for the second cylinder, however, is different: pressures of values up to 4 Pa are registered in the sector [120:150] *deg*. It is the same sector where deceleration is observed in Fig. 5.13. Similar effect is observed in front lower part of the second cylinder, albeit registered pressure is much smaller, approximately 1 Pa. Horizontal asymmetry can be partly explained by proximity effects due to presence of free surface. Pressures behind the second cylinder are also smaller than those behind the first cylinder, however, the shape of the distribution in this part is similar.

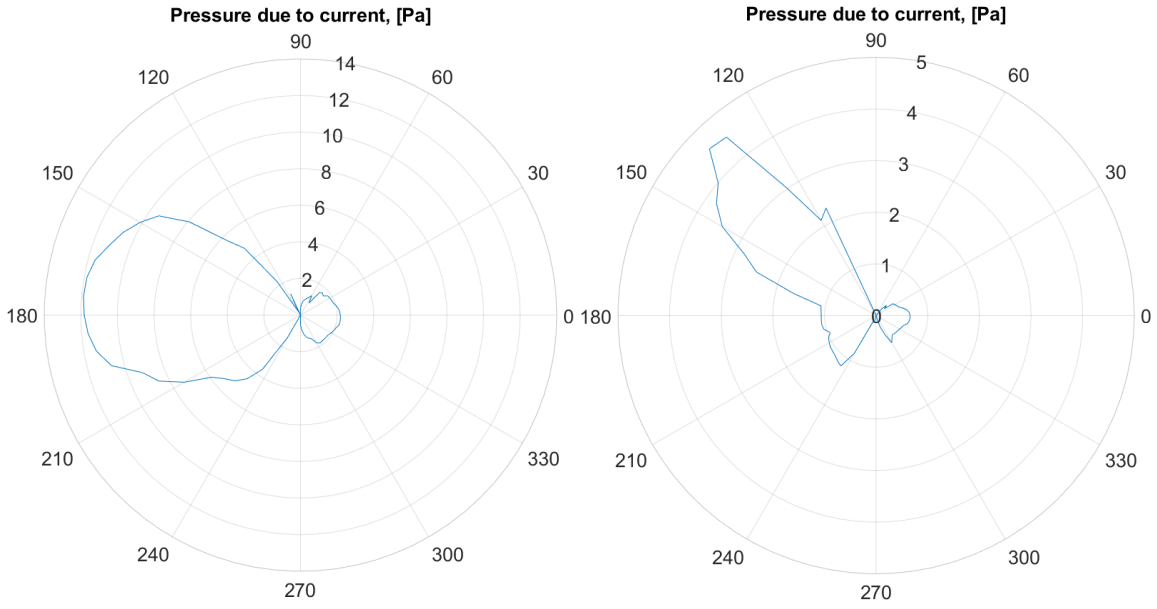

(f) Cylinder 1 (g) Cylinder 2

Figure 5.14: Pressure distribution for cylinders with distance of 1.5D between them

Compared to pressure distribution for the second cylinder in the case with $d = 1D$ (Fig. 5.12b), distribution depicted in Fig. 5.14b demonstrates higher pressures in front part of the cylinder. In particular, pressure registered on horizontal diameter is non-zero, which stems from more complicated flow pattern due to increased distance

between the cylinders. Pressures in rear part of the second cylinder in the case under consideration are smaller than those in case with $d = 1D$.

Distance between cylinders of 2D

Lastly, distance between the cylinders is set to $d = 2D$. Velocity profile at time instant t = 15 s, in developed steady state, is shown in Fig. 5.15.

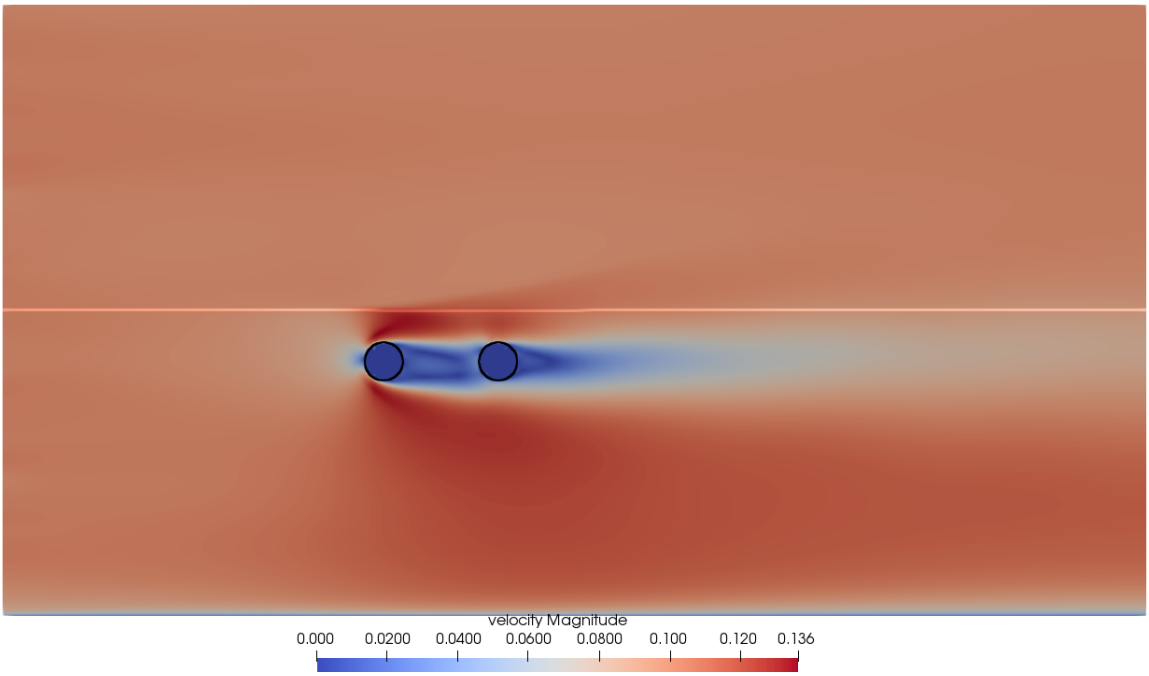

Figure 5.15: Two cylinders: velocity at t = 15 s

Distribution of pressure for the first cylinder in the set (Fig. 5.16a) is similar in shape and values to distribution of pressure for the single cylinder (Fig. 5.6). Distribution of pressure due to current for the second cylinder, however, is different: pressures of values up to 4 Pa are registered in front of the cylinder, with highest values in sector [120,150] *deg* (up to 4 Pa). It is the same sector where deceleration is observed in Fig. 5.15. Similar effect is observed in front lower part of the second cylinder, albeit registered pressure is much smaller, approximately 1.6 Pa. Horizontal asymmetry can be partly explained by proximity effects due to presence of free surface. Pressures behind the second cylinder are also smaller than those behind the first cylinder, however, the shape of the distribution in this part is similar.

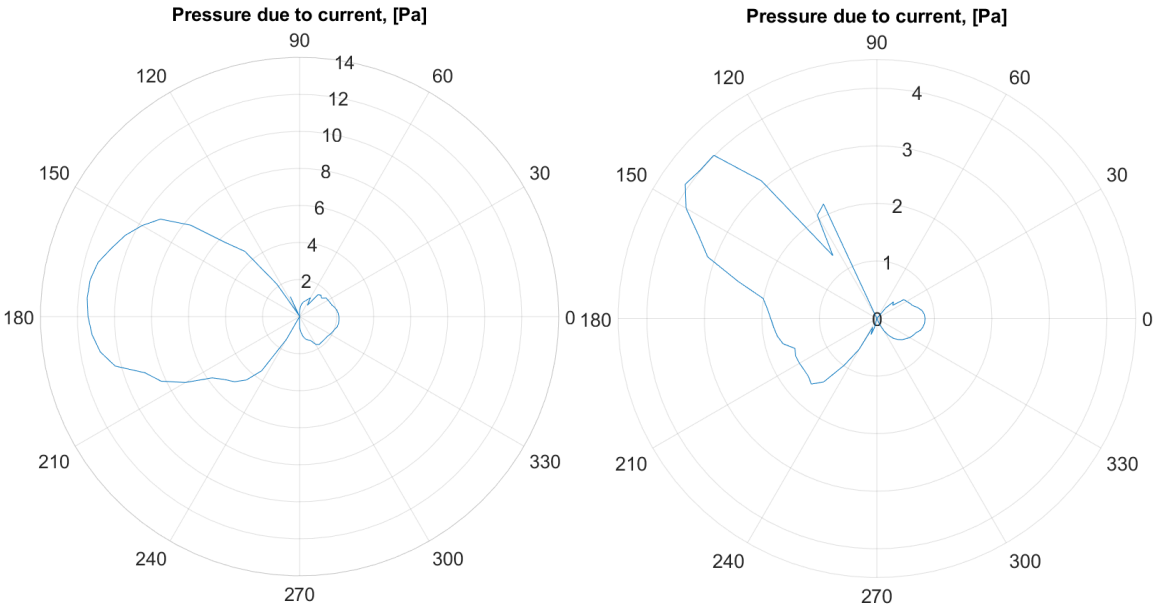

(a) Cylinder 1

(b) Cylinder 2

Figure 5.16: Pressure distribution for cylinders with distance of 2D between them

Compared to pressure distributions for two previous cases, distribution shown in Fig. 5.16b) has the biggest pressures in the front part. In particular, pressure registered on horizontal diameter is non-zero (approximately 2 Pa), which stems from more complicated flow pattern due to increased distance between the cylinders. Pressures in rear part of the second cylinder in the case under consideration are bigger that those in case with $d = 1.5D$.

Comparison of forces acting upon cylinders

In this part, in-line forces acting on two cylinders are compared. As can be seen in Fig. 5.17, in case when only one cylinder is placed in the flow, it experiences the highest drag force ($F = 0.293$ N). Moreover, presence of the second cylinder behind the first one, at the same level of submergence, hampers formation of vortices, therefore no fluctuation in drag force is observed for all cases with two cylinders.

In Table 5.2 values of registered forces are shown. The smallest drag force is registered in case with $d = 1D$: it is 6% smaller than drag force acting on single cylinder. It has to do with influence that second cylinder imposes on flow behaviour behind the first cylinder. It was anticipated that growing distance would have unambivalent impact on the in-line forces, which is, however, not the case: registered in-line forces for cases with $d = 1D$ and $d = 2D$ are both smaller than that for the case with $d = 1.5D$. This can be explained by the fact that behaviour of flow patterns in between the cylinders

is very subtle. In addition, difference in forces of 6% is arguably negligible.

Table 5.2: Drag force acting on the first cylinder in combination

d	$F_{in-line}$, $[N]$
Single cylinder	0.293
1D	0.275
1.5D	0.288
2D	0.279

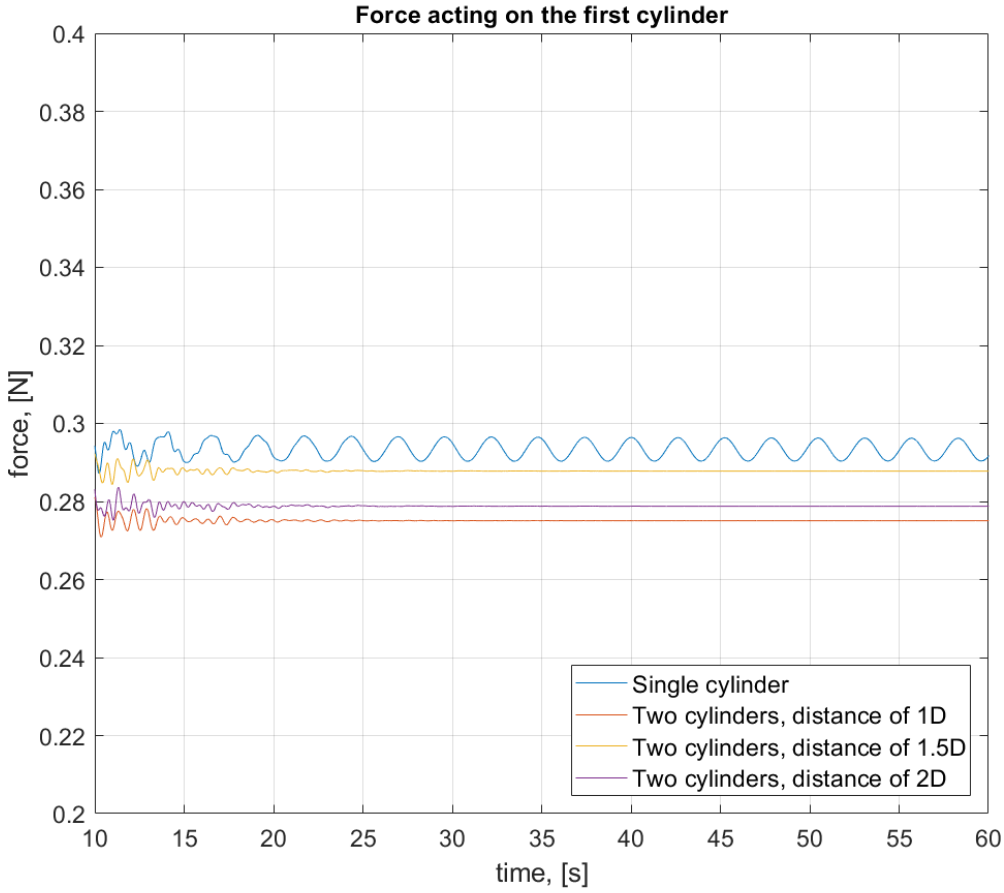

Figure 5.17: Drag forces acting on the first cylinder in the combination

As expected, presence of the first cylinder considerably influences in-line force acting on the second cylinder (Fig. 5.18). Moreover, nature of this influence is unambivalent: the bigger the distence, the larger in-line force registered for the second cylinder becomes, which is brought about by the fact that protection effect of the first cylinder

decreases with growing distance. No fluctuation in drag force is observed, which can be explained by the fact that the flow velocity in front of the second cylinder is not sufficient to induce vortex formation.

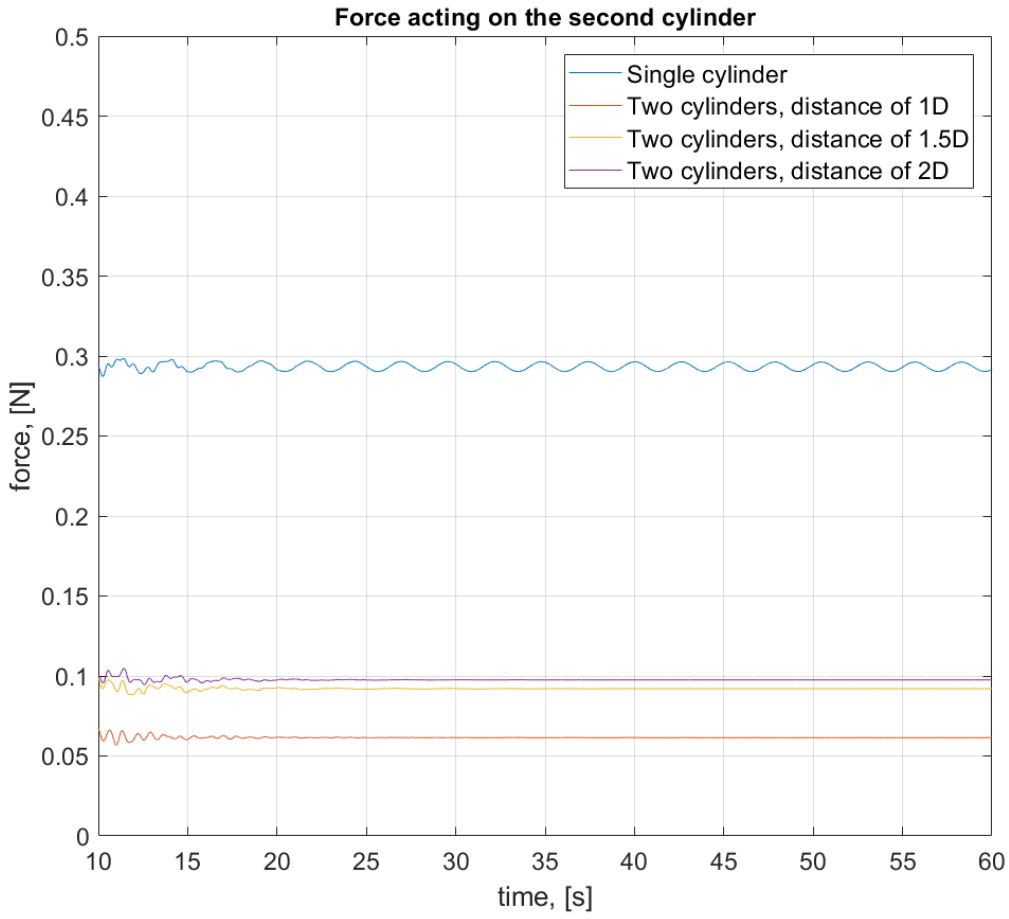

Figure 5.18: Drag forces acting on the second cylinder in the combination

Registered in-line forces for the second cylinder remain below 0.1 N in all considered cases, which is approximately 3 times smaller than force registered in case with single cylinder. Difference in forces for cases with $d = 1D$ and $d = 1.5D$ is larger than difference in forces for cases $d = 1.5D$ and $d = 2D$, which suggests that dependence between in-line forces acting on the second cylinder and distance d is non-linear.

Table 5.3: Drag force acting on the second cylinder in combination

d	$F_{in-line}$, $[N]$
Single cylinder	0.293
1D	0.061
1.5D	0.092
2D	0.098

5.2 SFT in stratified water

After numerical model of horizontal cylinder in flow of homogeneous water was validated, stratification is introduced. Density of bottom layer is chosen according to ration $\Delta\rho/\rho_1 = 0.031$ from table 3.2, which yields $\rho_1 = 1035\ kg/m^3$. Test is performed in three-dimensional numerical tank with cell size of 5 mm. Simulating stratified flow over cylinder in two-dimensional numerical tank brought about enhanced mixing, leading to results that cannot be read and interpreted. In order to keep computational efficiency at an acceptable level, coarse grid is employed.

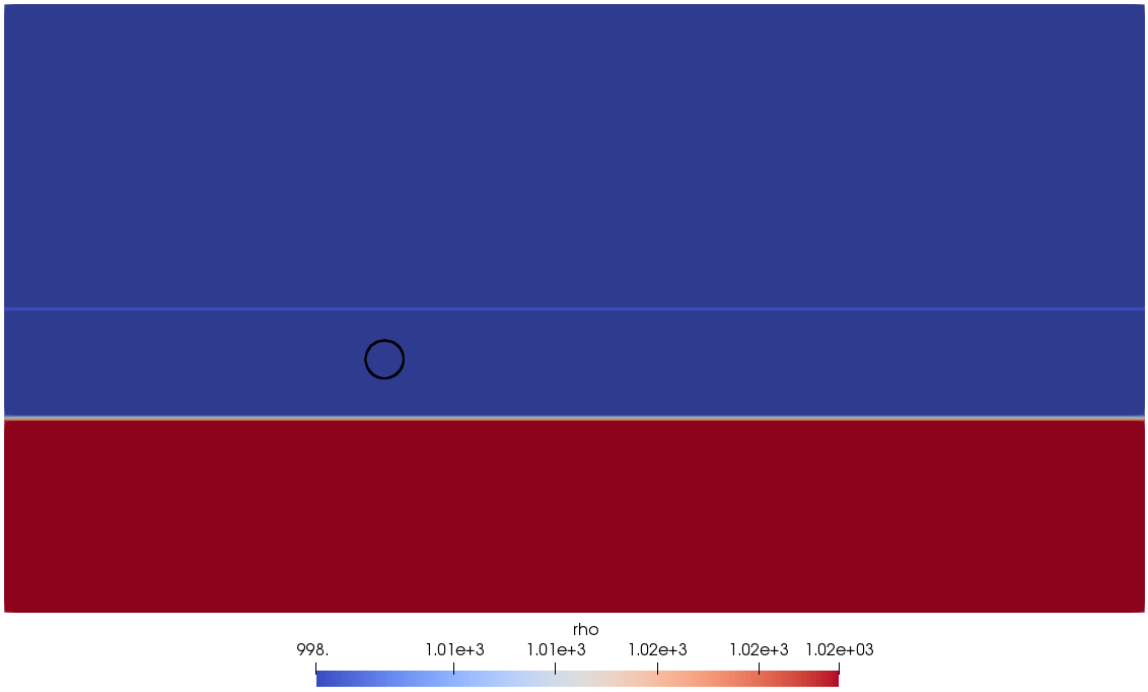

(a) t = 0 s

Figure 5.19: Cylinder in stratified fluid

Thickness of bottom layer is set to $h = 255$ mm, thus thickness of layer of fresh water is $h' = 145$ mm (total water depth is 0.4 m). Light-blue line in Fig. 5.18 represents

free surface. Below the free surface blue area of fresh water is placed, and under fresh water - salt water, represented by red color.

At the beginning of the simulation (Fig. 5.18a), water is at rest. Once simulation has started, mixing of two layers begins (Fig. 5.18b). At the bottom of the snapshot fresh water "leak" is visible, which is an artifact that disappears as time advances (Fig. 5.18c). At time instant t = 5 s, disturbance of particles from the layer of their neutral buoyancy is clear, as well as work of buoyancy restoration forces, which create pattern resembling the wave downstream of the cylinder. At time instant t = 10 s (Fig. 5.18d) obscure curved line, which separates less mixed water from more mixed water upstream of the cylinder, is another artifact. It also disappears by the time simulation reaches t = 15 s (Fig. 5.18e). Wave downstream of the cylinder remains in place until the end of the simulation at t = 30 s (Fig. 5.18f), when the steady state has developed. It is not possible to register the length of the wave as tank appeared to be too short. It is not possible to establish longer tank due to restrictions of computational demand.

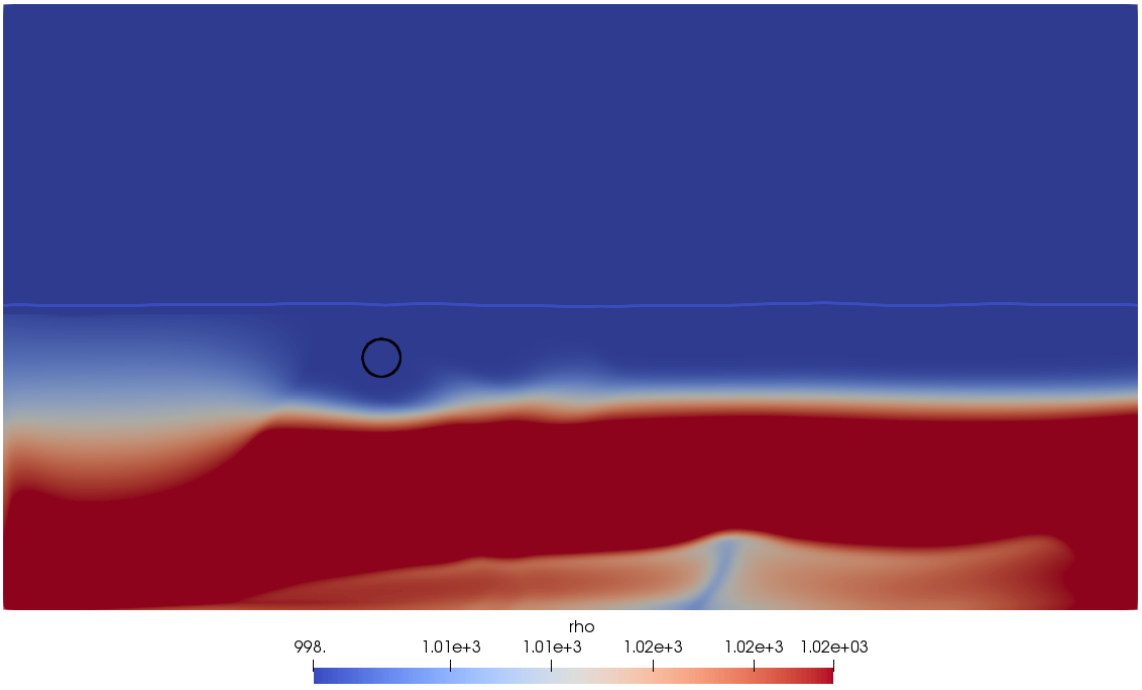

(b) t = 2 s

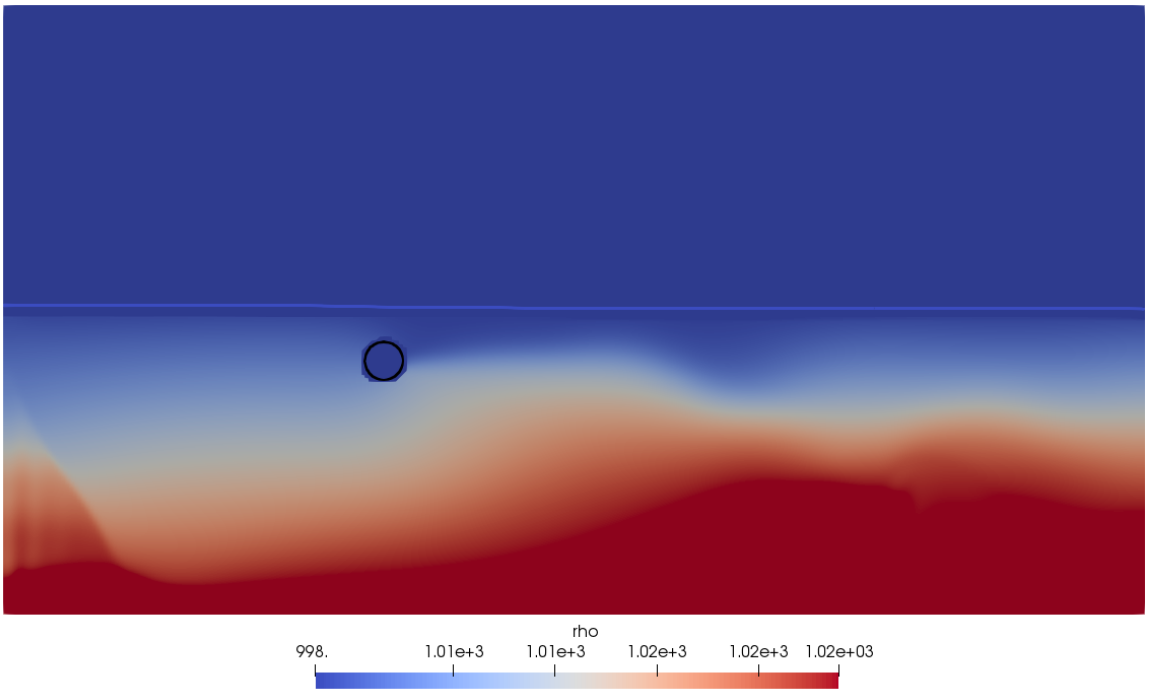

(c) t = 5 s

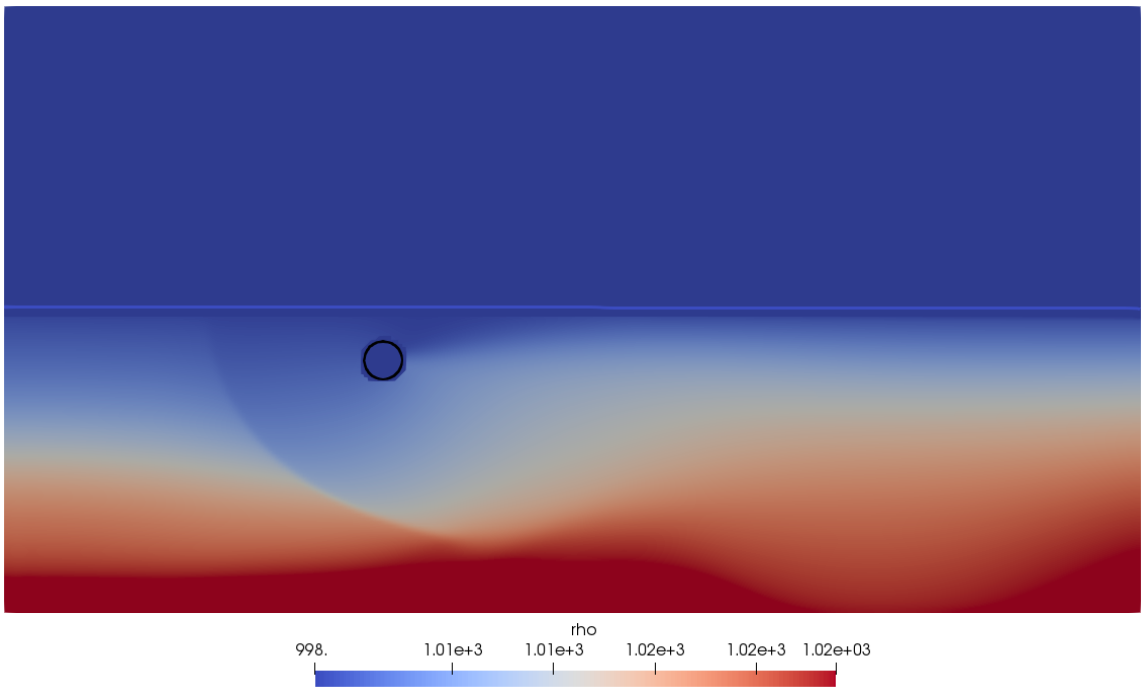

(d) t = 10 s

Figure 5.18: Cylinder in stratified fluid

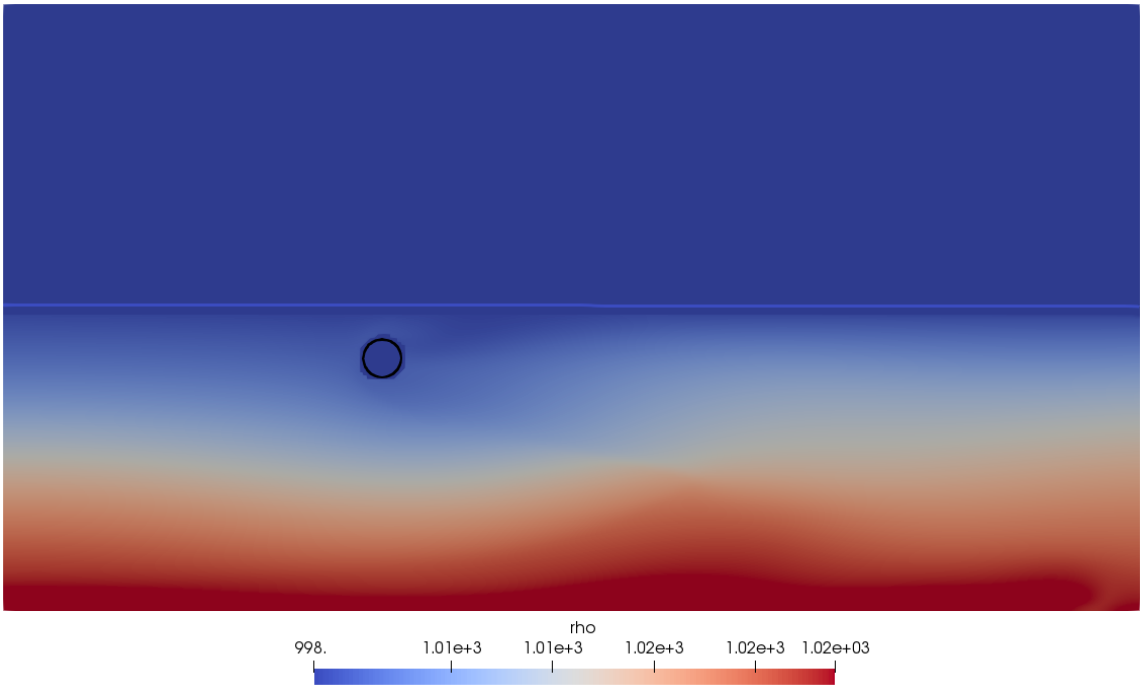

(e) t = 15 s

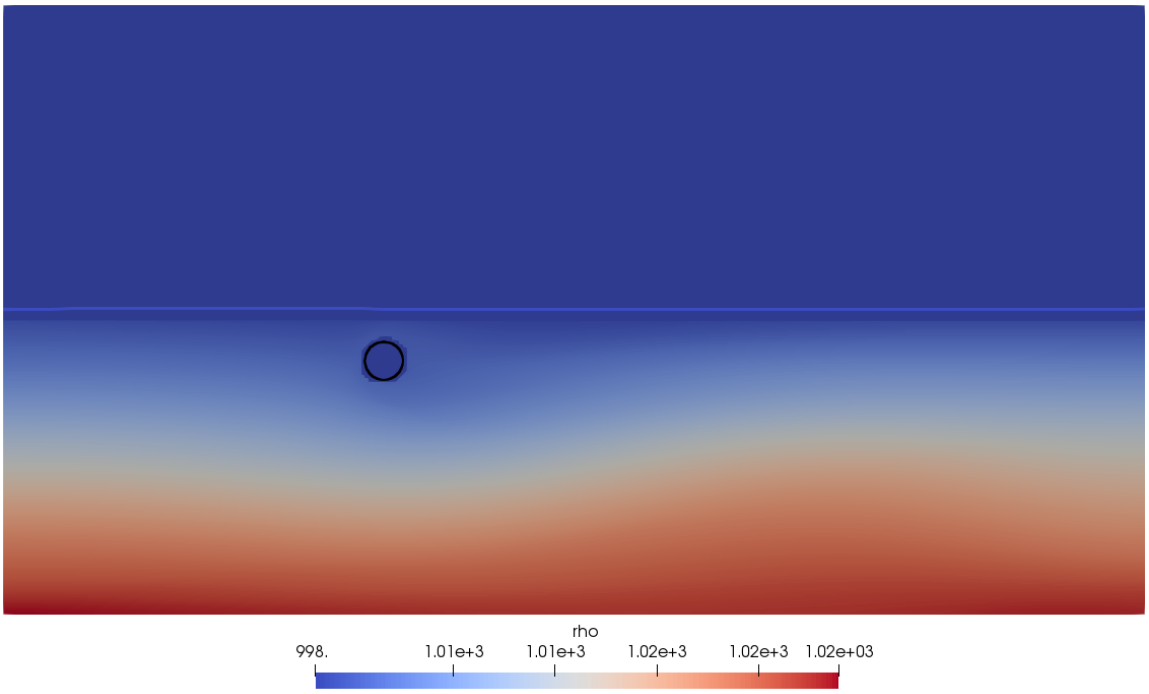

(f) t = 30 s

Figure 5.18: Cylinder in stratified fluid

It is possible to register wave height H of the internal wave (Fig. 5.19). As depicted

in the figure, wave height $H \simeq 0.07$ m, which yields $H/D = 1.4$. According to formula (eq. 3.13), celerity of the longest internal wave for given parameters is $c_i = 0.167$, meaning that densimetric Froude number (eq. 3.12) takes value $Fr_d = 0.6$. Combination of $Fr_d = 0.6$ and registered $H/D = 1.4$ falls within data range obtained by Arntsen in [27].

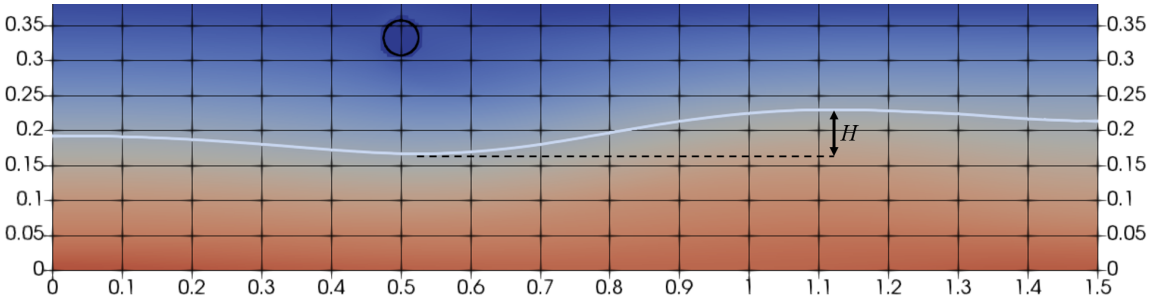

Figure 5.19: Wave height of the internal wave

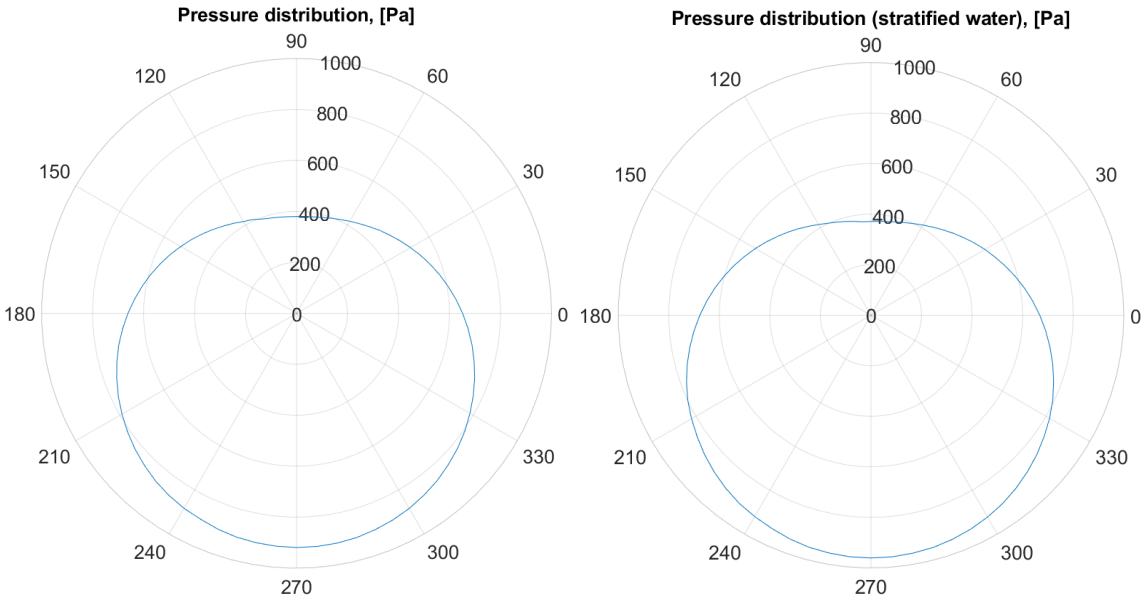

(a) Homogeneous flow

(b) Stratified flow

Figure 5.20: Pressure distributions around cylinder in homogeneous and stratified flows

In order to estimate in-line force acting upon the cylinder, numerical integration of the pressure needs to be performed, as installed function in REEF3D does not produce accurate results for used grid size, which was established in section 5.1.2. Full pressure distribution around the cylinder in stratified flow is compared to that of cylinder in

homogeneous flow in Fig. 5.20. It is not possible to subtract hydrostatic component as it depends on water density ρ, which is not constant in case with stratified water. However, difference in distributions still can be observed: for the case in question, pressure is larger in the area underneath the cylinder, where it takes value of 960 Pa, compared to 919 Pa in case with homogeneous water.

Numerical integration of full pressure around the cylinder in stratified flow resulted in $F_{in-line} = 0.277$ N, which is less than $F_{in-line} = 0.286$ N for case with homogeneous water. Anticipated value of force for conditions under consideration, found by Arntsen [27], is $F_{in-line} \simeq 0.45$, therefore, no agreement in horizontal forces between physical experiments and numerical simulation performed in this study is observed at this point. Inaccuracy, brought about by the fact that the grid is too coarse, can be a possible explanation, as well as insufficient simulation time. However, both simulation time and grid size are chosen based on computational efficiency considerations. Improving either of the parameters would lead to simulation time that lies beyond reasonable limits.

Chapter 6

Conclusions and Outlook

6.1 Propagation of the gravity current

6.1.1 Conclusions

This study was aimed at determining optimal modelling parameters for simulation of the gravity current in two- and three-dimensional setup, as it contributes to successful modelling of internal waves. At first, REEF3D modelling capabilities were introduced, as well as concepts of computational fluid dynamics. After that, brief outline of physical experiments on the gravity current development were presented, based on which numerical models were set up. At first, two-dimensional gravity current was considered, where two sets of simulations were performed: one with Large-Eddy Simulation modelling of turbulence, and another one with no turbulence modelling. For the two aforementioned sets grid convergence study was performed, which resulted in conclusion that, in terms of propagation speed, fine mesh with the cell sizes of 5 and 2.5 mm are the most accurate in case when LES modelling of turbulence is employed, albeit some mismatch between physical experiments and numerical simulations was observed. For the case where turbulence eddies were resolved directly, all mesh sizes demonstrated arguably good agreement with results of physical experiments, however, fine mesh produced the most accurate propagation speed. Moreover, based upon obtained results, coarse mesh is believed to enhance mixing for both sets of simulations. Therefore, it is concluded that for two-dimensional simulations of gravity current development fine mesh with no turbulence modelling is preferable, despite high computational demand. In order to confirm that finding, another density difference was chosen and modelled with established optimal parameters. It resulted in propagation speed that was in good agreement with that obtained in physical experiments.

Modelling of gravity current development in three-dimensional setup was considered next. Physical experiments, which resulted in gravity current front positions at the

bottom level of the tank at different time instants, were briefly outlined. Numerical simulations with parameters of fluids and the tank identical to those used in physical experiments were performed. Simulations were run with LES modelling of turbulence and without any turbulence modelling, cell size was set to 5 mm. Obtained front positions were compared to those from physical experiments. Both approaches to turbulence produced front propagation that were similar to front positions recorded during physical experiments. It is therefore concluded that modelling of gravity current in three-dimensional setup can be done accurately with mesh size of 5 mm and LES approach to turbulence, which is more computationally efficient than resolving eddies directly.

6.1.2 Outlook

Further step in the research would be an introduction of bottom roughness, which has an influence on propagation of the gravity current both in two- and three-dimensional situations. In addition, varying width of the gate in the wall separating two reservoirs in three-dimensional case is a factor which impact needs further research, as it is of importance in industry, particularly in coastal engineering. This study offers basis for computationally efficient numerical modelling in the outlined direction. However, additional validation needs to be performed for cases with other density differences.

6.2 Water-structure interaction of submerged floating tube

6.2.1 Conclusions

In this study, literature review on modelling of SFT in homogeneous and stratified water is outlined. Based on physical experiments performed earlier, numerical models were set up and validated, namely, model of horizontal rigid cylinder in homogeneous water at a certain level of submergence. In-line forces acting upon cylinder were the main focus of the study: impacts of submergence and combination of two cylinders were researched. In order to obtain the most computationally efficient model, grid convergence study was performed, as well as various values of CFL criterion. In addition, three-dimensional problem was converted into two-dimensional so as to reduce numerical domain, which is another measure of improving computational efficiency while preserving high accuracy.

As a result of grid convergence study, it was established that very fine mesh with cell size of 2.5 mm yields the most accurate value of in-line force, both by means of

installed REEF3D function and by means of numerical integration of pressures around the cylinder. Initially the latter was employed as method for additional check on the results obtained via function within REEF3D, however, later it was proven to be a good estimate of the in-line force in conditions when REEF3D cannot compute the force accurately, namely when the grid is too coarse. Testing various CFL conditions has demonstrated that time step should be limited to 0.3 for given conditions, which does not allow for significant improvement of computational efficiency. Nevertheless, converting three-dimensional problem into two-dimensional significantly downsized computational demand without imposing undesirable influence on accuracy of the simulation in homogeneous water. That was not the case, however, for the simulation with stratified flow.

Combination of two cylinders in homogeneous water and influence of the distance between them was investigated in two-dimensional model with very fine grid. It was established that none of three different sizes of distance considerably affects in-line force acting upon the first cylinder. Nevertheless, difference up to 6% was registered. In addition, presence of another cylinder behind the first one affected vortex formation, which eliminated in-line force fluctuation. This can be regarded as a favourable effect that combination introduces to the system. No fluctuation in drag force was observed for the second cylinder as well. Moreover, as anticipated, protection effect of the first cylinder resulted in considerably reduced in-line forces registered for the second cylinder. Increasing size of the distance between cylinders led to increasing value of the force, however, the relation is not linear. In addition, for both cases with single cylinder and combination of two cylinders, numerical model set up in REEF3D was capable of accounting for proximity and blockage effects, thus, no increase in drag force due to the effects was observed.

Water-structure interaction of the cylinder in stratified flow was performed in three-dimensional setup with cell size of 5 mm. Similar mesh employed for the case in homogeneous water did not yield accurate in-line force via dedicated function, therefore, numerical integration of pressures around the cylinder was used. It produced in-line force that was smaller than that in the case with homogeneous flow, which is explained by inaccuracy inherent to the cell size in question. In addition, insufficient simulation period might have contributed to that. Nevertheless, observed internal wave height for the densimetric Froude number, which characterized the simulation, was in good agreement with what had been established in physical experiments.

6.2.2 Outlook

Research on water-structure interaction of SFT in flow is an important step, which brings construction of such a unique object closer to realization. However, further investigation needs to be done on, first of all, transverse forces acting upon the cylinder, which were not within the scope of the study. Apart from that, different shapes of the tube should be tested so as to establish the most efficient one. Cylinder under consideration is a blunt object, which is characterized by dominance of drag over skin friction. This is not the case for streamlined objects. In addition, other combinations of cylinders need to be tested, as there are many various configurations of submerged tubes, for example, cylinders placed under each other. All of it is somewhat challenging research, however, it is very promising, albeit balance between computational demand and accuracy imposes certain limits on it. Sufficient simulation period, very fine mesh and three-dimensional setup are main components of the balance that goes through any model solved by means of numerical simulations. This balance needs further investigation so as to increase capability of computational modelling in field of SFT water-structure interaction.

Bibliography

[1] S. Vegvesen. (2018). The e39 coastal highway route, [Online]. Available: https://www.vegvesen.no/en/roads/Roads+and+bridges/Road+projects/e39coastalhighwayroute.

[2] A. Kamath, M. Alagan Chella, H. Bihs, and Ø. A. Arntsen, "Energy transfer due to shoaling and decomposition of breaking and non-breaking waves over a submerged bar", *Engineering Applications of Computational Fluid Mechanics*, vol. 11, no. 1, pp. 450–466, 2017.

[3] E. L. Grotle, H. Bihs, and V. Æsøy, "Experimental and numerical investigation of sloshing under roll excitation at shallow liquid depths", *Ocean Engineering*, vol. 138, pp. 73–85, 2017.

[4] N. Ahmad, H. Bihs, A. Kamath, and Ø. A. Arntsen, "Three-dimensional cfd modeling of wave scour around side-by-side and triangular arrangement of piles with reef3d", *Procedia Engineering*, vol. 116, pp. 683–690, 2015.

[5] N. Ahmad, H. Bihs, D. Myrhaug, A. Kamath, and Ø. A. Arntsen, "Numerical modeling of breaking wave induced seawall scour", *Coastal Engineering*, vol. 150, pp. 108–120, 2019.

[6] N. Ahmad, H. Bihs, D. Myrhaug, A. Kamath, and Ø. A. Arntsen, "Numerical modelling of pipeline scour under the combined action of waves and current with free-surface capturing", *Coastal Engineering*, vol. 148, pp. 19–35, 2019.

[7] H. Bihs, A. Kamath, M. A. Chella, and Ø. A. Arntsen, "Extreme wave generation, breaking, and impact simulations using wave packets in reef3d", *Journal of Offshore Mechanics and Arctic Engineering*, vol. 141, no. 4, p. 041 802, 2019.

[8] A. Aggarwal, H. Bihs, D. Myrhaug, and M. A. Chella, "Characteristics of breaking irregular wave forces on a monopile", *Applied Ocean Research*, vol. 90, p. 101 846, 2019.

[9] J. H. Ferziger and M. Peric, *Computational methods for fluid dynamics*. Springer Science & Business Media, 2012.

[10] D. C. Wilcox, *Turbulence modeling for CFD*. DCW industries La Canada, CA, 1998.

[11] B. E. Launder and D. B. Spalding, "The numerical computation of turbulent flows", in *Numerical prediction of flow, heat transfer, turbulence and combustion*, Elsevier, 1983, pp. 96–116.

[12] H. Schlichting and K. Gersten, *Boundary-layer theory*. Springer, 2016.

[13] J. Smagorinsky, "General circulation experiments with the primitive equations: I. the basic experiment", *Monthly weather review*, vol. 91, no. 3, pp. 99–164, 1963.

[14] G.-S. Jiang and D. Peng, "Weighted eno schemes for hamilton–jacobi equations", *SIAM Journal on Scientific computing*, vol. 21, no. 6, pp. 2126–2143, 2000.

[15] A. Harten, "High resolution schemes for hyperbolic conservation laws", *Journal of computational physics*, vol. 49, no. 3, pp. 357–393, 1983.

[16] C.-W. Shu and S. Osher, "Efficient implementation of essentially non-oscillatory shock-capturing schemes", *Journal of computational physics*, vol. 77, no. 2, pp. 439–471, 1988.

[17] S. Osher and J. A. Sethian, "Fronts propagating with curvature-dependent speed: Algorithms based on hamilton-jacobi formulations", *Journal of computational physics*, vol. 79, no. 1, pp. 12–49, 1988.

[18] A. J. Chorin, "Numerical solution of the navier-stokes equations", *Mathematics of computation*, vol. 22, no. 104, pp. 745–762, 1968.

[19] M. La Rocca, C. Adduce, G. Sciortino, and A. B. Pinzon, "Experimental and numerical simulation of three-dimensional gravity currents on smooth and rough bottom", *Physics of Fluids*, vol. 20, no. 10, p. 106 603, 2008.

[20] J. W. Rottman and J. E. Simpson, "Gravity currents produced by instantaneous releases of a heavy fluid in a rectangular channel", *Journal of Fluid Mechanics*, vol. 135, pp. 95–110, 1983.

[21] A. J. Hogg, M. A. Hallworth, and H. E. Huppert, "On gravity currents driven by constant fluxes of saline and particle-laden fluid in the presence of a uniform flow", *Journal of Fluid Mechanics*, vol. 539, pp. 349–385, 2005.

[22] M. Ungarish and T. Zemach, "On the slumping of high reynolds number gravity currents in two-dimensional and axisymmetric configurations", *European Journal of Mechanics-B/Fluids*, vol. 24, no. 1, pp. 71–90, 2005.

[23] V. W. Ekman, "On dead water", *The Norwegian North Pole Expedition, 1893-1896*, vol. 5, no. 15, pp. 1–151, 1904.

[24] C. J. Nappo, *An introduction to atmospheric gravity waves*. Academic press, 2013.

[25] Ø. A. Arntsen, "Lee waves and hydrodynamical loads due to the motion of a submerged horizontal circular cylinder in a three-layer fluid", *Journal of Hydraulic Research*, vol. 35, no. 4, pp. 435–454, 1997.

[26] H. Lamb, *Hydrodynamics*, 6th ed. University Press, Cambridge, 1932.

[27] Ø. A. Arntsen, "Disturbances, lift and drag forces due to the translation of a horizontal circular cylinder in stratified water", *Experiments in fluids*, vol. 21, no. 5, pp. 387–400, 1996.

[28] T. Sarpkaya, M. Isaacson, and J. Wehausen, "Mechanics of wave forces on offshore structures", *Journal of Applied Mechanics*, vol. 49, p. 466, 1982.

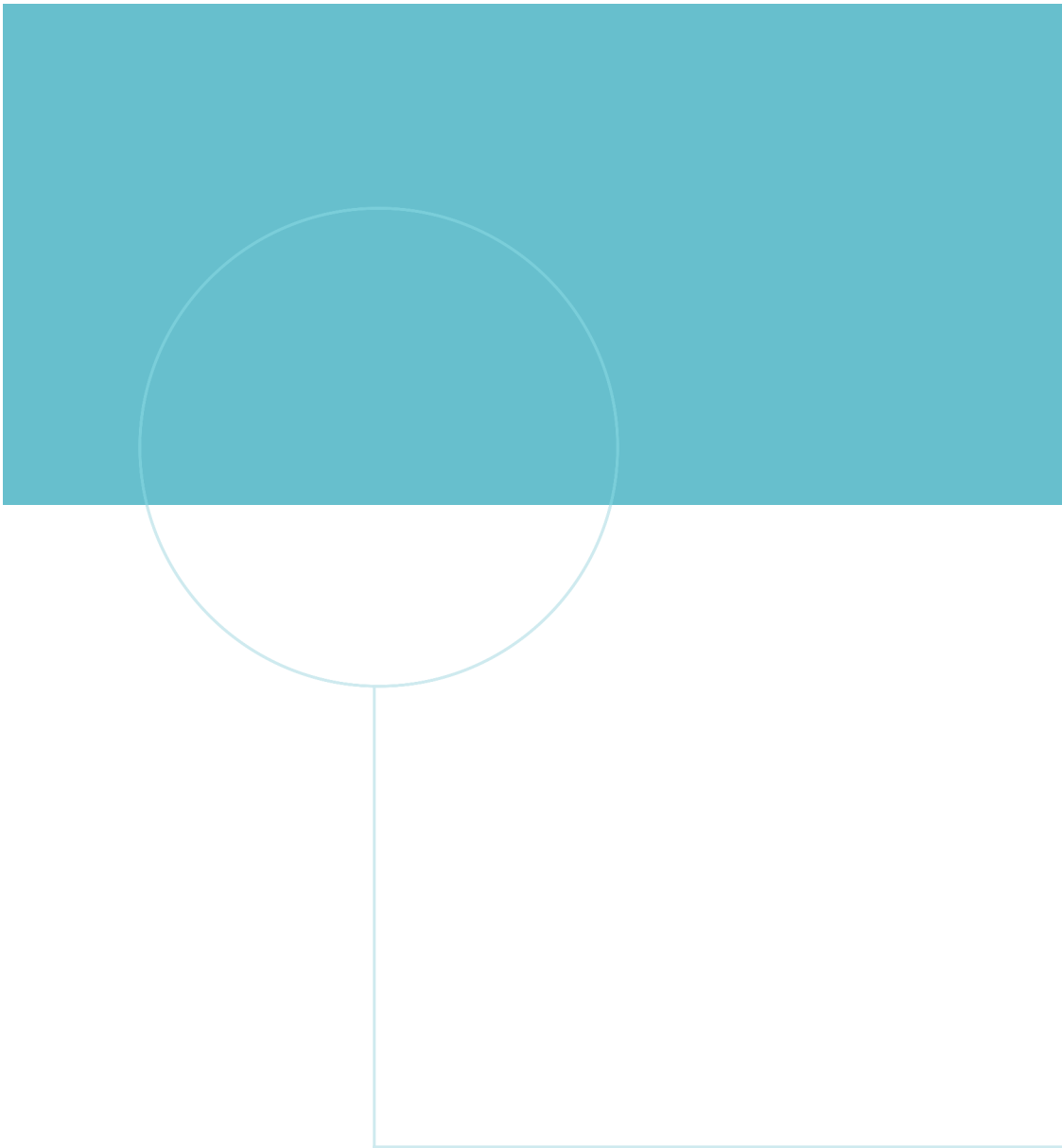

NTNU
Norwegian University of
Science and Technology